

Chemical Communication

Electronic Supplementary Information

Tuning of the Cross-GLaser Products mediated by Substrate-Catalyst's Polymeric Backbone Interactions

Sharanjeet Kaur,[†] Aritra Mukhopadhyaya,^{†,‡} Abdul Selim,^{†,‡} Vijayendran Gowri,[†] K. M. Neethu,[†]
Arif Hassan Dar,[†] Shaifali Sartaliya,[†] Md. Ehesan Ali,^{†,*} and Govindasamy Jayamurugan^{†,*}

[†]Institute of Nano Science and Technology, Mohali-160062, Punjab, India.

[‡]These authors contributed equally

Table of Contents

Section	Page
Section A: General Information	S4
A1. Instrumentation	S4
Section B: Synthetic procedures for catalysts 1, 2, and 3	S5-S10
<i>B1. Synthesis of TC-S-Cu^{III}O (catalyst 1)</i>	S7
<i>B2. Synthesis of EC-S-Cu^{III}O (catalyst 2)</i>	S9
<i>B3. Synthesis of C-S-Cu^{III}O (catalyst 3)</i>	S10
Section C: Characterisation	S11-S25
<i>C1. Characterisation of TC, TC-SH and TC-S-Cu^{III}O 1</i>	S11
<i>C2. Characterisation of EC, EC-SH and EC-S-Cu^{III}O 2</i>	S17
<i>C3. Characterisation of C-SH and C-S-Cu^{III}O 3</i>	S22
Section D: TC-S-Cu^{III}O 1 catalysed aerobic oxidation of homo-coupling of terminal alkynes	S26-S41
<i>D1. Optimisation</i>	S26
<i>D2. General procedure</i>	S26
<i>D3. Spectral details of homo-products</i>	S27
<i>D4. ¹H- and ¹³C-NMR, and GC-MS spectral profiles of homo-products</i>	S29
<i>D5. Oxidative homo-coupling of ethynylbenzene and catalytic amount variability study</i>	S39
<i>D6. Comparison of catalytic activity of present catalyst TC-S-Cu^{III}O 1 with other reported catalysts in literature for the homo-coupling of ethynylbenzene</i>	S40
Section E: TC-S-Cu^{III}O 1 catalysed aerobic oxidative cross-coupling of terminal alkynes	S42-S60
<i>E1. General procedure</i>	S42
<i>E2. Spectral details of cross-Glaser-products</i>	S42
<i>E3. ¹H- and ¹³C-NMR, and GC-MS spectral profiles of cross-Glaser-products</i>	S45
Section F: Computational method and modeling	S61-S67
<i>F1. Polarity order of plausible intermediates</i>	S61
<i>F2. Computational details</i>	S62
<i>F3. Modelling of the catalyst Cu(II)O nanoparticle assembly</i>	S62
<i>F4. Ab initio molecular dynamics</i>	S63
<i>F5. Description of change in electronic structure from Density of States</i>	S66

Section G: Magnetically recyclable catalyst 4	S68
<i>G1. Recyclability study using MNP-TC-S-Cu^{III}O 4</i>	S68
<i>G2. Synthesis of MNP-TC-S-Cu^{III}O 4</i>	S69
<i>G3. Characterisation of MNP-TC-S-Cu^{III}O 4</i>	S70
<i>G4. TEM studies of reused MNP-TC-S-Cu^{III}O 4</i>	S73
H. References	S74-76

Section A. General Information

Unless otherwise noted, all chemicals were obtained from commercial sources (Sigma-Aldrich, Alfa Aesar, Loba Chemie, TCI and Himedia) and used without further purification. The dialysis membrane with molecular weight cut-off (MWCO) of 10 kDa was purchased from Himedia. Column chromatography was carried out on silica gel (60–120 mesh) by elution with appropriate solvents.

A1. Instrumentation

Fourier transform infrared (FT-IR) spectra were recorded on Agilent Cary 660 spectrometer using the KBr pellet technique in a range of 4000–400 cm^{-1} to monitor the chemical synthesis at each step.

Thermogravimetric analysis (TGA) was performed to determine the degradation/decomposition behaviour of samples using thermogravimetric (TG) analyzer-Perkin Elmer STA 8000) at a N_2 flow rate of 10 mL/min and a heating rate of 10 $^\circ\text{C}/\text{min}$.

^1H and ^{13}C nuclear magnetic resonance (NMR) spectra were measured on a Bruker Advance-II spectrometer at 400 MHz and 100 MHz, respectively, in CDCl_3 , D_2O , or $\text{DMSO-}d_6$. The chemical shift was reported in parts per million (ppm) relative to tetramethylsilane (TMS) as the internal standard. All NMR was done with fluorine coupling. Data for ^1H NMR are reported as follows: s = singlet, d = doublet, m = multiplet, br. = broad

X-ray Diffraction (XRD) was performed using a Bruker D-8 advanced diffractometer in the 2θ range of 10–90 $^\circ\text{C}$. The average crystallite size of nanoparticles (NP) was estimated using the Scherrer equation.

X-ray photoelectron spectroscopy (XPS) experiments were performed on a PHI 5000 VersaProbe high-performance electron spectrometer, using monochromatic Al Ka radiation (1486.6 eV) operating at an accelerating X-Ray power of 50W15KV. Before the measurement, the sample was outgassed at 25 $^\circ\text{C}$ in a UHV chamber ($<5 \times 10^{-7}$ Pa). The sample charging effects were compensated by calibrating all binding energies (BE) with the adventitious C 1s peak at 284.6 eV. This reference gave BE values with an accuracy at ± 0.1 eV. Figs. S8a,b shows the X-ray photoelectron spectroscopy (XPS) survey of the as-prepared TC-S-Cu^{II}O **1** indicating the presence of copper photoelectron peaks (Cu3s, Cu2p, Cu3p and its Cu LMM Auger), the oxygen peaks (O1s and its OKLL Auger) and the photoelectron peak of the adventitious carbon (C1s).¹

The *elemental composition* and morphology of the samples were investigated using a SEM-EDX scanning microscope (JEOL, JSM-IT300) attached with Bruker signal processing unit. Samples were prepared by a drop of sample on silicon wafers and vacuum dried.

Inductively coupled plasma-mass spectrometer (ICP-MS) was used to estimate the amount of copper in the catalysts for calculating mol% and turn over frequency (TOF), Agilent Technologies 7700 series. The catalyst was predigested for 1 h in conc. HNO₃. Then, the samples were digested in the microwave for 2 h at 180 °C. The resulting solution was diluted 15 times and analysed using ICP-MS.

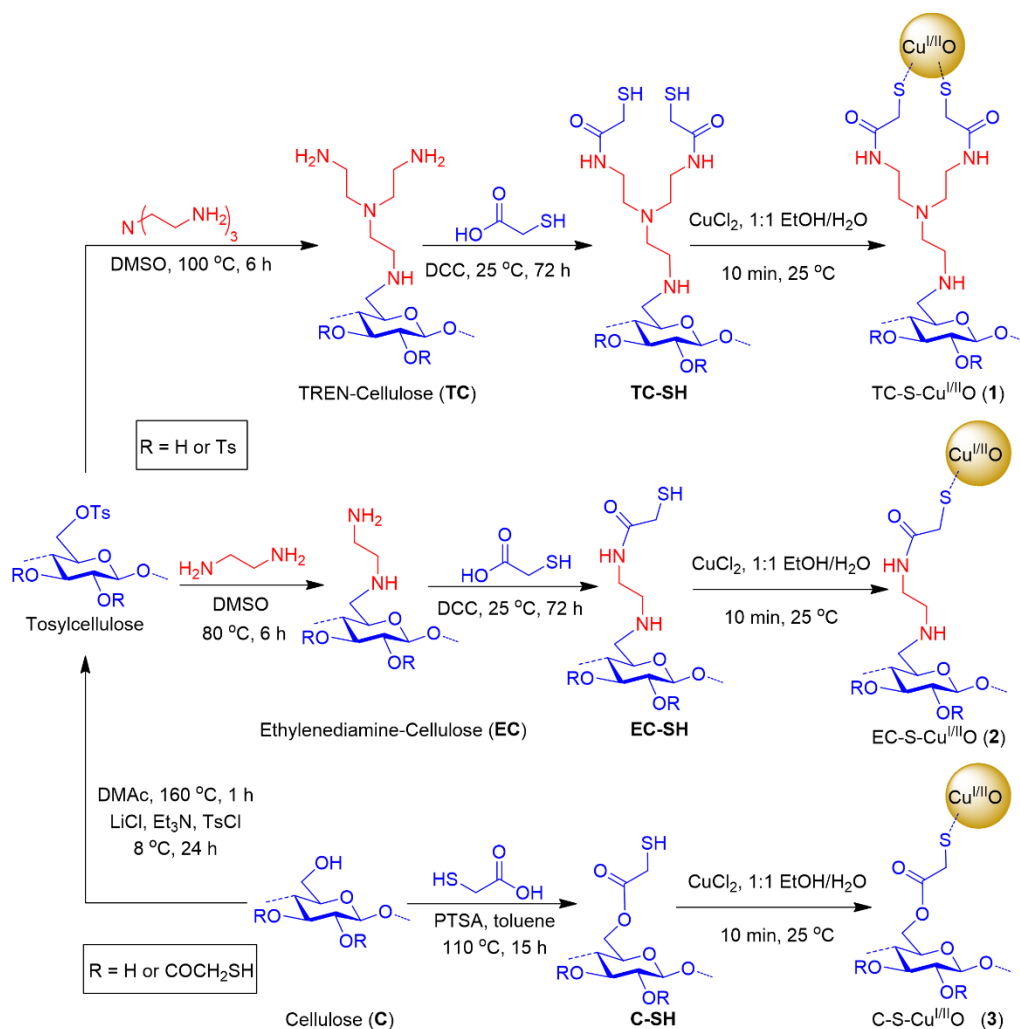
Transmission Electron microscopy (TEM) images were acquired on a Jeol 2100 HR operating at 120 kV. Samples were prepared by depositing a drop of diluted nanoparticle solution on 300 mesh TEM grid and dried under vacuum for 2 h.

Gas chromatography-mass spectrometry (GC-MS) analysis was performed using a Shimadzu GC coupled with a GCMS-QP 2010 plus mass detector (GC-MS) and a single-quadrupole mass spectrometer Quantum (Shimadzu) with 100% dimethyl polysiloxane (Restek Rxi-1ms; 30 m × 0.25 mmID., 0.25 µm film thickness) column. GC-MS operating conditions: The initial oven temperature was 60 °C, maintained for 1 min and then ramped to 270 °C at a rate of 10 °C/min followed by holding for 5 min at 270 °C. The initial temperature of the injector was 63 °C and then programmed at the same rate as oven. Helium was used as a carrier gas with primary pressure of 570 KPa. The split injection mode was used with a split ratio of 10.0. The injection volume of each sample was 1 µL. Mass spectrometer settings: electron impact ionization mode with electron energy of 70 eV, ion source and interface temperatures were set at 200 and 270 °C, respectively and scan mass range *m/z* 50–800. Dodecane is used as an internal standard.

Section B. Synthetic procedures for catalysts 1, 2, and 3

All catalysts (**1**, **2**, and **3**) were synthesised starting from cellulose (Scheme S1). For catalysts **1** and **2** functionalization at the C-6 position of cellulose with tris-(2-aminoethyl)amine (TREN) (TC)^{2,3} and ethylenediamine (EC),⁴ respectively were achieved via tosylcellulose. The synthesis of tosylcellulose was performed following the reported procedure.^{2–5} Synthesis of various amine functionalization at the C-6 position of cellulose have been extensively studied as they exhibit high biocompatibility for biological applications.^{6,7} Upon synthesis of TREN- and ethylenediamine-

functionalised celluloses (TC and EC)²⁻⁵ and unfunctionalised-cellulose (C)^{8,9} were converted to catalysts TC-S-Cu^{I/II}O **1**, EC-S-Cu^{I/II}O **2**,¹⁰ and C-S-Cu^{I/II}O **3**,^{8,9} respectively in two steps synthetic procedures. The first step involves the generation of SH-functionalization to afford TC-SH,¹⁰ EC-SH,¹⁰ and C-SH^{8,9} (Schemes S2B, S3, and S4, respectively). Whereas the second step involves the generation copper oxide nanoparticles on to TC-SH, EC-SH, and C-SH to provide the final catalysts **1**, **2**, and **3**,^{8,9} respectively (Schemes S2B, S3, and S4). It is expected that the thiol group should act as both reducing agent as well as the supporting agent for the formation of nanoparticles. Generation of copper(I) oxide nanoparticles using SH-functionalised cellulose paper have been successfully demonstrated by Felpin and co-workers.⁸ The stepwise synthetic procedures are detailed below.

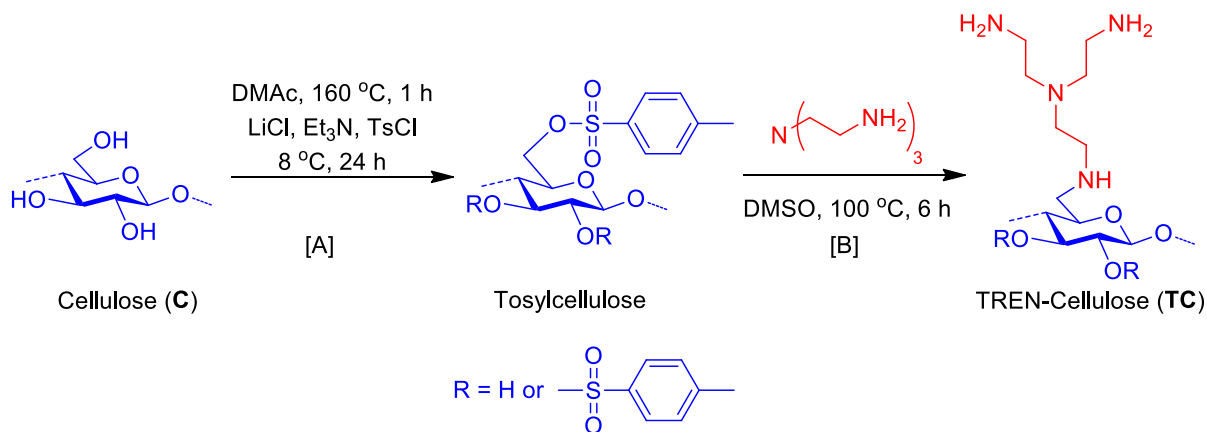


Scheme S1. Synthesis of catalysts **1**, **2**, and **3** starting from cellulose.

B1. Synthesis of TC-S-Cu^{III}O (catalyst 1)

Synthesis of catalyst **1** involves two stages. The first stage involves the synthesis of TREN-cellulose (TC) (Scheme S2A) via 6(2)-O-tosylcellulose (tosylcellulose)^{2,3} starting from cellulose in two steps (steps 1 and 2). Similarly, the second stage involves the conversion of TC into catalyst **1** via thiol-functionalised TREN-Cellulose (TC-SH) (Scheme S2B) in another two steps (Steps 3 and 4).

TC was synthesised according to the literature procedures.^{2,3} It involved two steps: step A), synthesis of tosylcellulose from cellulose, step B). Conversion of tosylcellulose into TC. Tosylcellulose^{2,3} was synthesised by reacting microcrystalline cellulose with tosyl chloride (TsCl) and triethylamine (Et₃N) in dimethylacetamide (DMAc) and LiCl under homogeneous conditions.²⁻⁵ Then TC was obtained by reacting tosylcellulose with tris-(2-aminoethyl)amine (TREN) as shown in Scheme S2A.



Scheme S2A. Synthesis of [1] tosylcellulose, and [2] TREN-cellulose (TC).

Step A. Synthesis of 6(2)-O-tosylcellulose (Tosylcellulose)

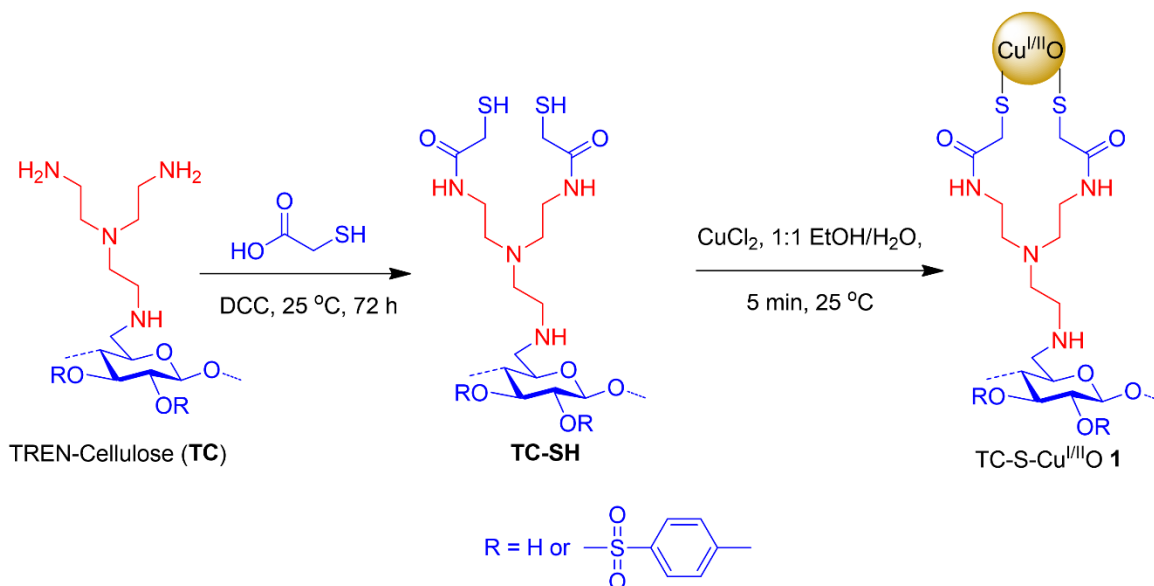
Tosylcellulose was synthesised by reacting cellulose with TsCl under homogeneous conditions according to Rahn *et al.*³ Microcrystalline cellulose (2 g, 12.46 mmol) was dissolved in dimethylacetamide (DMAc, 47 mL) and heated with stirring at 160 °C for 1 h under N₂ atmosphere. After 1 h, the contents of the flask were allowed to cool to 100 °C and anhydrous LiCl (4 g, 94.36 mmol) was added. The reaction mixture was further cooled to 25 °C with continuous stirring and the cellulose dissolved completely within 6 h. To a stirred cellulose solution, a mixture of Et₃N (6.06 mL, 60 mmol) and DMAc (4.2 mL) was added. A solution of TsCl (4.04 g, 21.19

mmol) in DMAc (6 mL) was added dropwise within 5 min to the reaction flask while maintaining the temperature at 8 °C and stirring was continued further 24 h. Then the reaction mixture was slowly poured into ice-water (~1.5 L) to form a white precipitate. The precipitate was filtered off, washed carefully with distilled water (500 mL) and EtOH (200 mL). Then, acetone (100 mL) was used to dissolve the precipitate using sonication. Re-precipitation was carried out by adding distilled water (300 mL). After filtration, the white precipitate was washed with EtOH (50 mL × 2) and vacuum dried at 50 °C for 24 h.

Step B. Synthesis of 6-deoxy-6-(*ω*-aminoethyl)aminocellulose (TC)^{2,3}

To a vigorously stirred solution of tosylcellulose (4.2 g) in DMSO (40 mL) at 100 °C, tris-(2-aminoethyl)amine (TREN) (22 mL, 0.407 mol) was added under N₂ atmosphere. After 6 h, the reaction mixture was poured into acetone (600 mL) to afford a precipitate. The obtained precipitate was washed three times with iPrOH (50 mL), and vacuum dried at 50 °C for 24 h to afford TC (3.8 g) as a yellowish-brown sticky solid.

In the second stage, steps 3 and 4 were performed to obtain catalyst **1** via TC-SH (Scheme S2B). TC-SH was synthesised by treating thioglycolic acid which is mediated by *N,N'*-dicyclohexylcarbodiimide [DCC, as coupling agent] as described by below procedure.



Scheme S2B. Synthesis of thiol-functionalised TREN-cellulose (TC-SH) and TC-S-Cu^{II}O **1**.

Step 3. Synthesis of thiol-functionalised TREN-cellulose (TC-SH)¹⁰

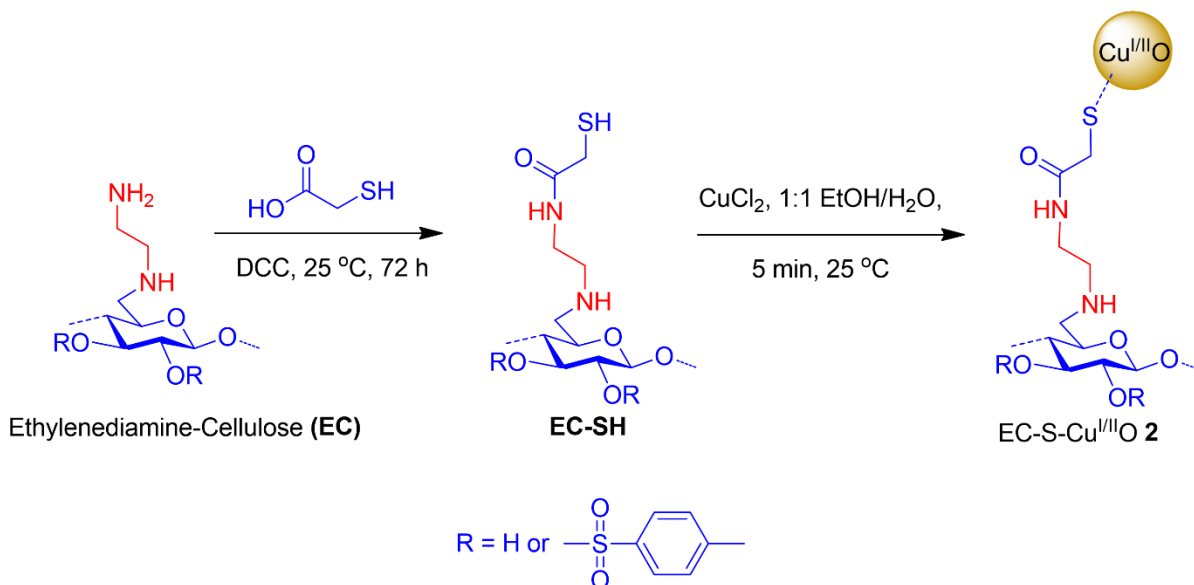
TREN-cellulose TC (0.4 g) was dissolved in 100 mL of 0.2% v/v hydrochloric acid (HCl) aqueous solution. Then 5 mL of HCl aqueous solution (0.2% v/v) containing thioglycolic acid (5.0 mmol) and the same molar ratio of DCC was dropped into the TC solution and stirred for 72 h at 25 °C. The reaction solution was filtered through the sintered funnel, and the filtered solution was dialysed (MWCO: 10,000 Daltons) against distilled water for 5 days and then lyophilised to give light yellow foamy solid TC-SH (0.35 g).

Step 4. Synthesis of catalyst 1

Catalyst 1 was synthesised by adding 1 wt% aqueous solution of TC-SH (1 g, 100 mL) to an ethanolic solution of CuCl₂ (1 g, 100 mL).^{8,9} The resulting 1:1 v/v mixture was stirred at 25 °C for 10 minutes. Then the obtained homogeneous solution was used as it is for catalysis.

B2. Synthesis of EC-S-Cu^{II}O (catalyst 2)

The ethylenediamine-functionalised cellulose (EC)²⁻⁵ was prepared according to the literature procedure. EC-SH was synthesised in two steps from ethylenediamine-cellulose (EC) via thioglycolation and copper oxide nanoparticles formation (Scheme S3).



Scheme S3. Synthesis of EC-S-Cu^{II}O 2.

Step 1. Synthesis of thiol-functionalised EC-SH¹⁰

Ethylenediamine functionalised-cellulose EC (0.4 g) was dissolved in 100 mL of 0.2% v/v hydrochloric acid aqueous solution. Then 5 mL HCl solution (0.2% v/v) containing thioglycolic acid (5.0 mmol) and the same molar ratio of DCC was dropped into the EC solution and stirred for 72 h at 25 °C. The reaction solution was filtered, and the filtered solution was dialysed (MWCO: 10,000 Daltons) against distilled water for 5 days and then lyophilised to give the light yellow coloured EC-SH (0.35 g)

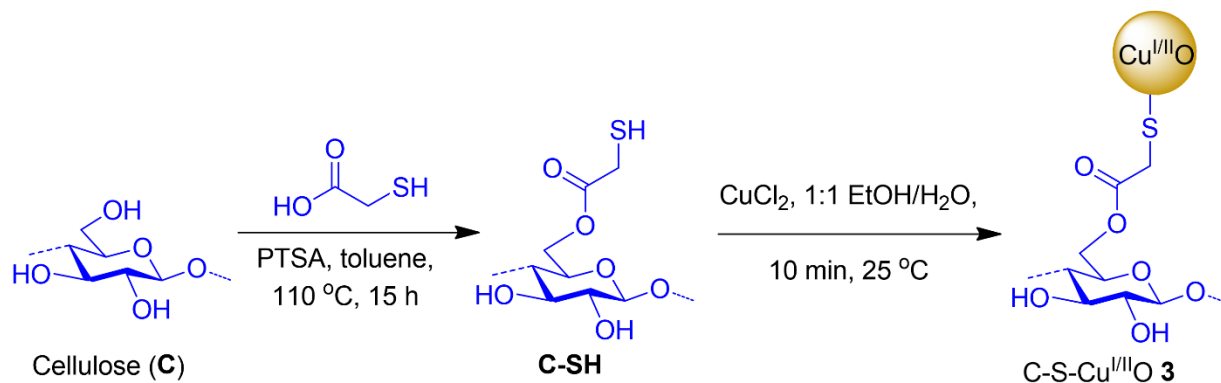
Step 2. Synthesis of EC-S-Cu^{III}O 2

EC-S-Cu^{III}O 2 was synthesised by adding 1 wt% aqueous solution of EC-SH (1 g, 100 mL) to an ethanol solution of CuCl₂ (1 g, 100 mL).^{8,9} The resulting 1:1 v/v mixture was stirred at 25 °C for 10 min. Then the obtained homogeneous solution was used as it is for catalysis.

B3. Synthesis of C-S-Cu^{III}O (catalyst 3)^{8,9}

Similar to catalyst 2, synthesis of catalyst 3 was achieved in two steps starting from cellulose (Scheme S4).

- (i) The thiol-functionalised cellulose C-SH was prepared according to the literature procedure.^{8,9}
- (ii) C-S-Cu^{III}O 3^{8,9} was synthesised by adding 1 wt% aqueous solution of C-SH (1 g, 100 mL) to an ethanol solution of CuCl₂ (1 g, 100 mL). The resulting 1:1 v/v mixture was stirred at 25 °C for 10 min. Then the obtained homogeneous solution was used as it is for catalysis.



Scheme S4. Synthesis of C-S-Cu^{III}O 3.

Section C: Characterisation

C1. Characterisation of TC, TC-SH and TC-S-Cu^{III}O 1

Characterisation of TREN-cellulose (TC) and TC-SH, synthesised in steps 2 and 3, respectively in Schemes S2A and S2B, Section B) were investigated by FT-IR, ¹H-NMR, SEM-EDX, CHNS analyses. Whereas the TC-S-Cu^{III}O 1 was characterised by FT-IR, PXRD, ¹H-NMR, SEM, CHNS, XPS, TEM, TGA, and ICP-MS analyses. The details are discussed below.

FT-IR data of TC, TC-SH and TC-S-Cu^{III}O 1:

FT-IR (TC, KBr): $\tilde{\nu}$ = 3420 (N–H stretching, s), 2923 (C–H symmetrical stretching, m), 1650 (m), 1574 (–NH₂ scissoring, s), 1472 (–CH₂ bending, s), 1362 (C–NH₂, m), 1316 (w), 1175 (w), 1120 (C–O–C, m), 1061 (s), 811 (w), 681 (w), 558 cm^{–1} (–O–H out of plane bend, w).

FT-IR (TC-SH, KBr): $\tilde{\nu}$ = 3399 (N–H stretching, s), 2919 (C–H symmetrical stretching, m), 2631 (–S–H, w), 1713 (C=O of amide, s), 1659 (–NH₂ scissoring, s), 1572 (–CH₂ bending, s), 1376 (C–NH₂, s), 1211 (s), 1176 (s), 1120 (C–O–C, s), 1033(s), 1006 (s), 814 (m), 681(s), 563 cm^{–1} (–O–H out of plane bend, s).

Comparative FT-IR spectral analysis (Fig. S1) of TC and TC–SH showed the formation of TC from tosylcellulose due to the presence of an amino peak at 3421 cm^{–1} (for medium N–H stretching) and 1574 cm^{–1} (for medium N–H bending). Similarly, formation TC-SH was indicated due to the presence of S–H peak at 2631 cm^{–1} and C=O (amide) peak at 1713 cm^{–1}.

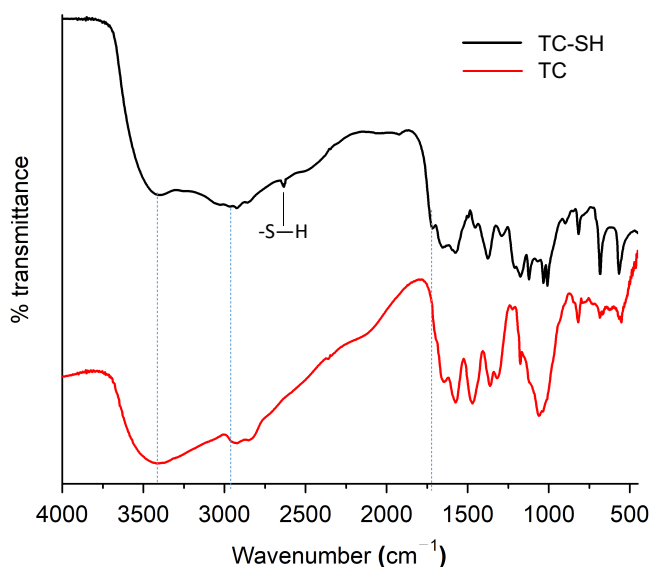


Fig. S1. FT-IR spectra of TREN-cellulose (TC) and its derivative (TC-SH).

IR (TC-S-Cu^{III}O 1, KBr): $\tilde{\nu}$ = 3487 (N–H stretching, s), 1719 (C=O, m), 1647 (N–H bending, s), 1604 (s), 1356 (w), 1200 (s), 1164 (s), 1036 (m), 994 (s), 958 (m), 660 (m), 603, 584 (m), and 521 (S–S). The presence of bands at 660, 603, and 584 cm^{-1} are due to the presence of CuO/Cu₂O in the FT-IR spectrum (Fig. S2) of catalyst **1** indicate different modes of bending/stretching vibration of the Cu–O bond of copper oxide NP.^{11,12}

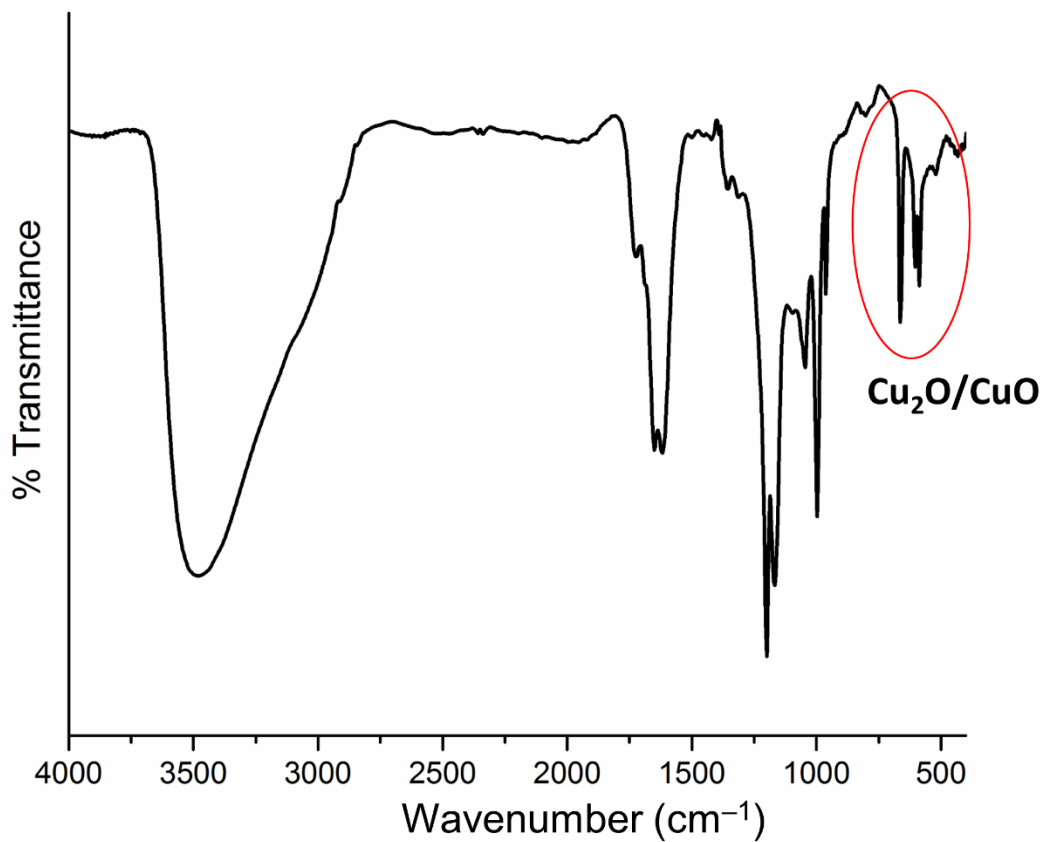


Fig. S2. FT-IR spectrum of as-prepared TC-S-Cu^{III}O **1**.

Powder XRD of TC-S-Cu^{III}O (Catalyst 1). The powder X-ray diffraction (PXRD) pattern (Fig. S3) of as-prepared TC-S-Cu^{III}O **1** represents the formation of CuO/Cu₂O NP, matches that of Joint Committee on Powder Diffraction Standards (JCPDS) no. 48-1548 corresponding to the monoclinic structure of CuO and JCPDS 05-0667 corresponding to cubic face-centered cubic (fcc) structure of Cu₂O, respectively.^{12,13}

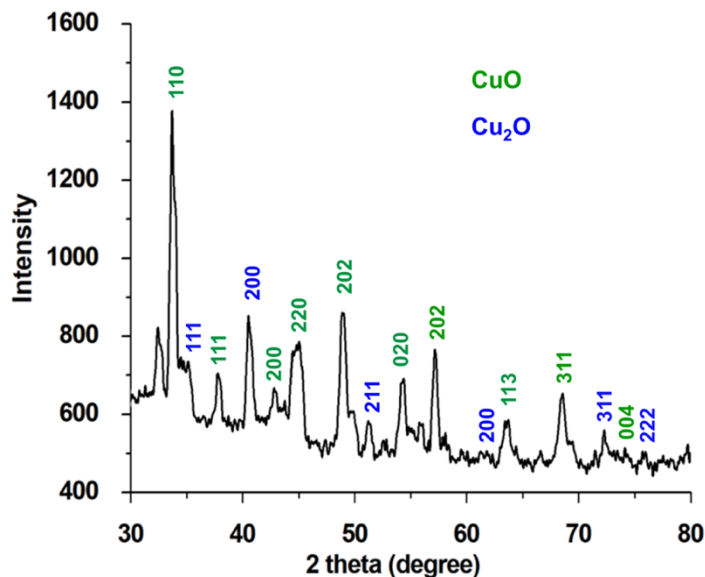


Fig. S3. Powder X-ray diffraction pattern of TC-S-Cu^{II}O 1.

¹H NMR data of TC and TC-SH:

¹H NMR (TC, 400 MHz, D₂O, 298 K): δ = 2.30 (s, -CH₂ TREN), 2.55–2.63 (m, -CH₂ TREN), 2.73–2.84 (m, -CH₂ TREN), 3.32–4.39 (cellulose protons), 8.18 & 7.84 (tosylate protons).

*¹H NMR (TC-SH, 400 MHz, DMSO-*d*₆, 298 K):* δ = 2.06–2.07 [-CH₂, TREN (h and e)], 2.35–2.93 (-CH₂, TREN (f, g, I and j)], 3.29–3.68 (cellulose backbone, a-d).

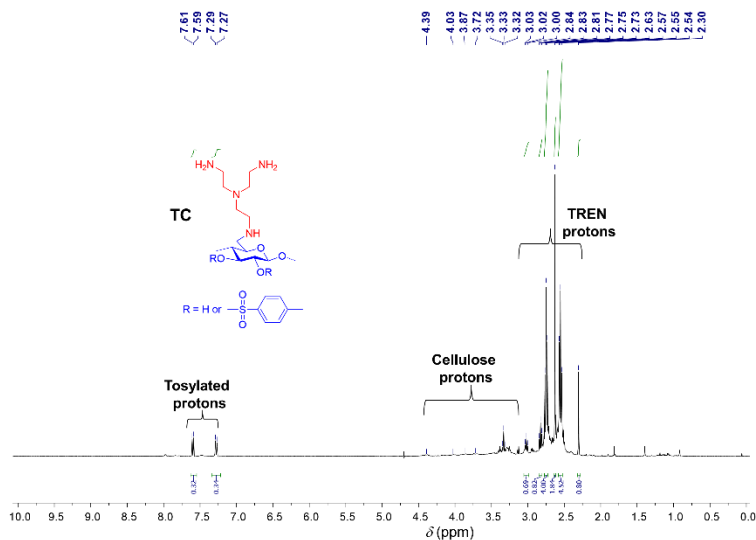


Fig. S4. ¹H NMR (400 MHz, D₂O, 298 K, HOD peak is suppressed) spectrum of TREN-cellulose (TC).

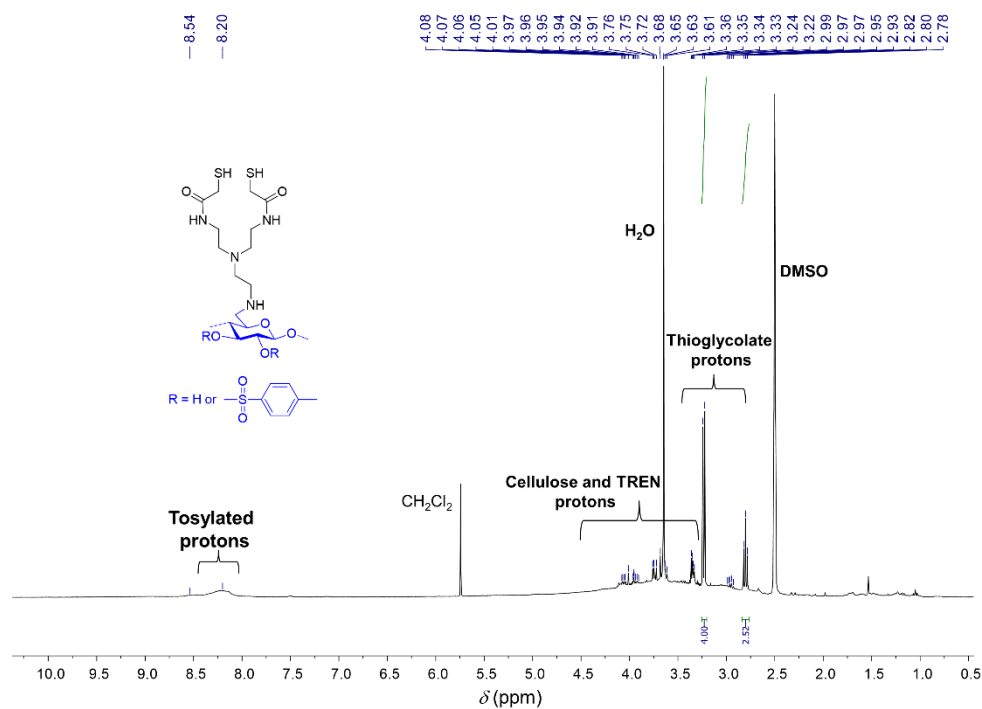


Fig. S5. ^1H NMR (400 MHz, DMSO-d_6 , 298 K) spectrum of TC-SH.

SEM analysis of TC-SH and Catalyst 1:

Energy dispersive X-ray (EDX) spectrum was measured using a Scanning Electron Microscope equipped with EDX facility. The elemental composition and relative abundance are given in Table S1.

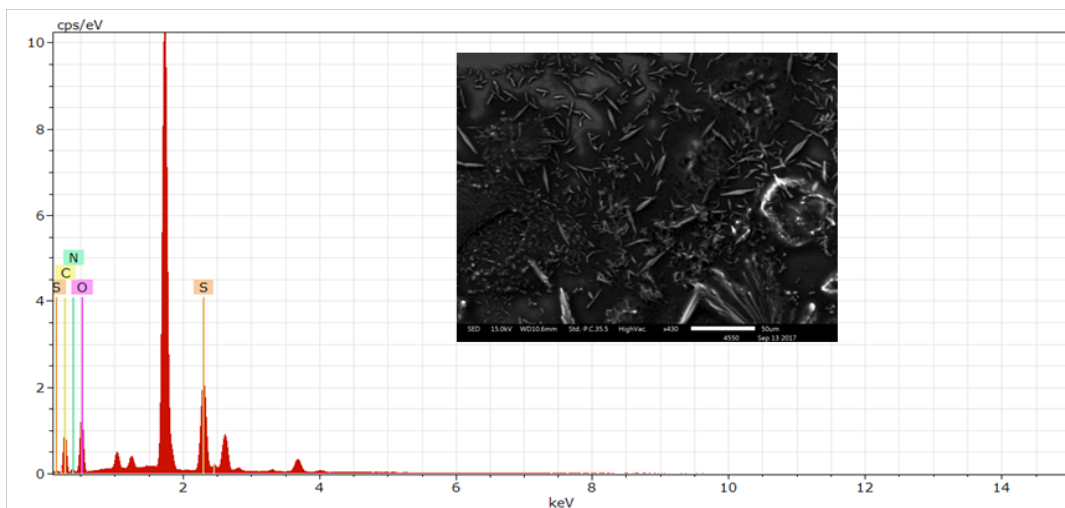


Fig. S6. Energy dispersive X-ray (EDX) spectrum of TC-SH. Scanning electron microscopic image of TC-SH (inset, scale bar 50 μm).

Table S1. SEM-EDX spectrum measurement of TC-SH.

Element	Kvalue	Weight (%)
		TC-SH
Sulphur (S)	0.152 (K ₁)	8.44
	2.314 (K ₂)	
Oxygen (O)	0.525(K _α)	35.90
Carbon (C)	0.277(K _α)	47.66
Nitrogen (N)	0.392(K _α)	8.01

Elemental analysis (TREN-SH) by CHNS analyzer: observed C 48.8%; H 8.2%, N 11.9%, S 12.2%. The degree of thioglycolic acid substitution is 88.8%. The elemental composition obtained from SEM-EDX is quite comparable with the values of CHNS analysis.

SEM image of TC-S-Cu^{II}O 1:

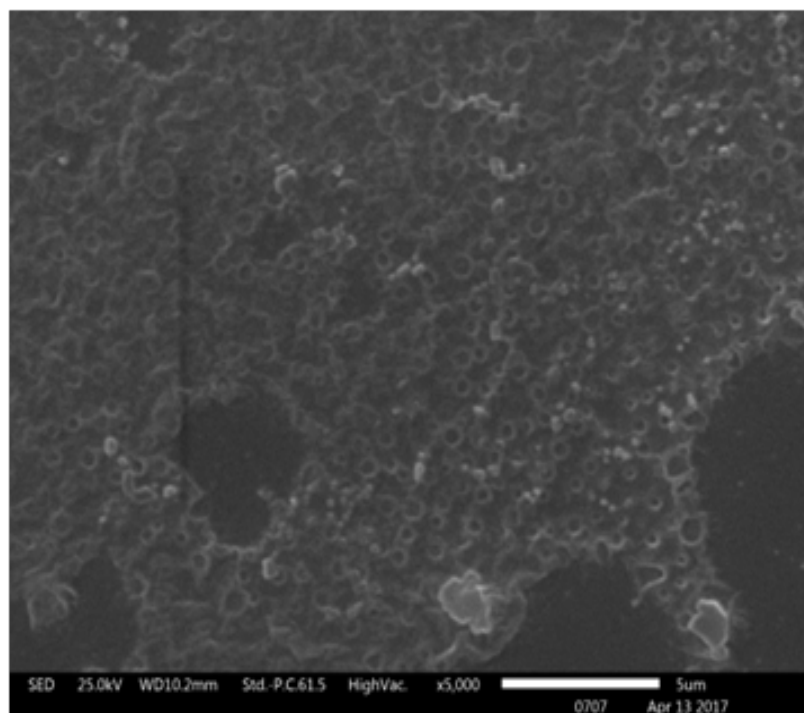


Fig. S7. Scanning electron microscopic image of TC-S-Cu^{II}O 1.

The SEM images of TC-SH and catalyst 1 show clearly the change in the morphology (Figs. S6 and S7).

XPS and TEM of TC-S-Cu^{III}O 1:

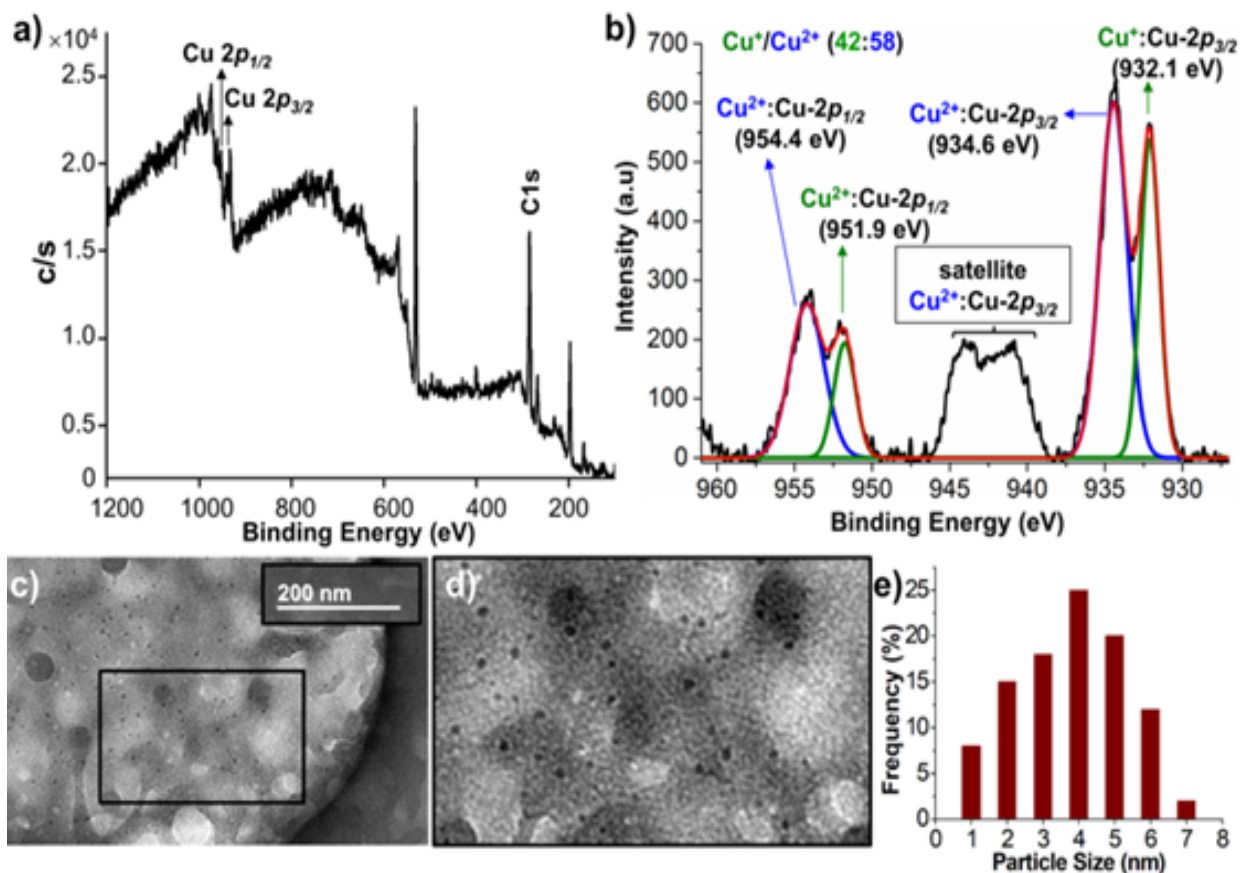


Fig. S8. (a) XPS survey spectrum of TC-S-Cu^{III}O 1. (b) XPS copper profile describing the coordination behaviour of Cu with TREN-Cellulose. (c) TEM images of TC-S-Cu^{III}O 1. (d) Magnified view of the selected area showing the particle size less than 10 nm. (e) Their respective particle size distribution histogram.

TGA analysis of TC-S-Cu^{III}O 1: In TGA, the decomposition occurs in four stages (Fig. S9): (i) the initial stage from 30 to 100 °C, 18% weight loss due to the removal of absorbed ethanol and water from the catalyst 1.¹⁴ (ii) The next 28% weight loss occurs from 100 to 200 °C due to the decomposition of thioglycolic part from the catalyst. (iii) The next 15% degradation from 200 to 350 °C was attributed to the cleavage of TREN from the TC. (iv) Further, degradation from 350 to 500 °C is attributed to the oxidation and pyrolysis of cellulose (14% weight loss).¹⁵

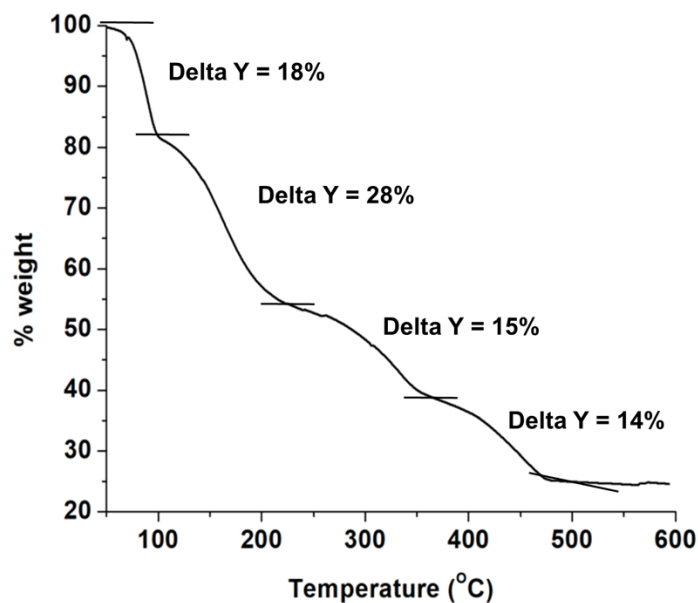


Fig. S9. TGA pattern of TC-S-Cu^{III}O 1.

ICP-MS data of TC-S-Cu^{III}O 1: The loading of copper on catalyst 1 was found to be 36.2 wt%, as determined by ICP-MS.

C2. Characterisation of EC, EC-SH and EC-S-Cu^{III}O 2

Characterisation of synthesised ethylenediamine-functionalised cellulose (EC)²⁻⁵ and EC-SH (Schemes S3, Section B2) was investigated by FT-IR, NMR, and SEM-EDX analyses. Whereas the EC-S-Cu^{III}O 2 (Schemes S3, Section B2) was characterised by FT-IR, PXRD, TEM, and ICP-MS analyses. The details are discussed below.

FT-IR:

FT-IR (EC, KBr): $\tilde{\nu}$ = 3435 (N-H stretching, s), 2928 (w), 2836 (C-H stretching, w), 1645 (m), 1572 (-NH₂ scissoring, s), 1467 (-CH₂ bending, s), 1358 (C-NH₂, m), 1316 (m), 1170 (m), 1065 (C-O-C, s), 814 (m), 677 (w), 549 cm⁻¹ (-O-H out of plane bend, w).

FT-IR (EC-SH, KBr): $\tilde{\nu}$ = 3412 (N-H stretching, s), 2919 (C-H symmetrical stretching, m), 2636 (-S-H, w), 1718 (C=O, m), 1654 (s), 1572 (-NH₂ scissoring, s), 1453 (w), 1371 (C-NH₂, s), 1211 (s), 1175 (s), 1120 (s), 1029 (s), 1006 (s), 898 (w), 814 (m), 682 (s), 568 cm⁻¹ (-O-H out of plane bend, s).

Comparative FT-IR spectral analysis (Fig. S10) of ethylenediamine-cellulose (EC) and EC-SH showed the formation of EC from tosylcellulose due to the presence of an amino peak at 3435 cm^{-1} (for medium N-H stretching) and 1572 cm^{-1} (for medium N-H bending). Similarly, formation EC-SH was indicated due to the presence of S-H peak at 2636 cm^{-1} and C=O (amide) peak at 1718 cm^{-1} .

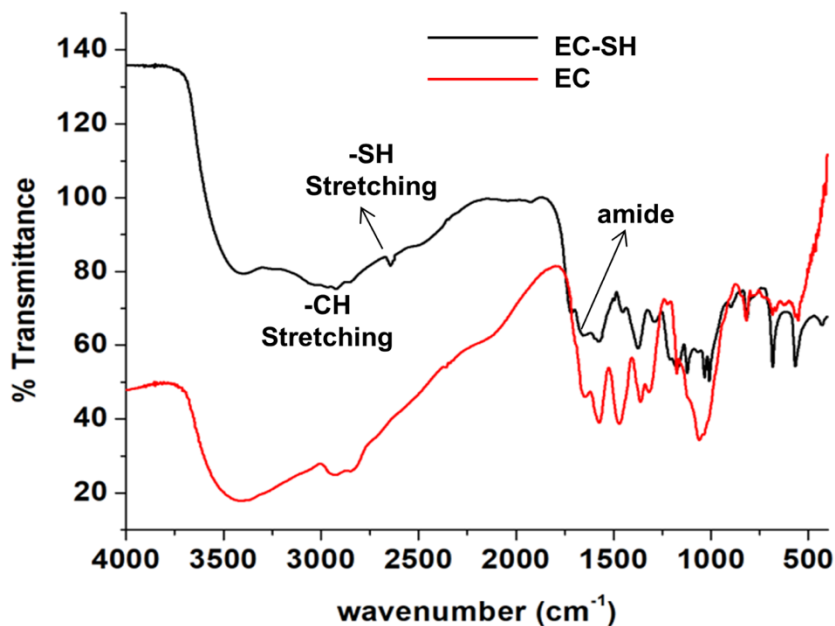


Fig. S10. FT-IR spectra of EC and EC-SH.

FT-IR (EC-S-Cu^{I/II}O 2, KBr): $\tilde{\nu}$ = 3524 (N-H stretching, s), 1648 (s), 1614 (s), 1427 (w), 1392 (w), 1222 (w), 1197 (m), 1173 (w), 1127 (w), 1041 (ring C-O stretching vibration in cellulose, m), 997 (m), 905 (w), 662 (m), 603 (m), 585 (m). The presence of bands at 662, 603, and 584 cm^{-1} are due to the presence of CuO/Cu₂O in the FT-IR spectrum (Fig. S11) of catalyst **2** indicate different modes of bending/stretching vibration of the Cu-O bond of copper oxide NP.^{11,12}

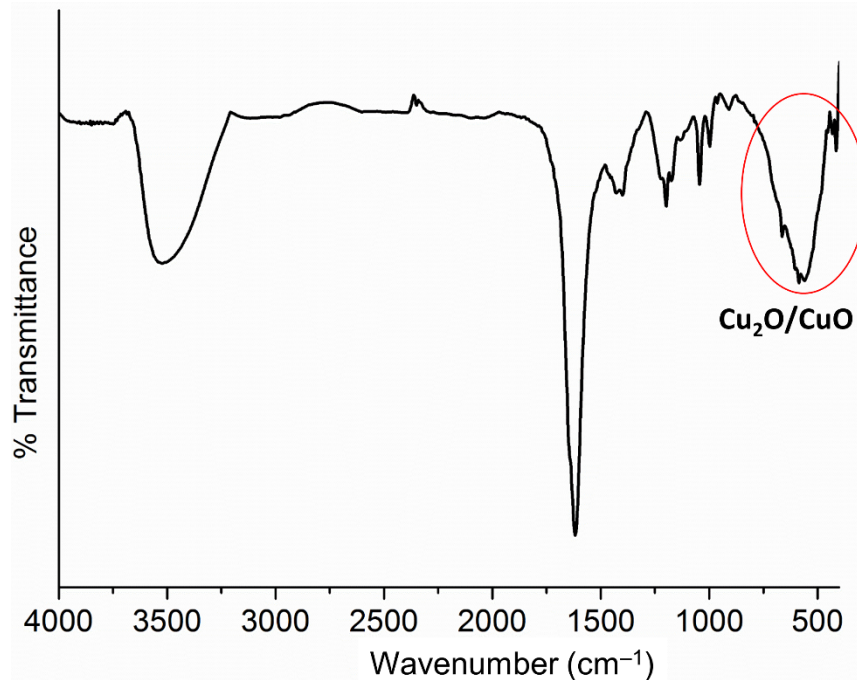


Fig. S11. FT-IR spectrum of EC-S-Cu^{I/II}O 2.

Powder XRD of EC-S-Cu^{I/II}O 2: The PXRD (Fig. S12) pattern of as-prepared EC-S-Cu^{I/II}O 2 represents the formation of CuO/Cu₂O NP, matches that of JCPDS no. 48-1548 corresponding to the monoclinic structure of CuO and JCPDS 05-0667 corresponding to cubic fcc structure of Cu₂O, respectively.^{12,13}

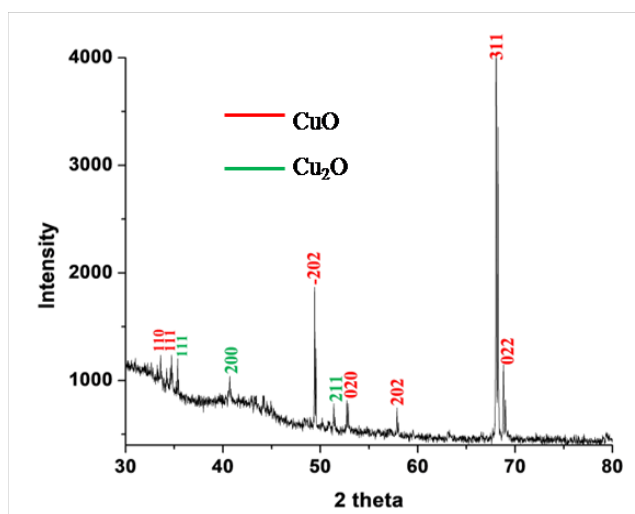


Fig. S12. PXRD spectrum of EC-S-Cu^{I/II}O 2.

NMR Data of EC and EC-SH

^1H NMR (EC^{2-5} , 400 MHz, D_2O , 298 K): $\delta = 2.51 - 2.58$ ($-\text{CH}_2$ EDA), 2.88 (C_6 proton of cellulose), 2.90–4.6 (cellulose backbone); ^{13}C NMR (EC, 100 MHz, D_2O , 298 K): $\delta = 38.71$ ($-\text{CH}_2$ primary amine), 55.69 ($-\text{CH}_2$ secondary amine), 64.23 (C_6 -cellulose), 125 (tosyl), 129.42, 142.27.

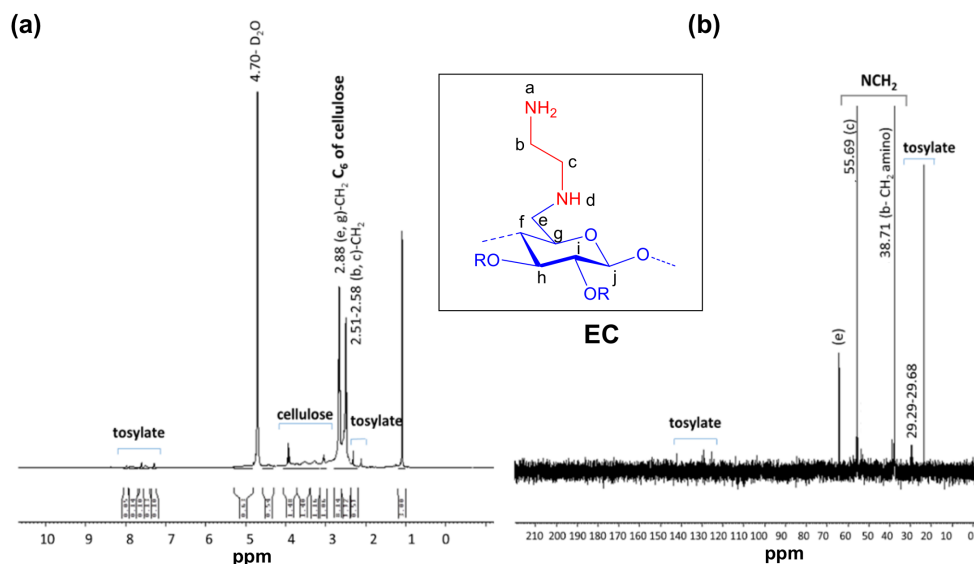


Fig. S13. a) ^1H - and b) ^{13}C -NMR spectra of EC.

^1H NMR (EC-SH, 400 MHz, D_2O , 298 K): $\delta = 3.25 - 3.45$ [$-\text{CH}_2$, EDA (c and d)], 2.60 (C_6 proton of cellulose), 3.51 – 3.65 (cellulose backbone, f-j). ^{13}C NMR (EC-SH, 100 MHz, D_2O , 298 K): $\delta = 36.09, 38.98, 40.19, 41.88, 46.81, 62.94, 65.43, 72.08$.

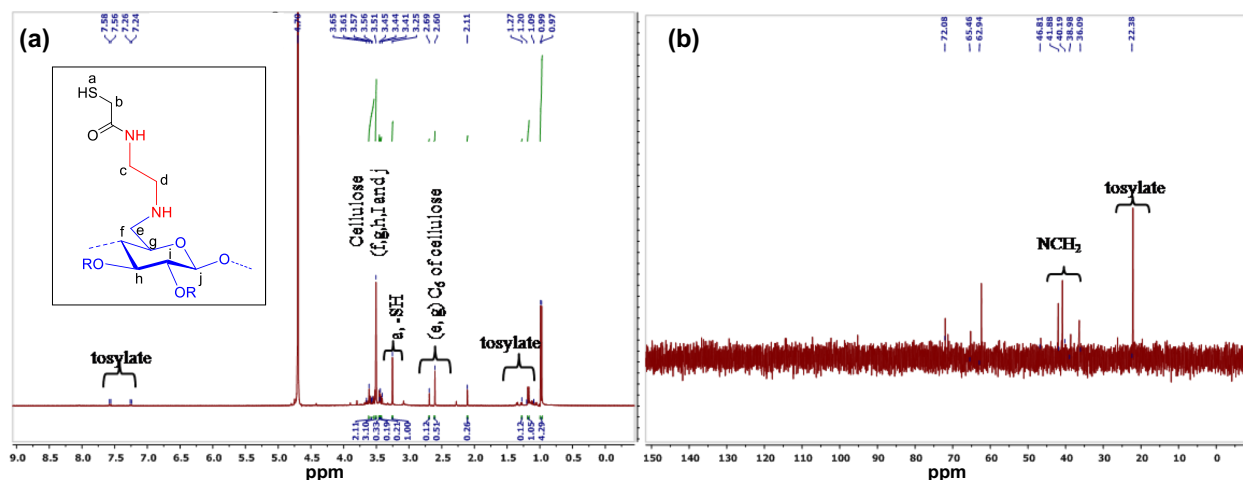


Fig. S14. a) ^1H - and b) ^{13}C -NMR spectra of EC-SH.

SEM-EDX data of EC-SH.

Energy dispersive X-ray (EDX) spectrum of EC-SH was measured using a Scanning Electron Microscope equipped with EDX facility (Fig. S15). The elemental composition and relative abundance are given in Table S2.

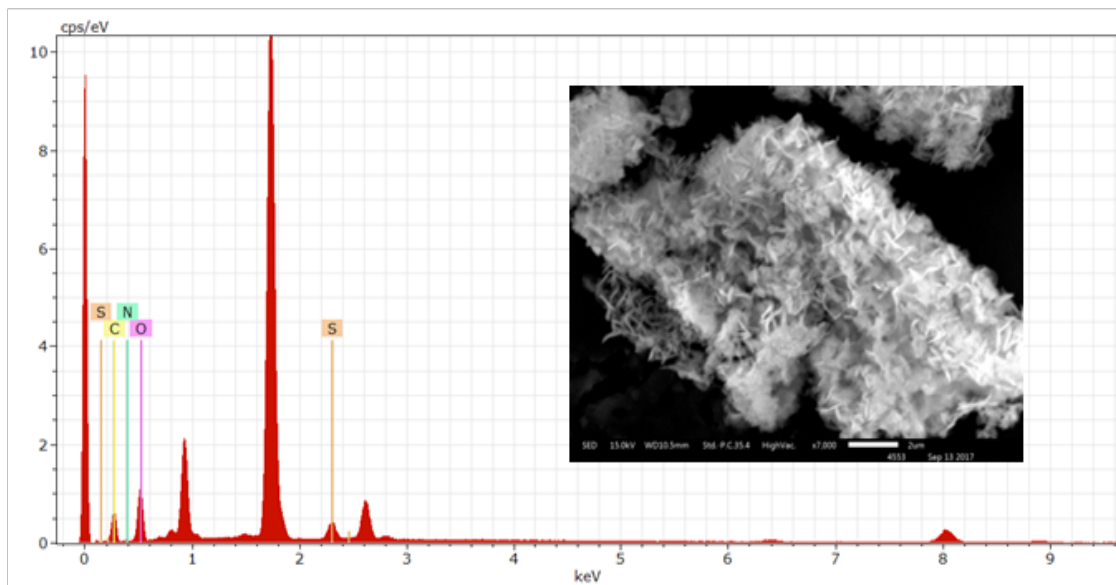


Fig. S15. Energy dispersive X-ray (EDX) spectrum of EC-SH. (inset) Scanning electron microscopic image of EC-SH.

Table S2. SEM-EDX spectra measurement of EC-SH.

Element	Kvalue	Weight (%)
		EC-SH
Sulphur (S)	0.152 (K ₁)	3.03
	2.314 (K ₂)	
Oxygen (O)	0.525(K _α)	51.64
Carbon (C)	0.277(K _α)	42.30
Nitrogen (N)	0.392(K _α)	3.03

TEM study of EC-S-Cu^{III}O 2:

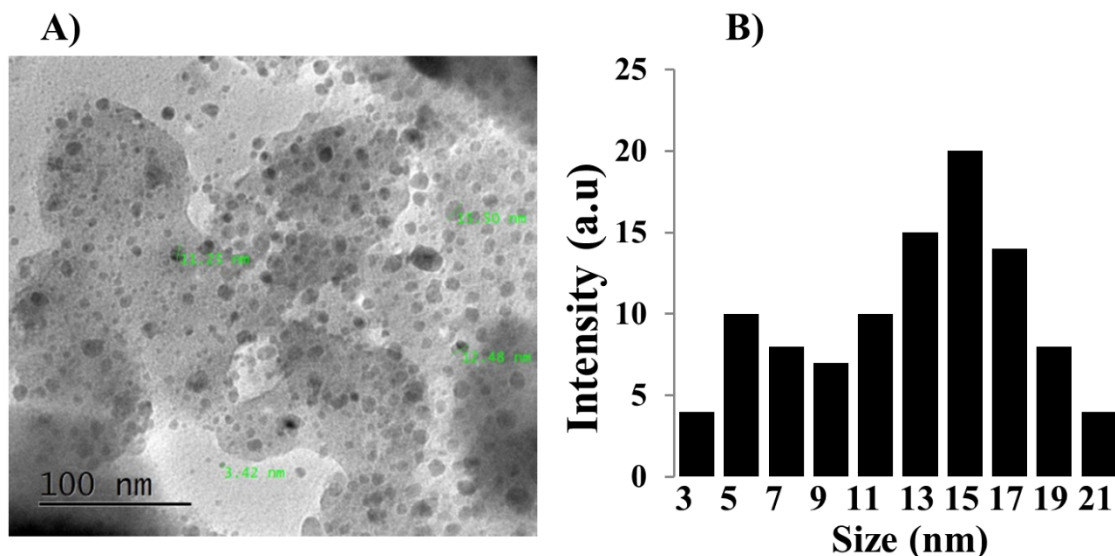


Fig. S16. A) TEM image of EC-S-Cu^{III}O 2 showing the Cu^{III}O nanoparticles are deposited on the cellulose. B) Their respective particle size distribution histogram showing the average size of the particle is around 15 nm.

ICP-MS data of EC-S-Cu^{III}O 2:

The loading of copper on EC-SH in catalyst **2** was found to be 41.2 wt%, as determined by ICP-MS.

C3. Characterisation of C-SH and C-S-Cu^{III}O 3

Characterisation of C-SH synthesised in Scheme S4, Section B3 were investigated by FT-IR, NMR, and SEM-EDX analyses. Whereas the C-S-Cu^{III}O **3** (Scheme S4, Section B3) was characterised by FT-IR, PXRD, TEM, and ICP-MS analyses. The details are discussed below.

FT-IR (C-SH, KBr): $\tilde{\nu}$ = 3574 (O–H stretching, s), 3425 (m), 3143 (m), 2904 (C–H symmetrical stretching, m), 2523 (–S–H, w), 1718 (C=O, s), 1656 (s), 1580, 1391 (s), 1286 (m), 1188 (m), 1061 (glucose and C–O stretching vibration in cellulose, m), 986 (m), 926 (w), 894 (w), 772 (s), 679 (s), 574 (w), 545 (w), 469 (w), 438 cm⁻¹ (w).

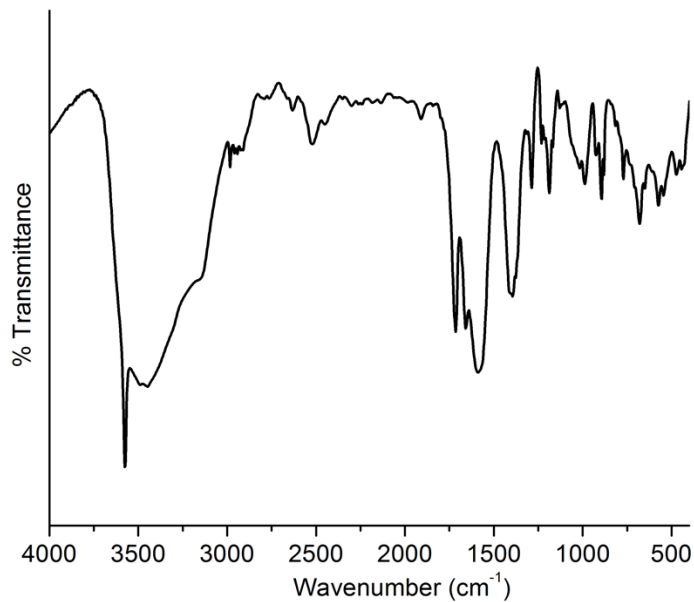


Fig. S17. FT-IR spectrum of C-SH.

FT-IR (C-S-Cu^{III}O **3, KBr):** $\tilde{\nu}$ = 3445 (-O-H, stretching, w), 2894 (C-H, w), 1720 (C=O, s), 1620 (m), 1418 (m), 1367 (m), 1275 (s), 1192 (s), 1156 (s), 1124 (s), 1056 (s), 1041 (s), 1004 (s), 894 (m), 817 (w), 661 (w), 596 (w), 564 (w), 518 cm^{-1} (S-S, w). The presence of bands at 661, 596, and 564 cm^{-1} are due to presence of CuO/Cu₂O in the FT-IR spectrum (Fig. S18) of catalyst **3** indicate different modes of bending/stretching vibration of the Cu-O bond of copper oxide NP.^{11,12}

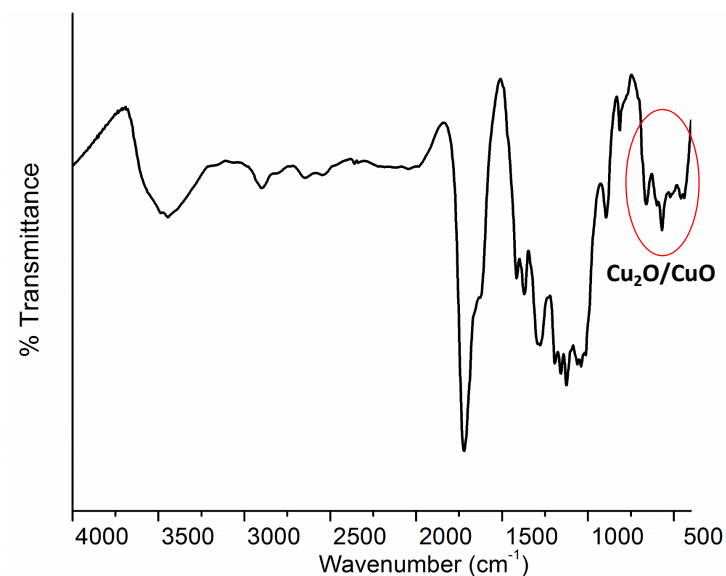


Fig. S18. FT-IR spectrum of C-S-Cu^{III}O **3**.

SEM-EDX data of C-SH

Energy dispersive X-ray (EDX) spectrum of C-SH was measured using Scanning Electron Microscope equipped with EDX facility (Fig. S19). The elemental composition and relative abundance are given in Table S3.

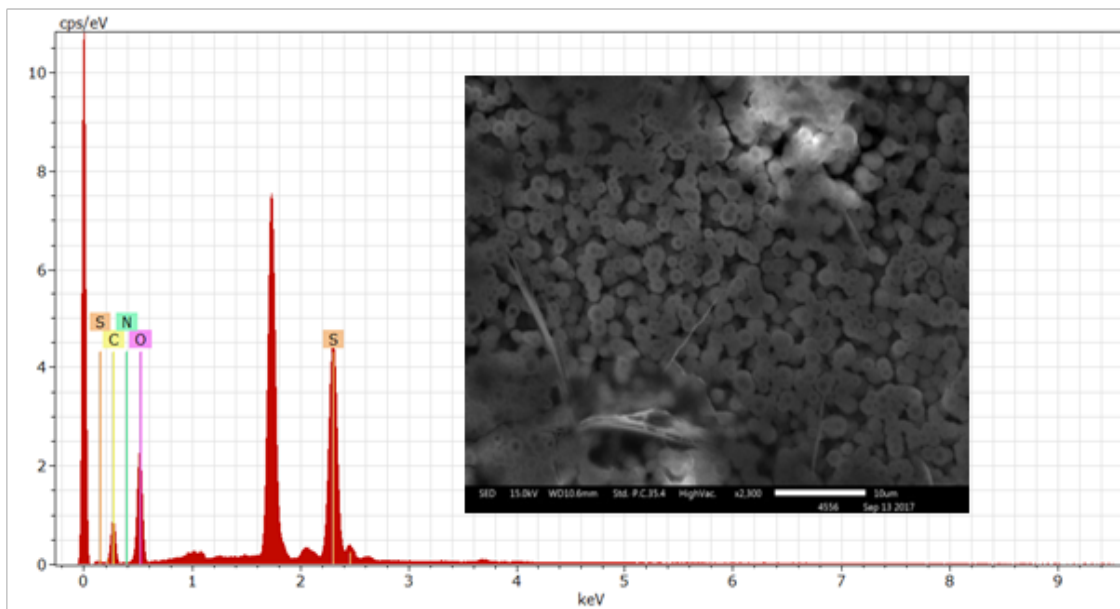


Fig. S19. Energy dispersive X-ray (EDX) spectrum of C-SH. (inset) Scanning electron microscopic image of C-SH (scale bare: 10µm).

Table S3. SEM-EDX measurement of C-SH.

Element	Kvalue	Weight (%)
		C-SH
Sulphur (S)	0.152 (K ₁)	14.81
	2.314 (K ₂)	
Oxygen (O)	0.525(K _α)	41.25
Carbon (C)	0.277(K _α)	43.94

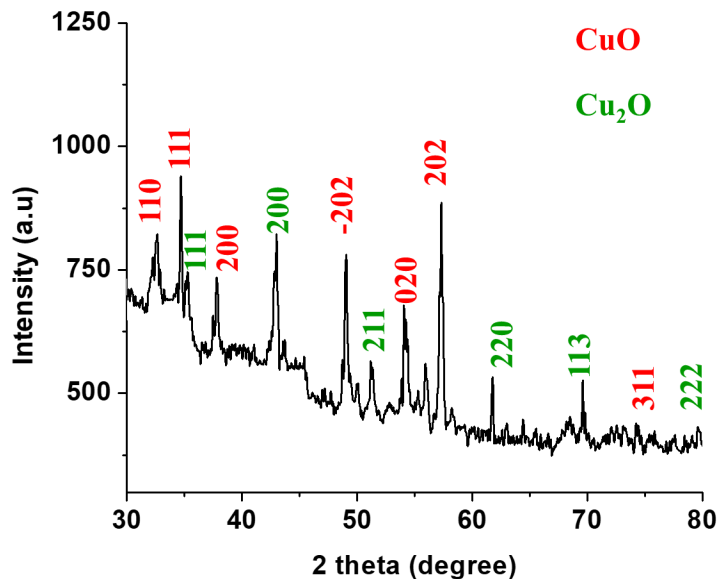


Fig. S20. PXRD spectrum of C-S-Cu^{II}O 3.

TEM data of C-S-Cu^{II}O 3.

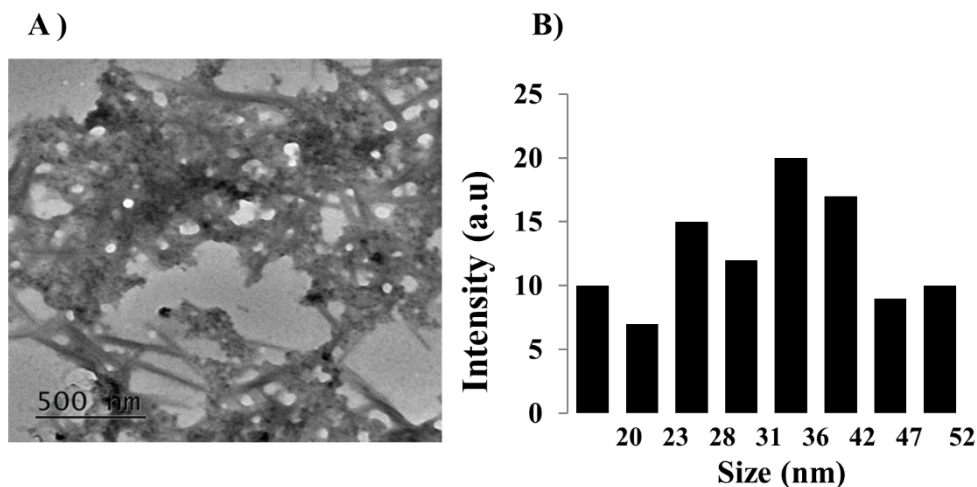


Fig. S21. A) TEM image of C-S-Cu^{II}O 3 showing the Cu^{II}O nanoparticles are deposited on the cellulose. B) Their respective particle size distribution histogram showing the average size of the particle is around 36 nm.

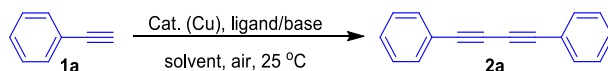
ICP-MS data of C-S-Cu^{II}O 3.

The loading of copper on C-SH in catalyst 3 was found to be 33.032 wt%, as determined by ICP-MS.

Section D: TC-S-Cu^{III}O **1** catalysed aerobic oxidation of homo-coupling of terminal alkynes

D1. Optimisation

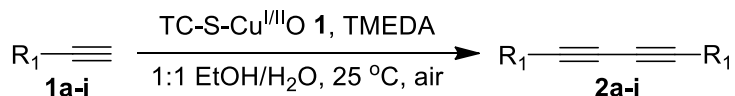
Table S4. Optimisation of reaction conditions for oxidative homo-coupling of ethynylbenzene.^a



entr y	Catalyst	solvent	Ligand/b ase	Time (min)	Yield ^b
1	TC-S-Cu ^{III} O 1	EtOH	TMEDA	2	98
2	TC-S-Cu ^{III} O 1	1:1 EtOH/H ₂ O	TMEDA	2	96
3	TC-S-Cu ^{III} O 1	1:1 MeCN/H ₂ O	TMEDA	15	91

^aethynylbenzene (0.5 mmol), TC-S-Cu^{III}O **1** (1 mol%), ligand (4 mol%), solvent (3 mL), air, 25 °C. ^bisolated yield in percentile.

D2. General procedure



An open Schlenk tube of 25 mL equipped with a magnetic stir bar was charged with TC-S-Cu^{III}O catalyst **1** (1 mol% of catalyst with respect to the amount of alkyne), TMEDA (4 mol%) in 1:1 EtOH:H₂O (3 mL). Then, ethynylbenzene **1a** (0.5 mmol, 1.0 equiv) was added. The reaction mixture was allowed to stirred at 25 °C for 5 min to 4 h depending upon the substrate. After completion of the reaction, 5 mL of CHCl₃ was added. Then the solution was washed with a saturated solution of NH₄Cl (3 mL) and dried over anhydrous Na₂SO₄. The solvent was removed in vacuum and the crude product was purified by flash column chromatography on silica gel to give the desired symmetrical 1,3-diyne **2a**.

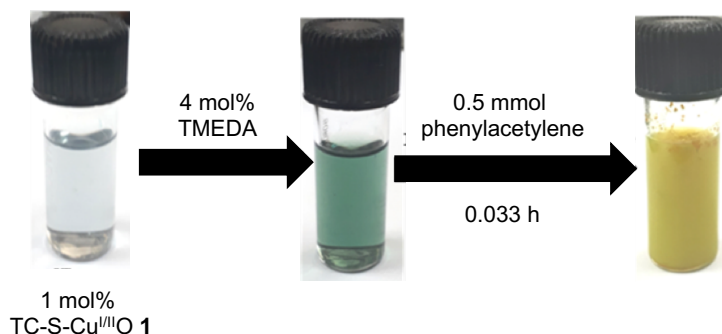
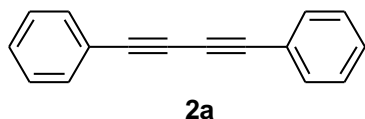


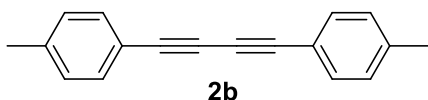
Fig. S22. Illustration of the progress of homo-coupling of ethynylbenzene with TC-S-Cu^{I/II}O 1/TMEDA catalytic system in 1:1 EtOH/H₂O solvent system.

D3. Spectral details of homo-products

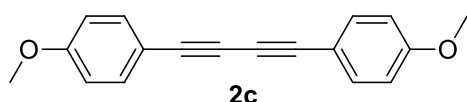
1,4-diphenylbuta-1,3-diyne ¹H NMR (400 MHz, CDCl₃): δ (ppm) = 7.32–7.39 (m, 4H), 7.53–7.56 (m, 6H); ¹³C NMR (100 MHz, CDCl₃): δ (ppm) = 74.1, 81.7, 121.9, 128.6, 129.3, 132.6.



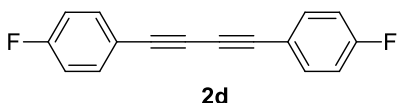
1,4-di-*p*-tolylbuta-1,3-diyne ¹H NMR (400 MHz, CDCl₃): δ (ppm) = 2.37 (s, 6H), 7.14 (d, *J* = 8.0 Hz, 4H), 7.42 (d, *J* = 8.1 Hz, 4H); ¹³C NMR (100 MHz, CDCl₃): δ (ppm) = 21.7, 73.5, 81.7, 118.8, 129.3, 132.5, 139.6.



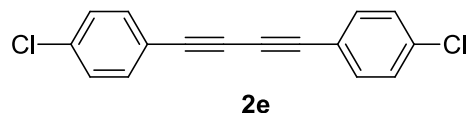
1,4-bis(4-methoxyphenyl)buta-1,3-diyne ¹H NMR (400 MHz, CDCl₃): δ (ppm) = 3.82 (s, 6H), 6.85 (d, *J* = 8.9 Hz, 4H), 7.46 (d, *J* = 8.9 Hz, 4H); ¹³C NMR (100 MHz, CDCl₃): δ (ppm) = 55.5, 73.1, 81.4, 114.1, 114.3, 134.3, 160.4.



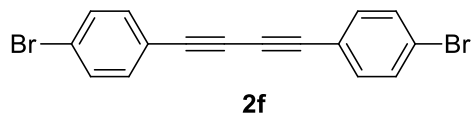
1,4-bis(4-fluorophenyl)buta-1,3-diyne ¹H NMR (400 MHz, CDCl₃): δ (ppm) = 7.04 (t, *J* = 8.7 Hz, 4H), 7.51 (dd, *J* = 8.1, 6.1 Hz, 4H); ¹³C NMR (100 MHz, CDCl₃): δ (ppm) = 73.8, 80.6, 116.1 (d, *J* = 22.3 Hz), 118.0 (d, *J* = 3.6 Hz), 134.7 (d, *J* = 8.6 Hz), 163.2 (d, *J* = 247.9 Hz).



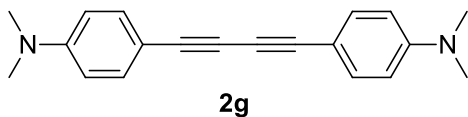
1,4-bis(4-chlorophenyl)buta-1,3-diyne $^1\text{H NMR}$ (400 MHz, CDCl_3): δ (ppm) = 7.26–7.30 (m, 4H), 7.72–7.77 (m, 4H); $^{13}\text{C NMR}$ (100 MHz, CDCl_3): δ (ppm) = 74.3, 87.4, 120.5, 123.8, 131.8, 133.9.



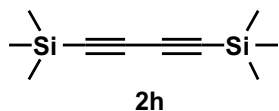
1,4-bis(4-bromophenyl)buta-1,3-diyne $^1\text{H NMR}$ (400 MHz, CDCl_3): δ (ppm) = 7.35 (d, J = 8.0 Hz, 4H), 7.47 (d, J = 8.0 Hz, 4H); $^{13}\text{C NMR}$ (100 MHz, CDCl_3): δ (ppm) = 74.9, 88.0, 121.2, 124.4, 132.4, 134.5.



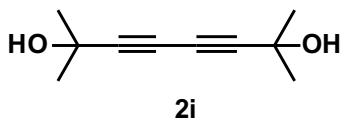
4,4'-(buta-1,3-diyne-1,4-diyl)bis(*N,N*-dimethylaniline) $^1\text{H NMR}$ (400 MHz, CDCl_3): δ (ppm) = 2.99 (s, 12H), 6.61 (d, J = 9.0 Hz, 4H), 7.39 (d, J = 8.9 Hz, 4H); $^{13}\text{C NMR}$ (100 MHz, CDCl_3): δ (ppm) = 40.2, 72.8, 82.5, 108.8, 111.8, 133.8, 150.5.



1,4-bis(trimethylsilyl)buta-1,3-diyne $^1\text{H NMR}$ (400 MHz, CDCl_3) δ (ppm) = 0.19 (s, 18H); $^{13}\text{C NMR}$ (100 MHz, CDCl_3): δ (ppm) = -0.4, 86.1, 88.1.



2,7-dimethylocta-3,5-diyne-2,7-diol $^1\text{H NMR}$ (400 MHz, CDCl_3) δ (ppm) = 1.40 (s, 12H), 5.44 (s, 2H); $^{13}\text{C NMR}$ (100 MHz, CDCl_3): δ (ppm) = 31.1, 65.6, 66.3, 84.0.



D4. ^1H - and ^{13}C -NMR, and GC-MS spectral profiles of homo-products

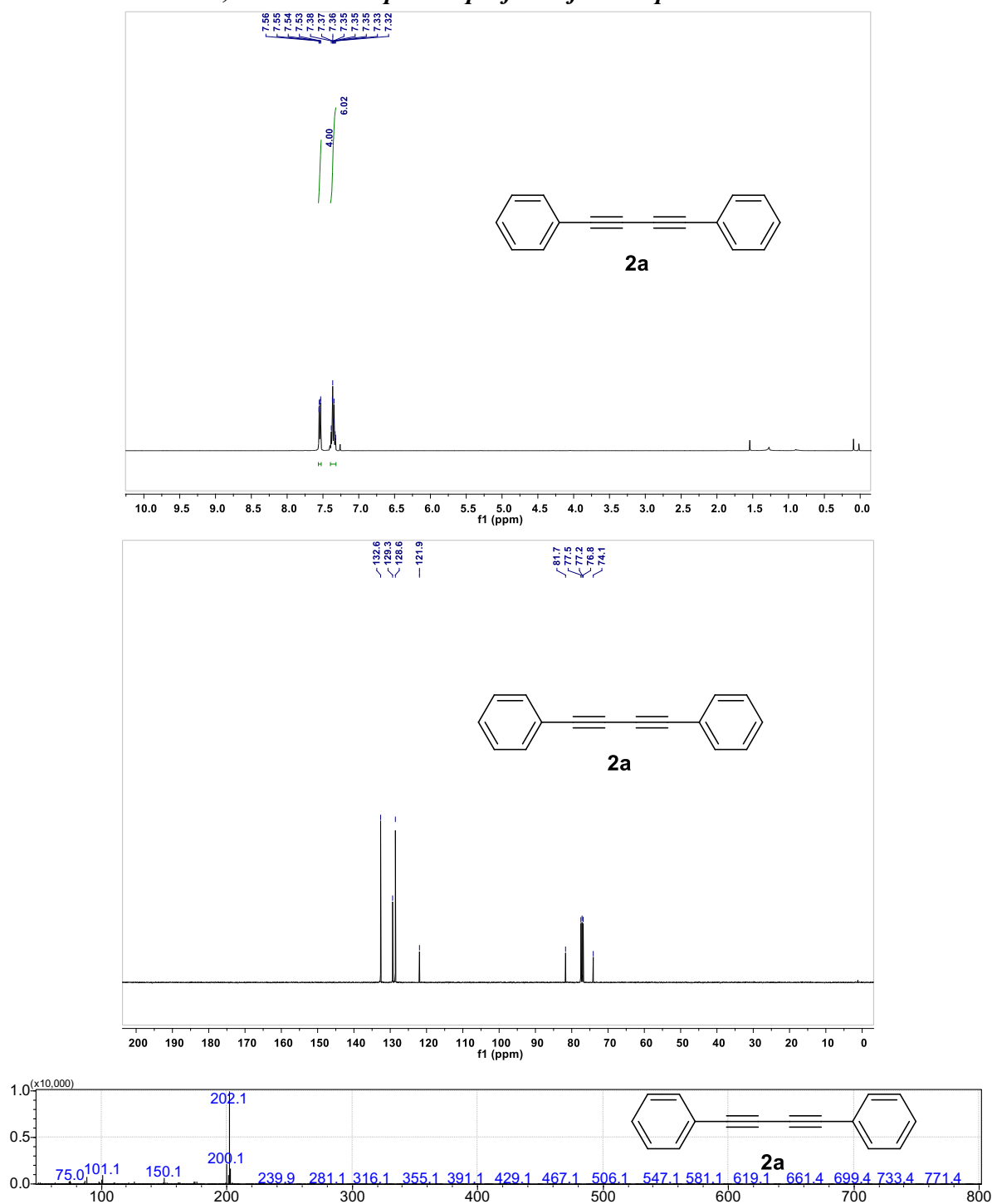


Fig. S23. ^1H - (400 MHz, CDCl_3 , 298 K), and ^{13}C -NMR (100 MHz, CDCl_3 , 298 K) and GC-MS spectra of **2a**.

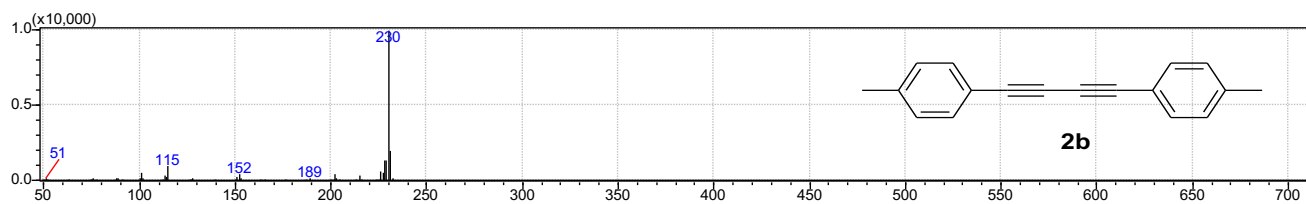
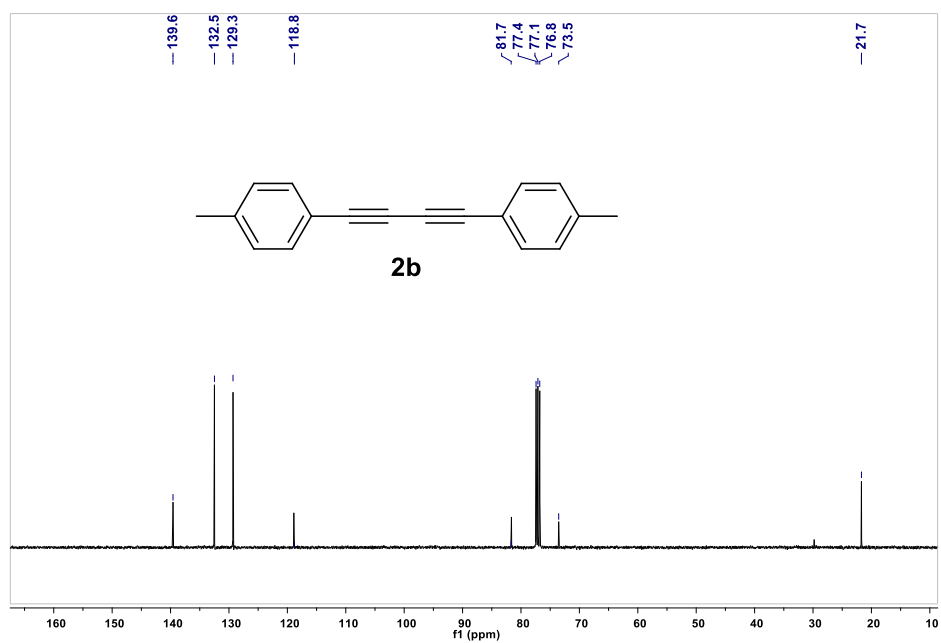
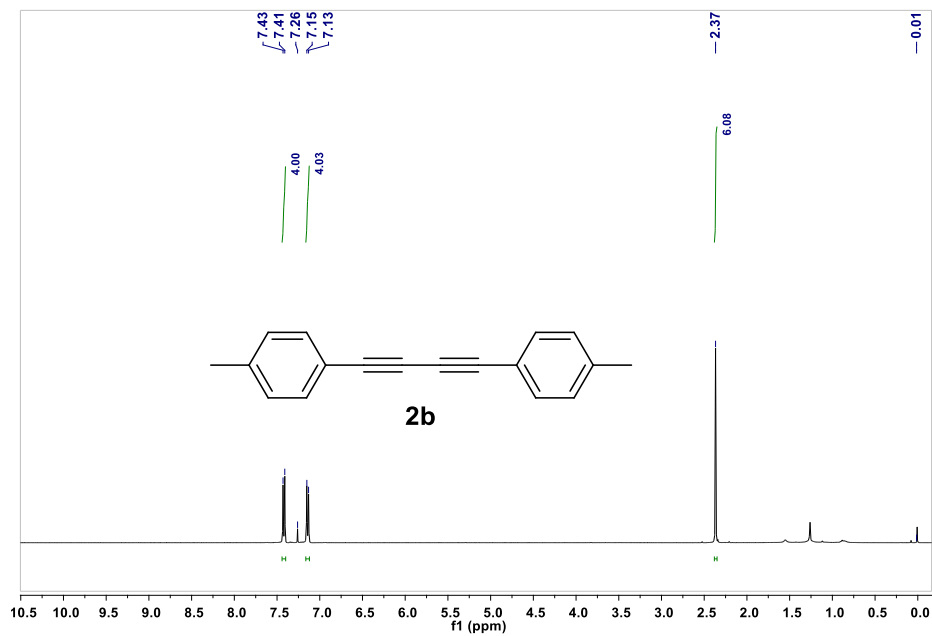


Fig. S24. ¹H- (400 MHz, CDCl₃, 298 K), and ¹³C-NMR (100 MHz, CDCl₃, 298 K) and GC-MS spectra of **2b**.

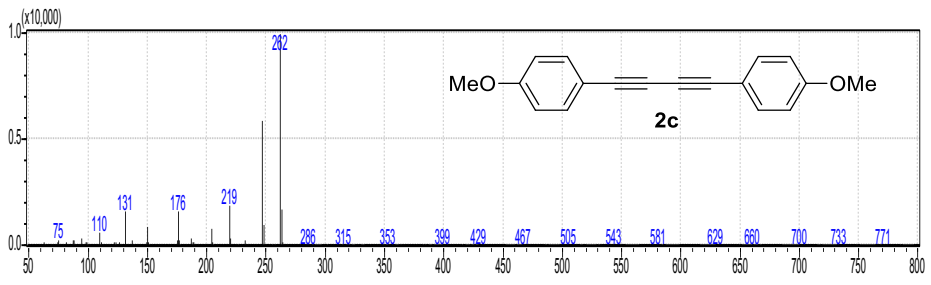
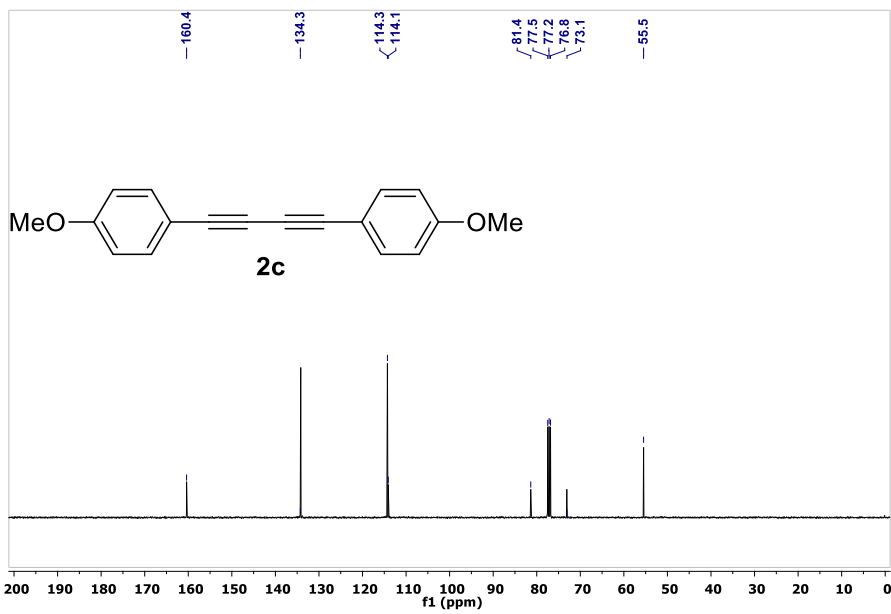
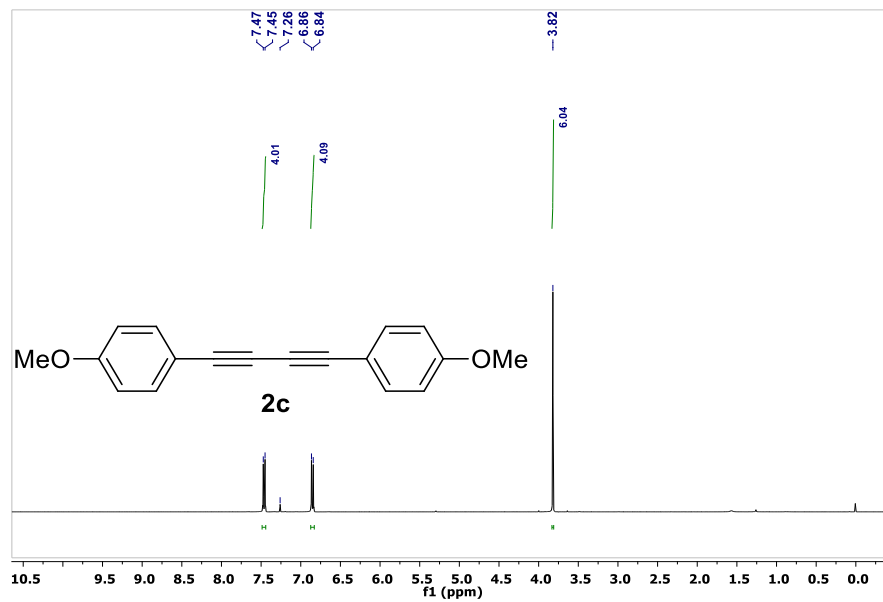


Fig. S25. ¹H- (400 MHz, CDCl₃, 298 K), and ¹³C-NMR (100 MHz, CDCl₃, 298 K) and GC-MS spectra of **2c**.

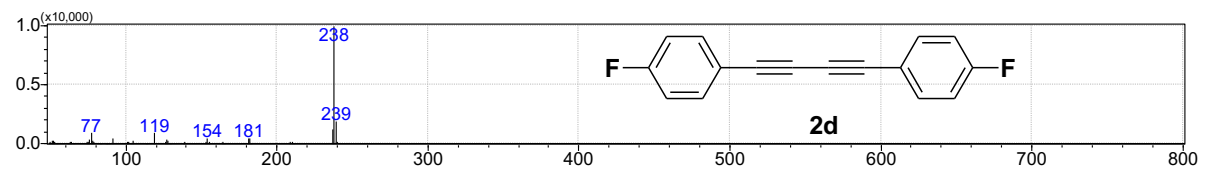
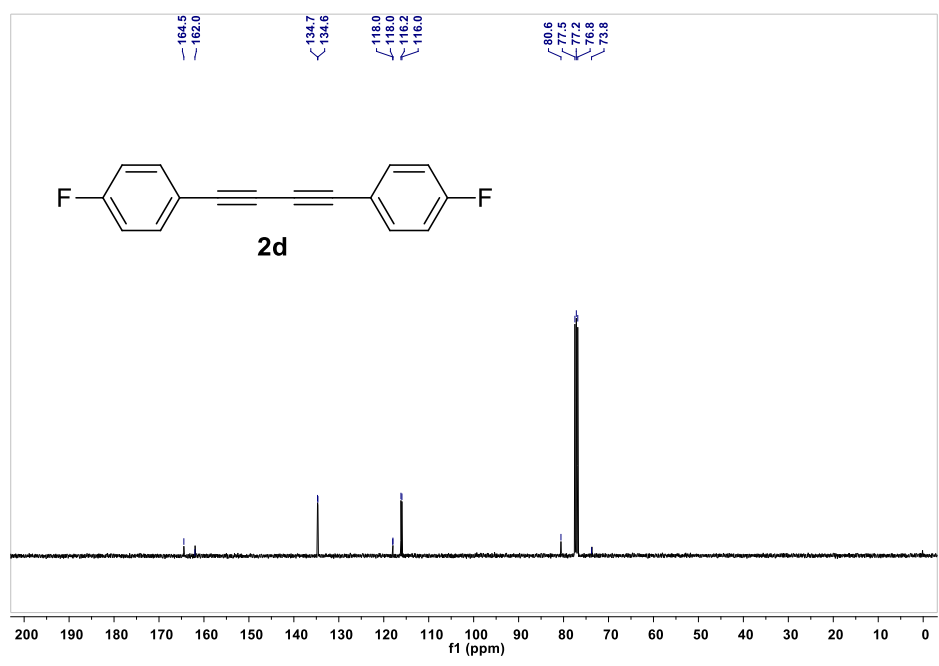
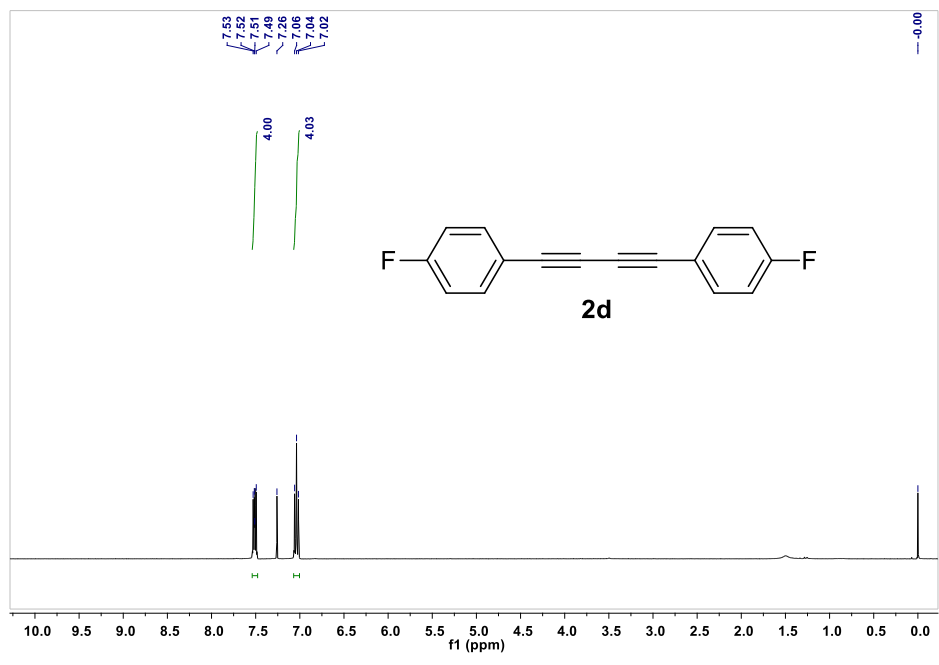
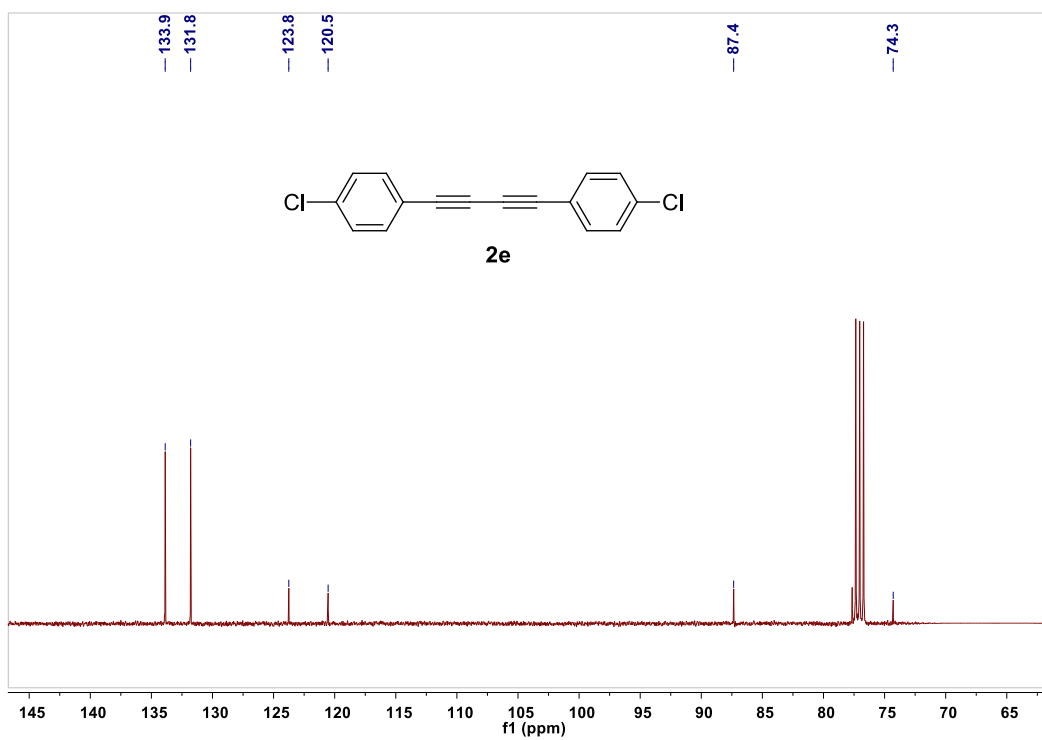
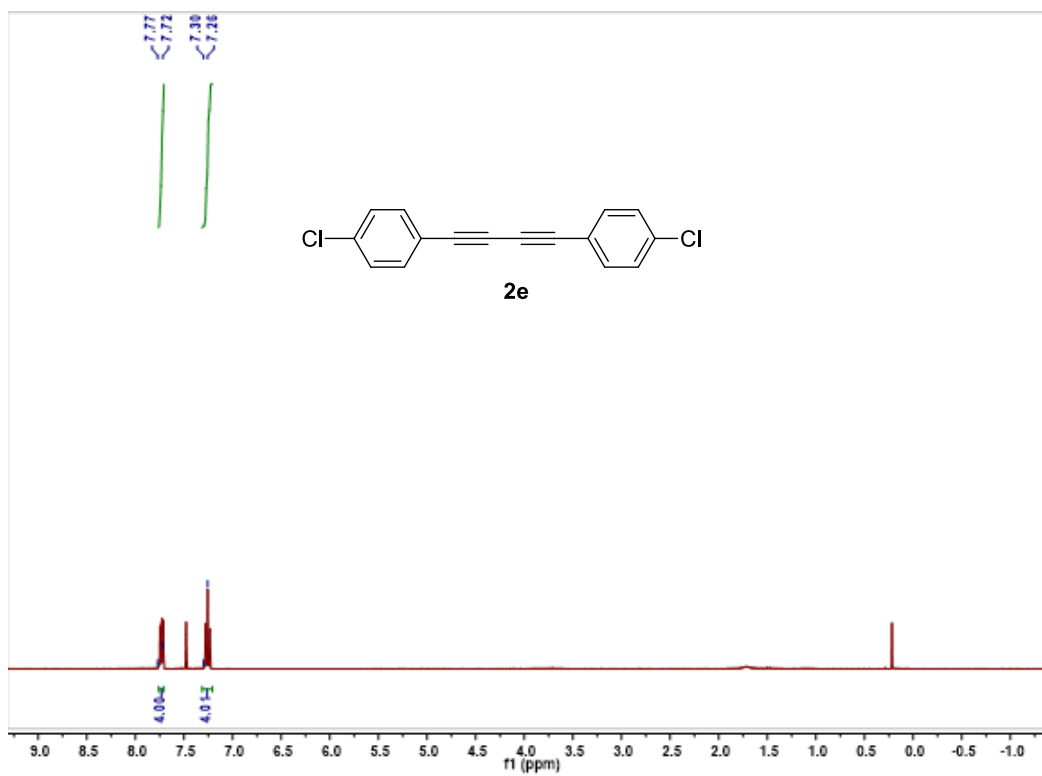


Fig. S26. ¹H- (400 MHz, CDCl₃, 298 K), and ¹³C-NMR (100 MHz, CDCl₃, 298 K) and GC-MS spectra of **2d**.



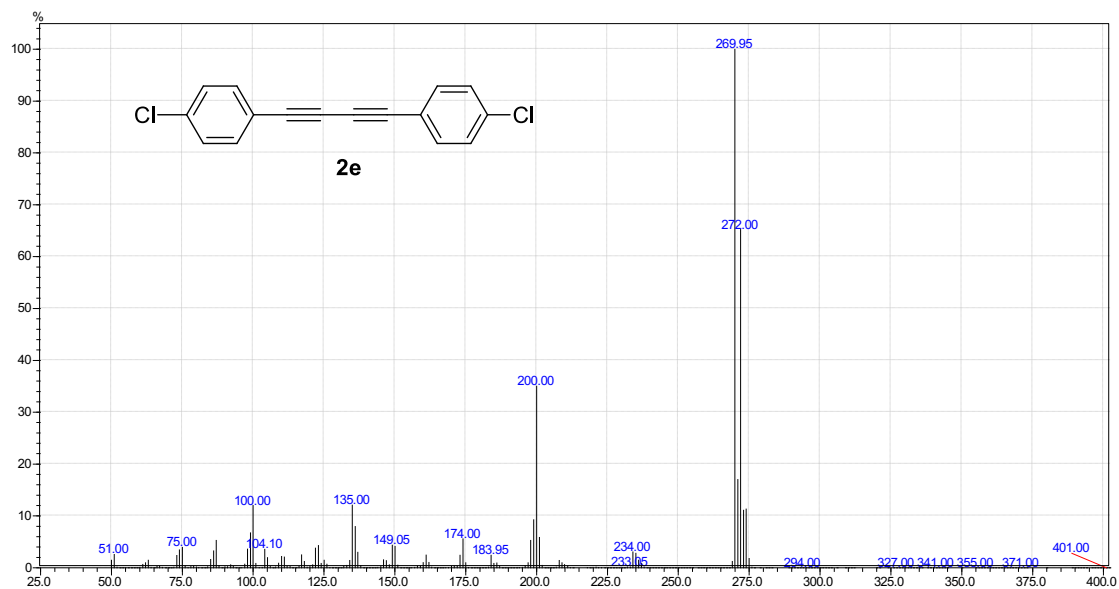
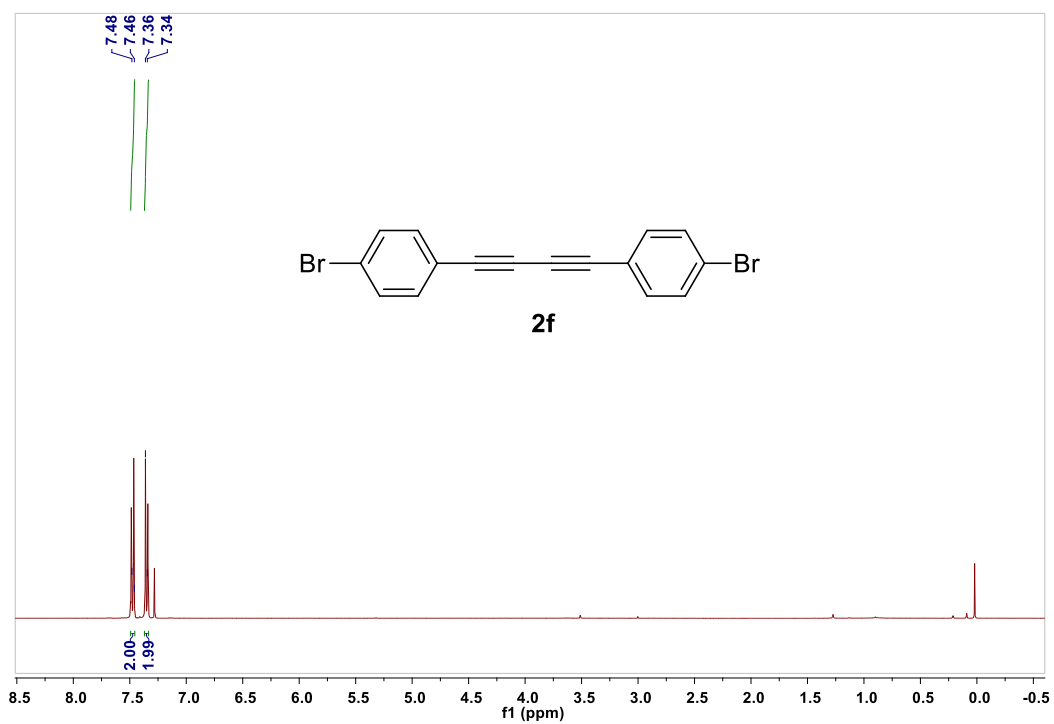


Fig. S27. ^1H - (400 MHz, CDCl_3 , 298 K), and ^{13}C -NMR (100 MHz, CDCl_3 , 298 K) and GC-MS spectra of **2e**.



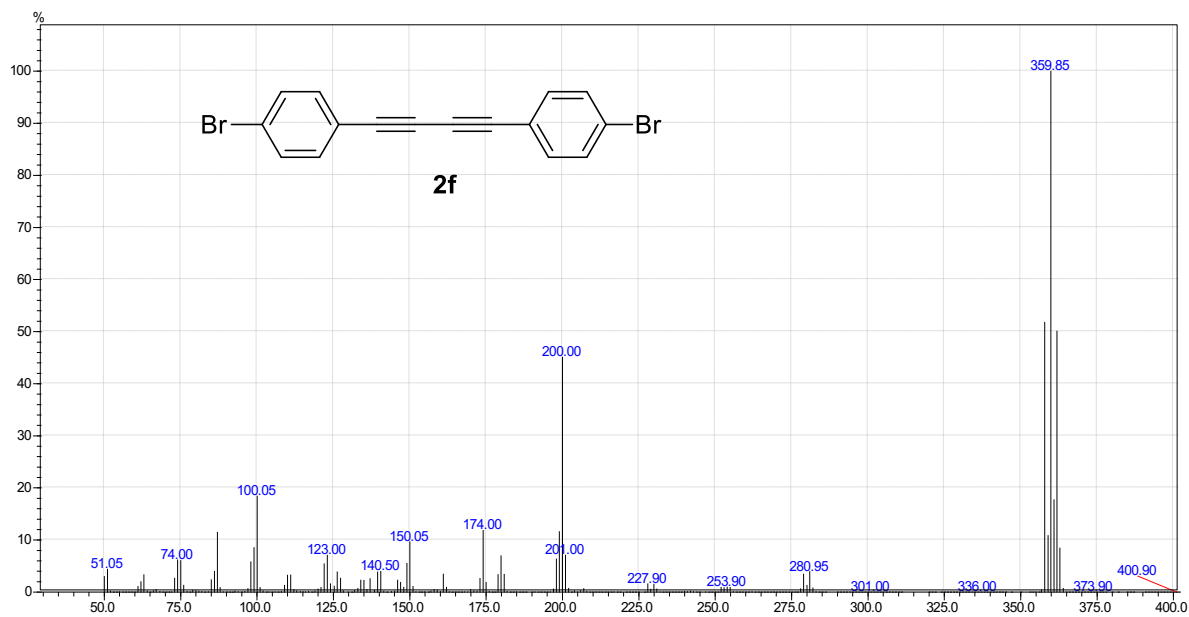
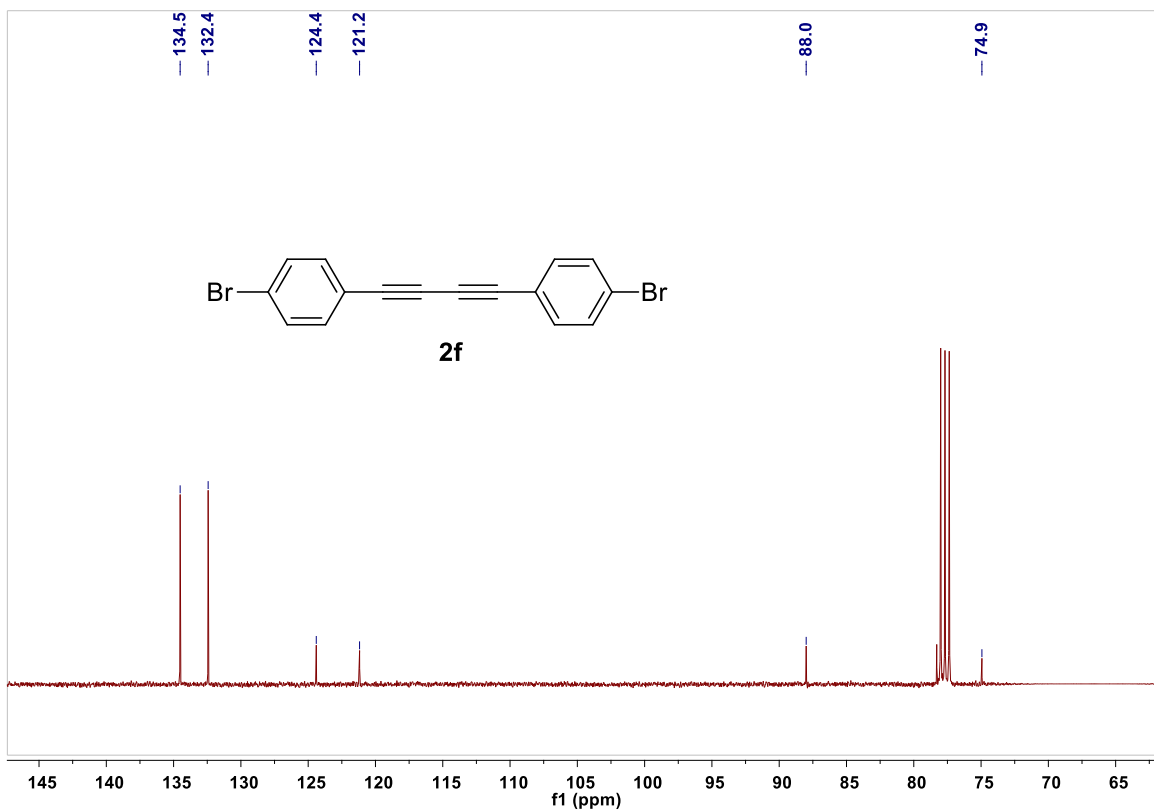


Fig. S28. ¹H- (400 MHz, CDCl₃, 298 K), and ¹³C-NMR (100 MHz, CDCl₃, 298 K) and GC-MS spectra of **2f**.

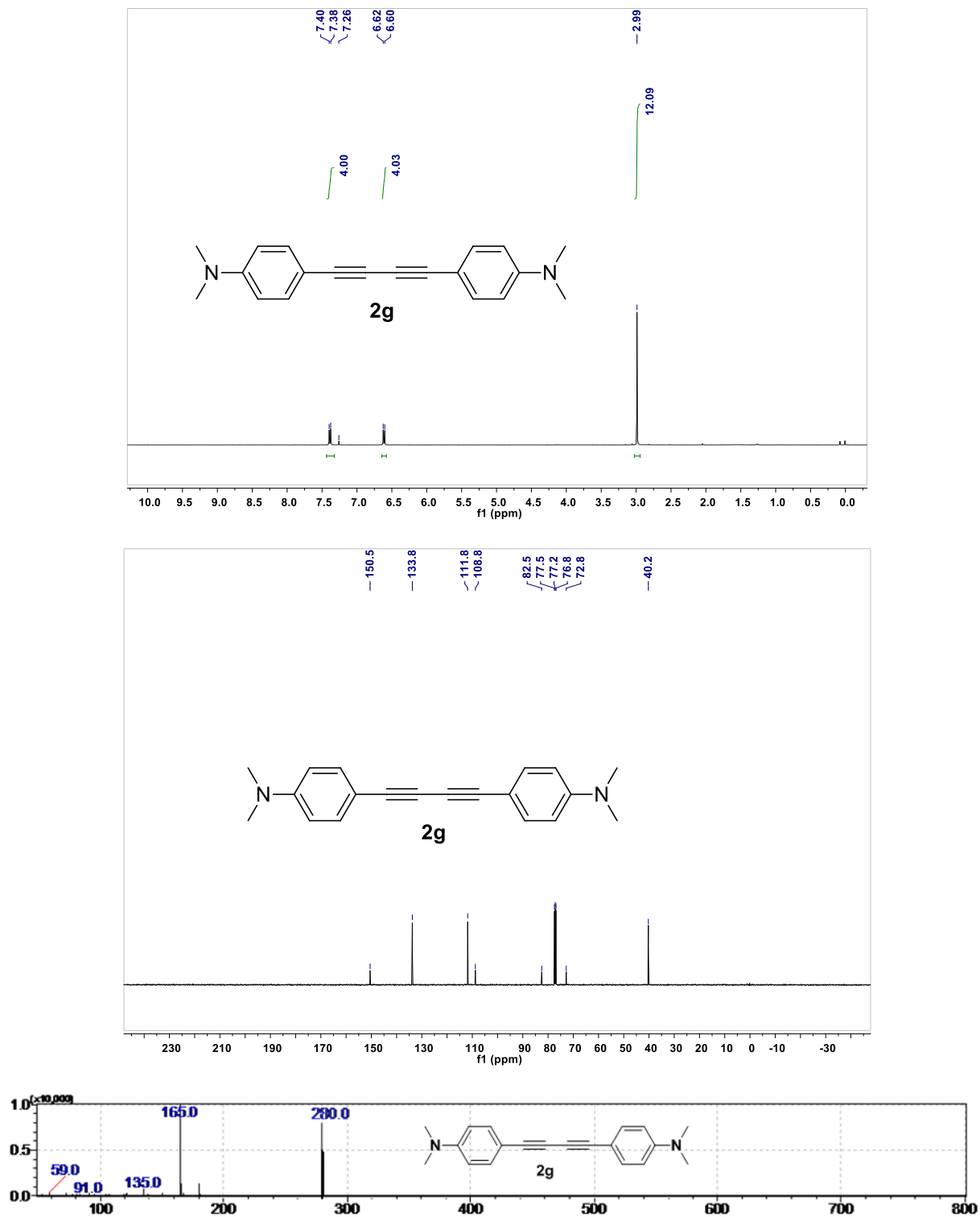


Fig. S29. ^1H - (400 MHz, CDCl_3 , 298 K), and ^{13}C -NMR (100 MHz, CDCl_3 , 298 K) and GC-MS spectra of **2g**.

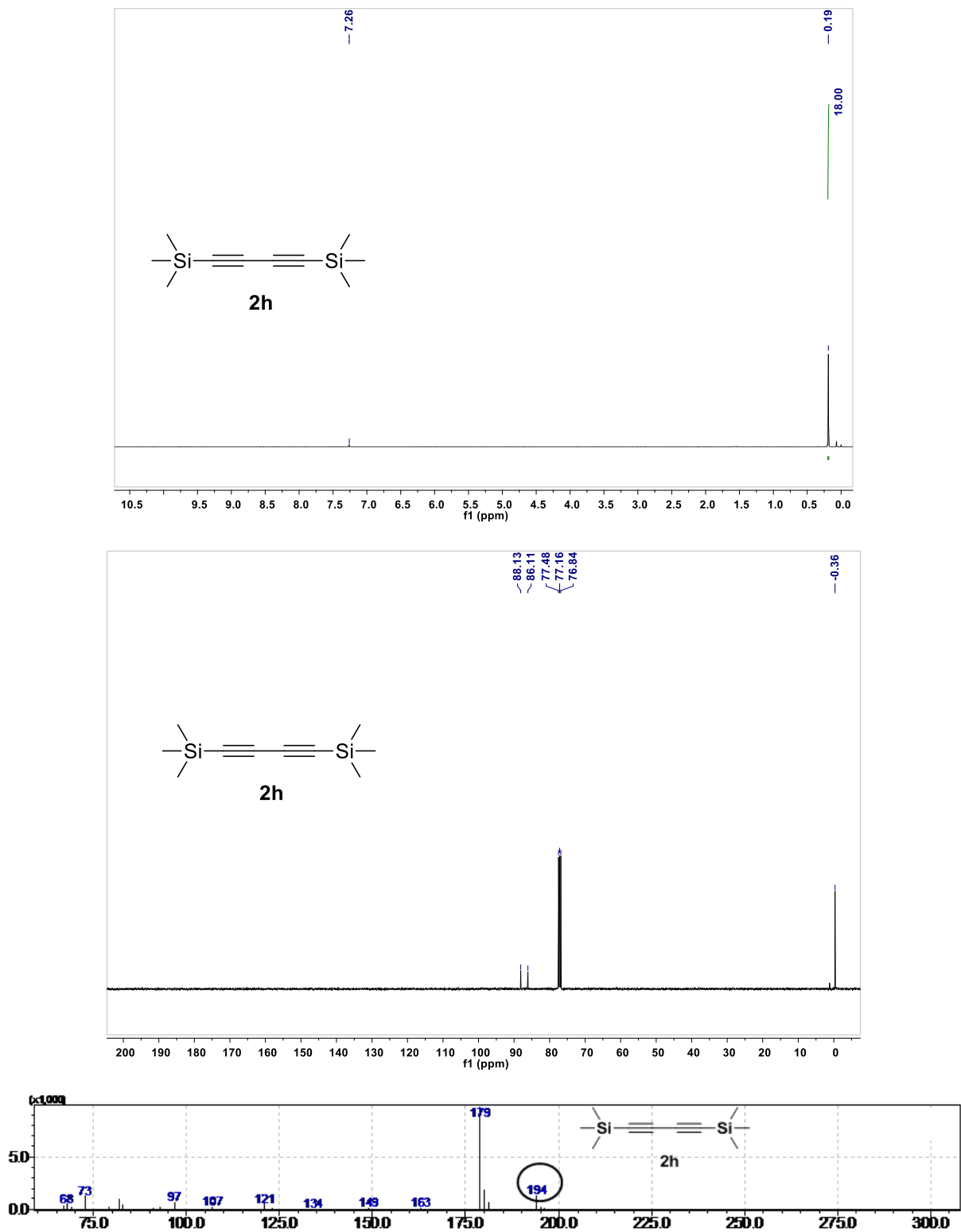


Fig. S30. ^1H - (400 MHz, CDCl_3 , 298 K), and ^{13}C -NMR (100 MHz, CDCl_3 , 298 K) and GC-MS spectra of **2h**.

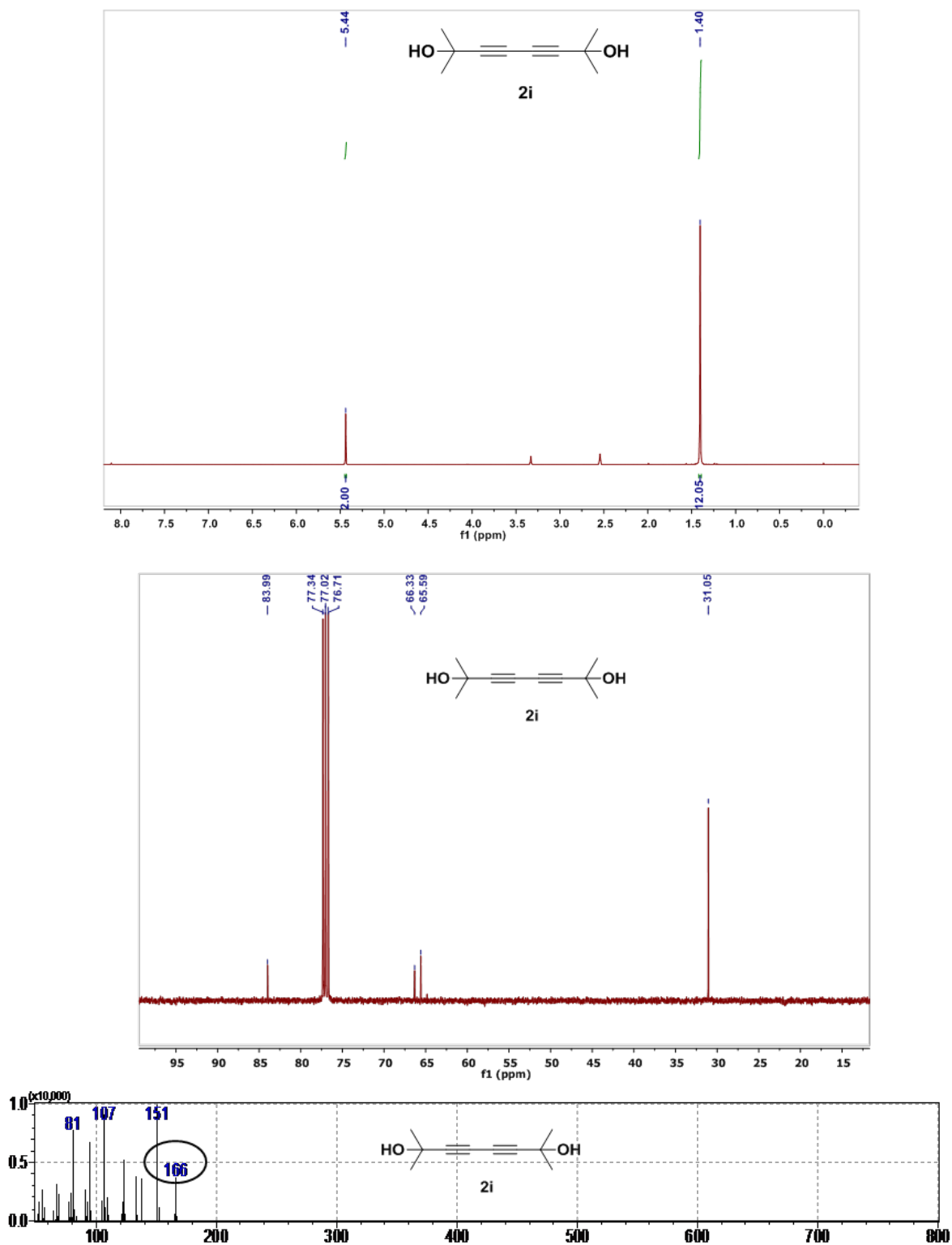


Fig. S31. $^1\text{H-}$ (400 MHz, CDCl_3 , 298 K), and $^{13}\text{C-NMR}$ (100 MHz, CDCl_3 , 298 K) and GC-MS spectra of **2i**.

D5. Oxidative homo-coupling of ethynylbenzene and catalytic amount variability study

- i) Comparison of TOF of TC-S-Cu^{III}O 1 with commercial catalyst for oxidative homo-coupling of ethynylbenzene.^a

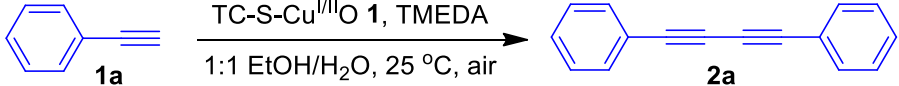
Table S5.

Entry	Catalysts	Ligand	Time (h)	Yield (%) ^b	TON ^c	TOF ^d
1	TC-S-Cu ^{III} O 1	TMEDA	0.033	96	96	2909
2	Cu-TMEDA (Sigma-Aldrich :CAS- 30698-64-7)	-	0.67	92	92	139

^aReaction conditions: ethynylbenzene **1a** (0.5 mmol), Cu-catalyst (1 mol% of Cu with respect to the amount of **1a** based on ICP-MS), 1:1 EtOH/H₂O (3 mL), 25 °C, air. ^bValues refer to yields of isolated product **2a**. ^cTON (number of moles of **1a** converted per mole of copper). ^dTOF (TON per time taken in hour).

- ii) Oxidative homo-coupling of ethynylbenzene using various amounts of catalyst **1**.^a

Table S6.

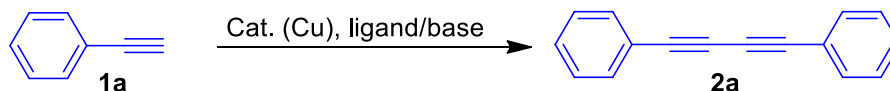


Entry	TC-S-Cu ^{III} O 1 (mol%)	yield (%) ^b	Time (h)	TON	TOF (h ⁻¹)
1	10	99	0.033	9.9	300
2	1	96	0.033	96	2909
3	0.1	96	0.75	960	12667
4	0.01	95	2	9500	4750
5	0.001	90	8	90000	11250
6	0.0001	85	18	85000	4722

^aReactions were carried out using 0.5 mmol of **1a** in the presence of various amounts of catalyst **1**, 1:1 EtOH/H₂O (3 mL), 25 °C, open air. ^byield was determined by GC-MS.

D6. Comparison of catalytic activity of present catalyst TC-S-Cu^{I/II}O 1 with other reported catalysts in literature for the homo-coupling of ethynylbenzene.

Table S7.



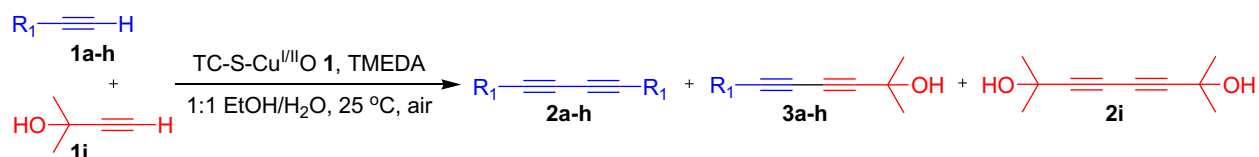
Entry	Catalyst	Solvent	Oxidant	Temp (°C)	Mol (%)	Time (h)	Yield (%)	TON	TOF (h ⁻¹)	Ref
1.	TC-S-Cu ^{I/II} O 1, TMEDA	1:1 EtOH/H ₂ O	Air	25	1	0.033	96	96	2909	a
2.	CuOx nanoparticles	toluene	O ₂	90	8	0.75	100	12.5	17	b
3.	Au Clusters on Amino-SiO ₂ , 1,10-phen,	CH ₂ Cl ₂	PhI(OAc) ₂	25	1	18	96	96	5.3	c
4.	Cu/MnO _x	toluene	Air	105	6	1	97	16.7	16.7	d
5.	Polyacrylonitrile, CuI, <i>n</i> BuNH ₂	EtOAc	Air	25	2	12	98	49	4.1	e
6.	Pd ^{II} /AgNO ₃ , Cs ₂ CO ₃	4:1 <i>n</i> BuOH/H ₂ O	Air	60	0.5	24	99	198	8.3	f
7.	HCP-NHC-Cu III, TMEDA	EtOH	O ₂	105	0.36	8	99	275	34.4	g
8.	CuCl ₂ , TMEDA	DMF	N ₂	40	0.5	2	97	194	97	h
9.	Cu ⁿ⁺ -M ³⁺ -Cu ⁿ⁺	piperidine	Air	125	5	4	98	19.6	4.9	i
10.	PdCl ₂ (PPh ₃) ₂ , K ₂ CO ₃	-	-	25	2.5	6	90	36	6	j
11.	Cu@SiO ₂ , base	toluene	O ₂	100	2	2.5	96	48	19.2	k
12.	SBA-15/DABCO-Pd, CuI	MeCN	Air	40	0.05	4	63	630	158	l
13.	CuCl, 20% TMEDA	Solkane®365 mfc	Air	25	10	1	93	9.3	9.3	m
14.	CuCl ₂ , Et ₃ N	toluene	Air	60	3	6	99	33	5.5	n
15.	CuCl, TMEDA, DIPEA, CAN	CH ₃ CN	Air	25	2	24	90	45	1.9	o
16.	Cu(OH) _x /TiO ₂	toluene	O ₂	100	5	0.5	90	18	36	p
17.	Cu-Zeolites	DMF	Air	110	30	15	78	2.6	0.17	q
18.	CuI	DMF	I ₂	80	100	3	99	0.99	0.33	r
19.	di-Cu-Substituted Silicotungstate	PhCN	O ₂	100	2.2	3	91	41.4	13.8	s
20.	CuCl ₂ , NaOAc	scCO ₂ , MeOH	-	40	200	3	100	0.5	0.16	t
21.	Fe(acac) ₃ /Cu(acac) ₂ , K ₂ CO ₃	DMF	Air	50	1	8	94	94	11.8	u
22.	CuCl ₂ /DBU	THF	Air	25	10	24	92	9.2	0.38	v
23.	Cu/C ₃ N ₄ , KOH	<i>i</i> PrOH	O ₂	25	20	12	99	4.95	0.41	w
24.	Cu ₂ (ophen) ₂ , TBAB	H ₂ O	Air	25	5	10	95	19	1.9	x
25.	Cu-TMEDA	1:1 EtOH/H ₂ O	Air	25	1	0.67	92	92	139	y

References for Table S7.

a. Present Manuscript.

- b. Liu, L.; Matsushita, T.; Concepción, P.; Leyva-Pérez, A.; Corma, A. *ACS Catal.* **2016**, *6*, 2211–2221.
- c. Vilhanová, B.; Václavík, J.; Artiglia, L.; Ranocchiari, M.; Togni, A.; van Bokhoven, J. A. *ACS Catal.* **2017**, *7*, 3414–3418.
- d. Biswas, S.; Mullick, K.; Chen, S.; A. Kriz, D.; Shakil, Md.; Kuo, C.; M. Angeles-Boza, A.; R. Rossi, A.; L. Suib, S. *ACS Catal.* **2016**, *6*, 5069–5080.
- e. Shi, XL.; Hu, Q.; Wang, F.; Zhang, W.; Duan P. *J. Catal.* **2016**, *337*, 233–239.
- f. Guo, M.; Chen, B.; Lv, M.; Zhou, X.; Wen, Y.; Shen, X. *Molecules* **2016**, *21*, 606 (1)–606 (7).
- g. Jia, Z.; Wang, K.; Li, T.; Tan, B.; Gu, Y. *Catal. Sci. Technol.* **2016**, *6*, 4345(1)–4345(12).
- h. Zhang, G.; Yi, H.; Zhang, G.; Deng, Y.; Bai, R.; Zhang, H.; T. Miller, J.; J. Kropf, A.; E. Bunel, E.; Lei, A. *J. Am. Chem. Soc.* **2014**, *136*, 924–926.
- i. Srivastava, S.; Ali, A.; Tyagi, A.; Gupta, R. *Eur. J. Inorg. Chem* **2014**, 2113–2123.
- j. Chen, L.; E. Lemma, B.; S. rich, J.; Mack, J. *Green Chem.* **2014**, *16*, 1101–1103.
- k. Van Gelderen, L.; Rothenberg, G.; Roberto Calderone, V.; Wilson, K.; Raveendran, Shiju, N. *Appl. Organometal. Chem.* **2013**, *27*, 23–27.
- l. Li, H.; Yang, M.; Pu, Q. *Microporous Mesoporous Mater.* **2012**, *148*, 166–173.
- m. Kusuda, A.; Xu, X.; Wang, X.; Tokunaga, e.; Shibata, N. *Green Chem.* **2011**, *13*, 843–846.
- n. Wang, D.; Li, J.; Gao, T.; Hou, S.; Chen, B. *Green Chem.* **2010**, *12*, 45–48.
- o. Adimurthy, S.; C. Malakar, C.; Beifuss, U. *J. Org. Chem.* **2009**, *74*, 5648–5651.
- p. Oishi, T.; Katayama, T.; Yamaguchi, K.; Mizuno, N. *Chem. Eur. J.* **2009**, *15*, 7539–7542.
- q. Kuhn, P.; Alix, A.; Kumarraja, M.; Louis, B.; Pale, P.; Sommer, J. *Eur. J. Org. Chem.* **2009**, 423–429.
- r. Li, D.; Yin, K.; Li, J.; Jia, X. *Tetrahedron Lett.* **2008**, *49*, 5918–5919.
- s. Kamata, K.; Yamaguchi, S.; Kotani, M.; Yamaguchi, K.; Mizuno, N. *Angew. Chem. Int. Ed.* **2008**, *47*, 2407–2410.
- t. Jiang, H.; Tang, J.; Wang, A.; Deng, G.; Yang, S. *Synthesis* **2006**, *7*, 1155–116.
- u. Meng, X.; Li, C.; Han, B.; Wang, T.; Chen, B. *Tetrahedron* **2010**, *66*, 4029–4031.
- v. Balamurugan, R.; Naveen, N.; Manojveer, S.; Nama, M. V. *Aust. J. Chem.* **2011**, *64*, 567–575.
- w. Xu, H.; Wu, K.; Tian, J.; Zhu, L.; Yao, X. *Green Chem.* **2018**, *20*, 793–797.
- x. Zhang, L.-J.; Wang, Y.-H.; Liu, J.; Xu, M.-C.; Zhang, X.-M. *RSC Adv.* **2016**, *6*, 28653–28657.
- y. Catalyst obtained from Sigma-Aldrich (CAS: 30698-64-7).

Section E: TC-S-Cu^{III}O 1 catalysed aerobic oxidative cross-coupling of terminal alkynes

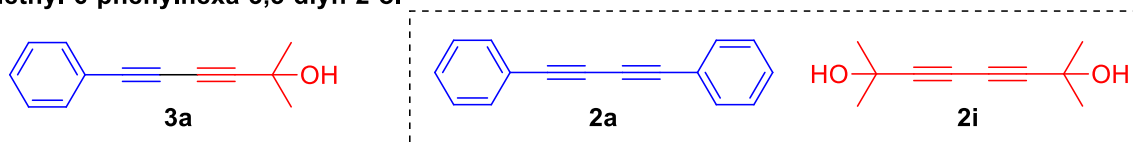


E1. General procedure

Round bottom flask of 25 mL equipped with a magnetic stir bar was charged with TC-S-Cu^{III}O **1** (1 mol%), TMEDA (4 mol%) in 3 mL of 1:1 EtOH/H₂O. Then, terminal alkynes **1a-h** (0.2 mmol, 1 equiv.) and **1i** (0.26 mmol, 1.3 equiv.) were added. The reaction mixture was stirred at 25 °C. After completion of the reaction, 4 mL of CHCl₃ was added. Then the solution was washed with a saturated solution of NH₄Cl (3 mL), and dried over anhydrous Na₂SO₄ and concentrated in vacuum. The crude product was purified by column chromatography on silica gel to give the desired unsymmetrical 1,3-diyne **3a-h** (medium-polar *cross-Glaser*-product).

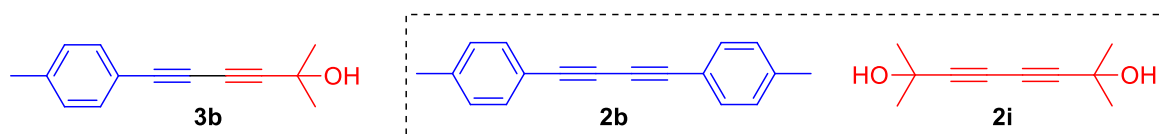
E2. Spectral details of cross-Glaser-products

2-methyl-6-phenylhexa-3,5-diyne-2-ol



Following the above general procedure, when 0.2 mmol **1a** and 0.26 mmol **1i** were used, the crude product **3a** was purified by column chromatography on silica gel and eluted with ethyl acetate/hexane 1:5 to afford **3a** as a white solid in 79% isolated yield. The selectivity between the homo- and cross-Glaser-products was estimated based on the GC-MS analysis, which is in the ratio of 85:10:05 (%) for **3a/2a/2i**, respectively. ¹H NMR (**3a**, 400 MHz, CDCl₃): δ (ppm) = 1.58 (s, 6H), 2.13 (s, 1H), 7.29 – 7.37 (m, 3H), 7.48 (d, J = 8 Hz, 2H); ¹³C NMR (100 MHz, CDCl₃): δ (ppm) = 31.1, 65.8, 67.1, 73.2, 78.8, 86.7, 121.6, 128.4, 129.3, 132.5.

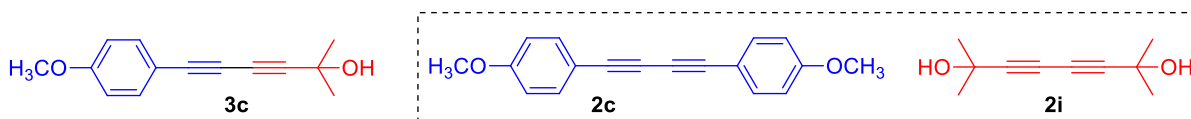
2-methyl-6-*p*-tolylhexa-3,5-diyne-2-ol



Following the above general procedure, when 0.2 mmol **1b** and 0.26 mmol **1i** were used, the crude product **3b** was purified by column chromatography on silica gel and eluted with ethyl acetate/hexane 1:5 to afford **3b** as a pale yellow solid in 75% isolated yield. The selectivity between the homo- and cross-Glaser-products was estimated based on the GC-MS analysis, which

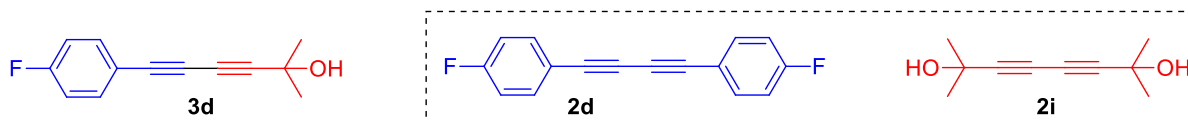
is in the ratio of 81:13:06 (%) for **3b/2b/2i**, respectively. ^1H NMR (**3b**, 400 MHz, CDCl_3): δ (ppm) = 1.57 (s, 6H), 2.28 (s, 1H), 2.35 (s, 3H), 7.12 (d, $J = 8$ Hz, 2H), 7.37 (d, $J = 8$ Hz, 2H); ^{13}C NMR (100 MHz, CDCl_3): δ 21.6, 31.2, 65.8, 67.2, 72.5, 79.1, 86.3, 118.4, 129.3, 132.4, 139.7.

6-(4-methoxyphenyl)-2-methylhexa-3,5-diyne-2-ol



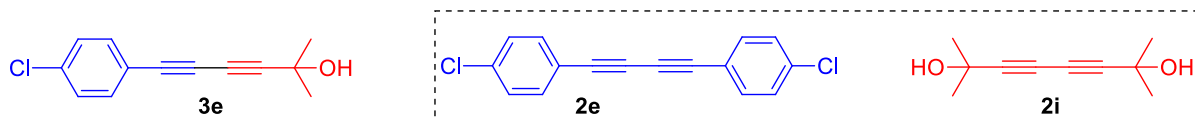
Following the above general procedure, when 0.2 mmol **1c** and 0.26 mmol **1i** were used, the crude product **3c** was purified by column chromatography on silica gel and eluted with ethyl acetate/hexane 1:5 to afford **3c** as a white solid in 70% isolated yield. The selectivity between the homo- and cross-Glaser-products was estimated based on the GC-MS analysis, which is in the ratio of 72:20:08 (%) for **3c/2c/2i**, respectively. ^1H NMR (**3c**, 400 MHz, CDCl_3): δ (ppm) = 1.57 (s, 6H), 2.28 (s, 1H), 3.80 (s, 3H), 6.83 (d, $J = 8.9$ Hz, 2H), 7.41 (d, $J = 8.9$ Hz, 2H); ^{13}C NMR (100 MHz, CDCl_3): δ (ppm) = 31.3, 55.4, 65.8, 67.4, 72.1, 79.1, 86.3, 113.6, 114.2, 134.2, 160.4.

6-(4-fluorophenyl)-2-methylhexa-3,5-diyne-2-ol

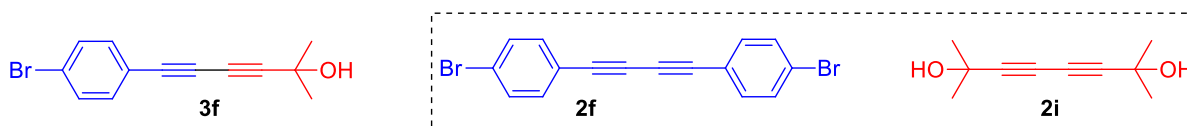


Following the above general procedure, when 0.2 mmol **1d** and 0.26 mmol **1i** were used, the crude product **3d** was purified by column chromatography on silica gel and eluted with ethyl acetate/hexane 1:5 to afford **3d** as a white solid in 78% isolated yield. The selectivity between the homo- and cross-Glaser-products was estimated based on the GC-MS analysis, which is in the ratio of 83:14:03 (%) for **3d/2d/2i**, respectively. ^1H NMR (**3d**, 400 MHz, CDCl_3): δ (ppm) = 1.58 (s, 6H), 2.08 (s, 1H), 6.99–7.03 (m, 2H), 7.44–7.48 (m, 2H); ^{13}C NMR (100 MHz, CDCl_3): δ (ppm) = 31.2, 65.9, 67.1, 73.1, 77.8, 86.8, 115.9, 116.1, 117.8, 117.8, 134.6, 134.7, 161.9, 164.4.

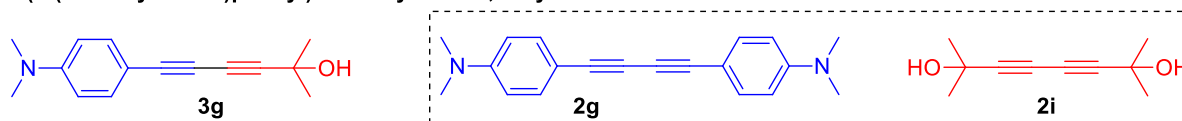
6-(4-chlorophenyl)-2-methylhexa-3,5-diyne-2-ol



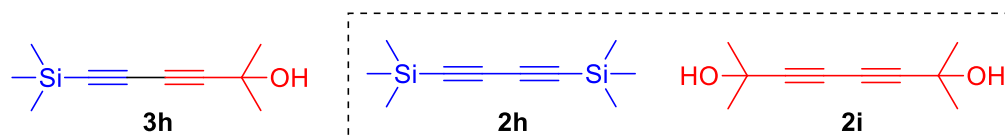
Following the above general procedure, when 0.2 mmol **1e** and 0.26 mmol **1i** were used, the crude product **3e** was purified by column chromatography on silica gel and eluted with ethyl acetate/hexane 1:8 to afford **3e** as a white solid in 73% isolated yield. The selectivity between the homo- and cross-Glaser-products was estimated based on the GC-MS analysis, which is in the ratio of 76:15:09 (%) for **3e/2e/2i**, respectively. ^1H NMR (**3e**, 400 MHz, CDCl_3): δ (ppm) = 1.58 (s, 6H), 2.01 (s, 1H), 7.30 (d, $J = 8.5$ Hz, 2H), 7.40 (d, $J = 8.5$ Hz, 2H); ^{13}C NMR (100 MHz, CDCl_3): δ (ppm) = 31.1, 65.9, 67.1, 74.2, 77.2, 87.4, 120.2, 129.0, 133.8, 135.6.

6-(4-bromophenyl)-2-methylhexa-3,5-diyne-2-ol

Following the above general procedure, when 0.2 mmol **1f** and 0.26 mmol **1i** were used, the crude product **3f** was purified by column chromatography on silica gel and eluted with ethyl acetate/hexane 1:8 to afford **3f** as a white solid in 75% isolated yield. The selectivity between the homo- and cross-Glaser-products was estimated based on the GC-MS analysis, which is in the ratio of 78:18:04 (%) for **3f/2f/2i**, respectively. ¹H NMR (**3f**, 400 MHz, CDCl₃): δ (ppm) = 1.56 (s, 6H), 2.05 (br. s, 1H), 7.33 (d, *J* = 8.8 Hz, 2H), 7.45 (d, *J* = 8.8 Hz, 2H); ¹³C NMR (100 MHz, CDCl₃): δ (ppm) = 31.2, 65.9, 67.0, 76.7, 77.8, 87.5, 120.7, 123.9, 131.9, 134.0.

6-(4-(dimethylamino)phenyl)-2-methylhexa-3,5-diyne-2-ol

Following the above general procedure, when 0.2 mmol **1g** and 0.26 mmol **1i** were used, the crude product **3g** was purified by column chromatography on silica gel and eluted with ethyl acetate/hexane 1:8 to afford **3g** as a yellow solid in 73% isolated yield. The selectivity between the homo- and cross-Glaser-products was estimated based on the GC-MS analysis, which is in the ratio of 84:12:04 (%) for **3g/2g/2i**, respectively. ¹H NMR (**3g**, 400 MHz, CDCl₃): δ (ppm) = 1.57 (s, 6H), 2.02 (s, 1H), 2.98 (s, 6H), 6.59 (d, *J* = 9.0 Hz, 2H), 7.35 (d, *J* = 8.9 Hz, 2H); ¹³C NMR (100 MHz, CDCl₃): δ (ppm) = 30.8, 40.1, 65.7, 67.6, 71.2, 80.6, 85.7, 108.0, 111.6, 133.8, 150.72.

2-methyl-6-(trimethylsilyl)hexa-3,5-diyne-2-ol

Following the above general procedure, when 0.2 mmol **1h** and 0.26 mmol **1i** were used, the crude product **3h** was purified by column chromatography on silica gel and eluted with ethyl acetate/hexane 1:8 to afford **3h** as a yellow solid in 65% isolated yield. The selectivity between the homo- and cross-Glaser-products was estimated based on the GC-MS analysis, which is in the ratio of 68:23:09 (%) for **3h/2h/2i**, respectively. ¹H NMR (**3h**, 400 MHz, CDCl₃): δ (ppm) = 0.20 (s, 9H), 1.53 (s, 6H), 1.96 (s, 1H); ¹³C NMR (100 MHz, CDCl₃): δ (ppm) = -0.3, 31.2, 65.7, 67.4, 82.1, 87.3, 88.0.

E3. ^1H - and ^{13}C -NMR, and GC-MS spectral profiles of cross-Glaser-products

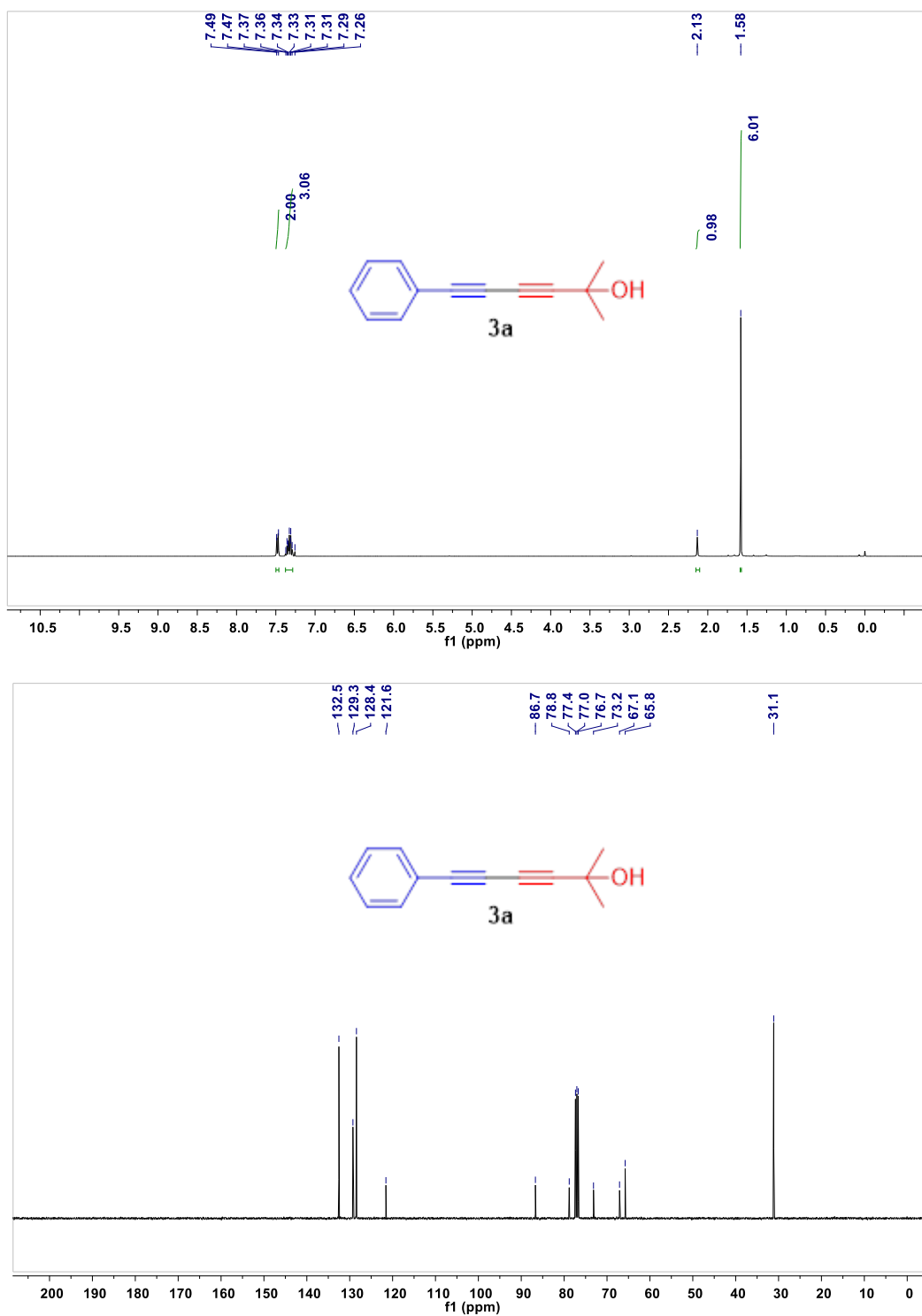
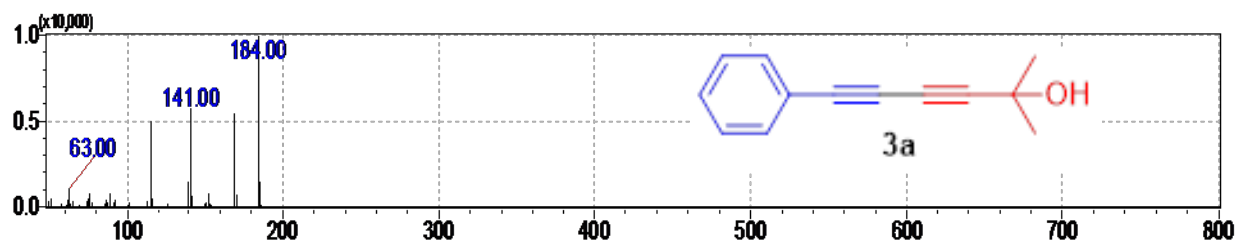
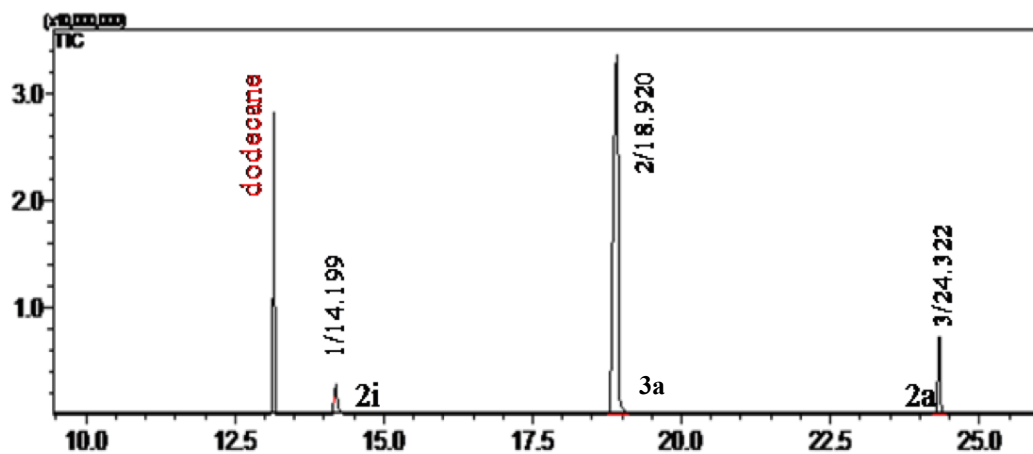


Fig. S32. ^1H - (400 MHz, CDCl_3 , 298 K) and ^{13}C -NMR (100 MHz, CDCl_3 , 298 K) spectra of **3a**.



GC Chart of crude reaction mixture (3a)



entry	Retention time	Area	Area %	Height	Height %	Mass (m/z)
1	14.199	11322792	4.96	5693305	11.91	166
2	18.920	194189622	85.15	34719949	72.66	184
3	24.322	22564754	9.89	7371301	15.43	202

Fig. S33. GC-MS profile of crude reaction mixture of 3a showing the selectivity of 85:10:05 (%) for 3a/2a/2i, respectively. Dodecane was used as a standard.

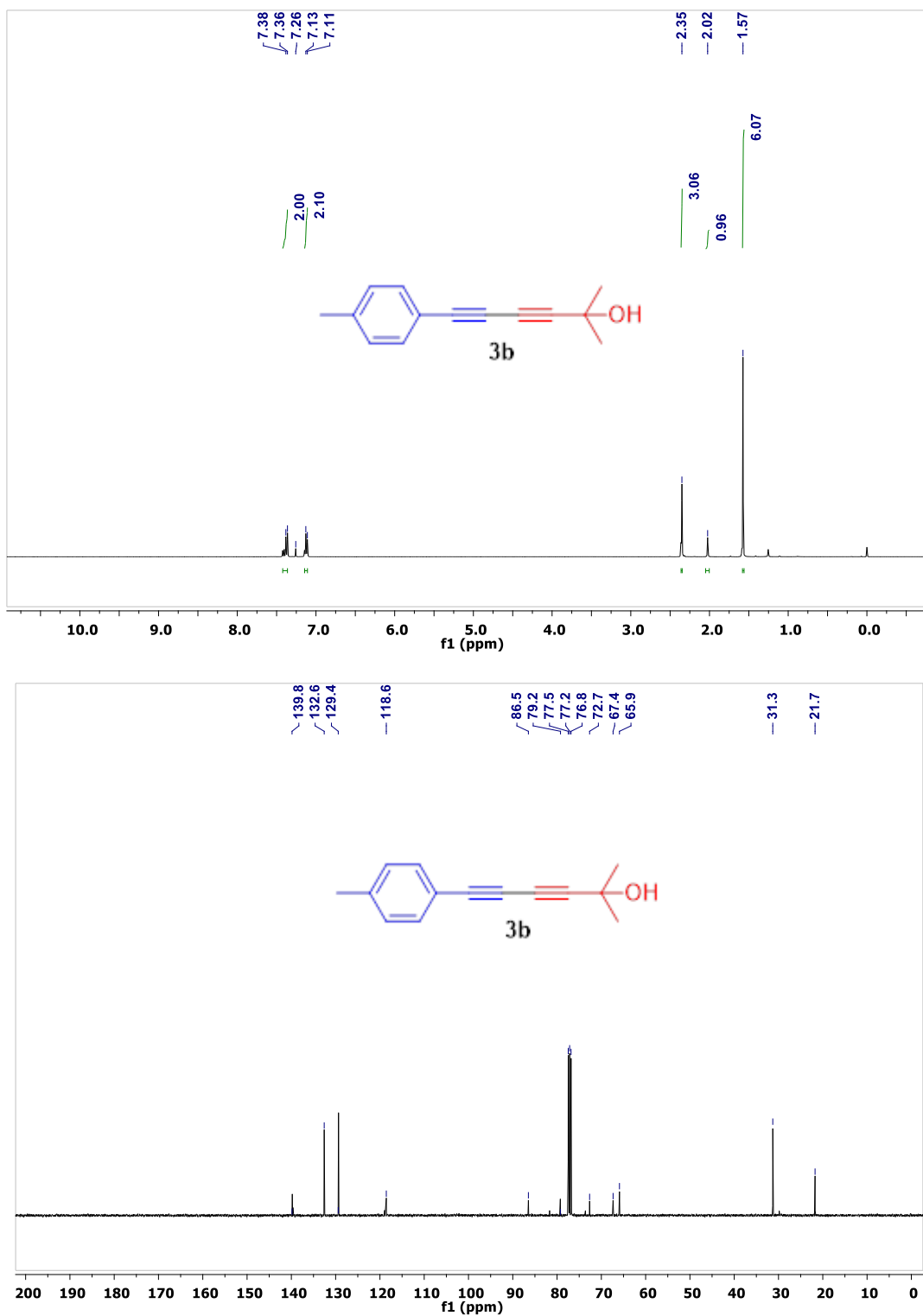
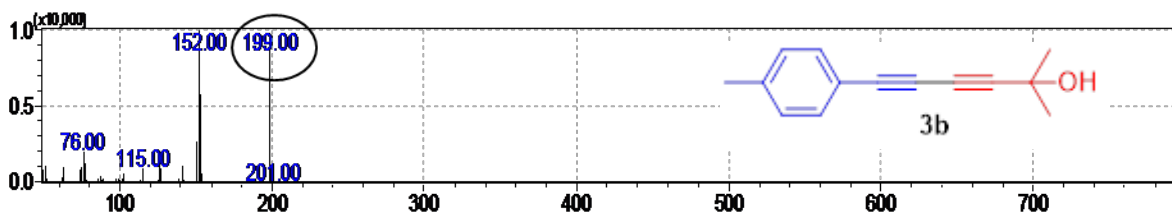
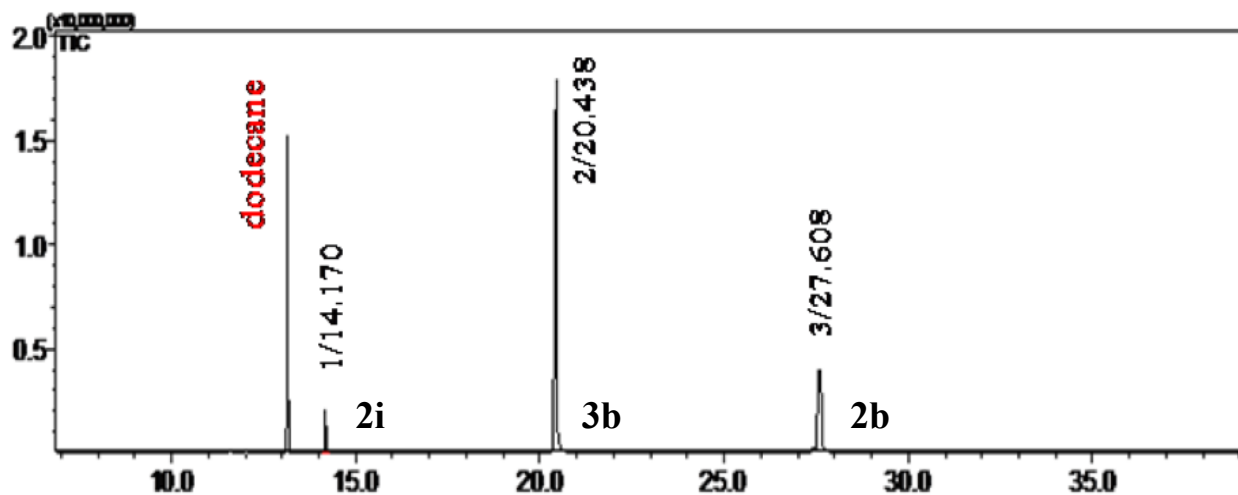


Fig. S34. ¹H- (400 MHz, CDCl₃, 298 K) and ¹³C-NMR (100 MHz, CDCl₃, 298 K) spectra of **3b**.



GC Chart of crude reaction mixture (3b)



entry	Retention time	Area	Area %	Height	Height %	Mass (m/z)
1	14.170	5137993	6.04	2288589	8.68	166
2	20.438	68989779	81.04	17748396	67.30	199
3	27.608	10998342	12.92	6333058	24.02	230

Fig. S35. GC-MS profile of crude reaction mixture of **3b** showing the selectivity of 81:13:06 (%) for **3b/2b/2i**, respectively. Dodecane was used as a standard.

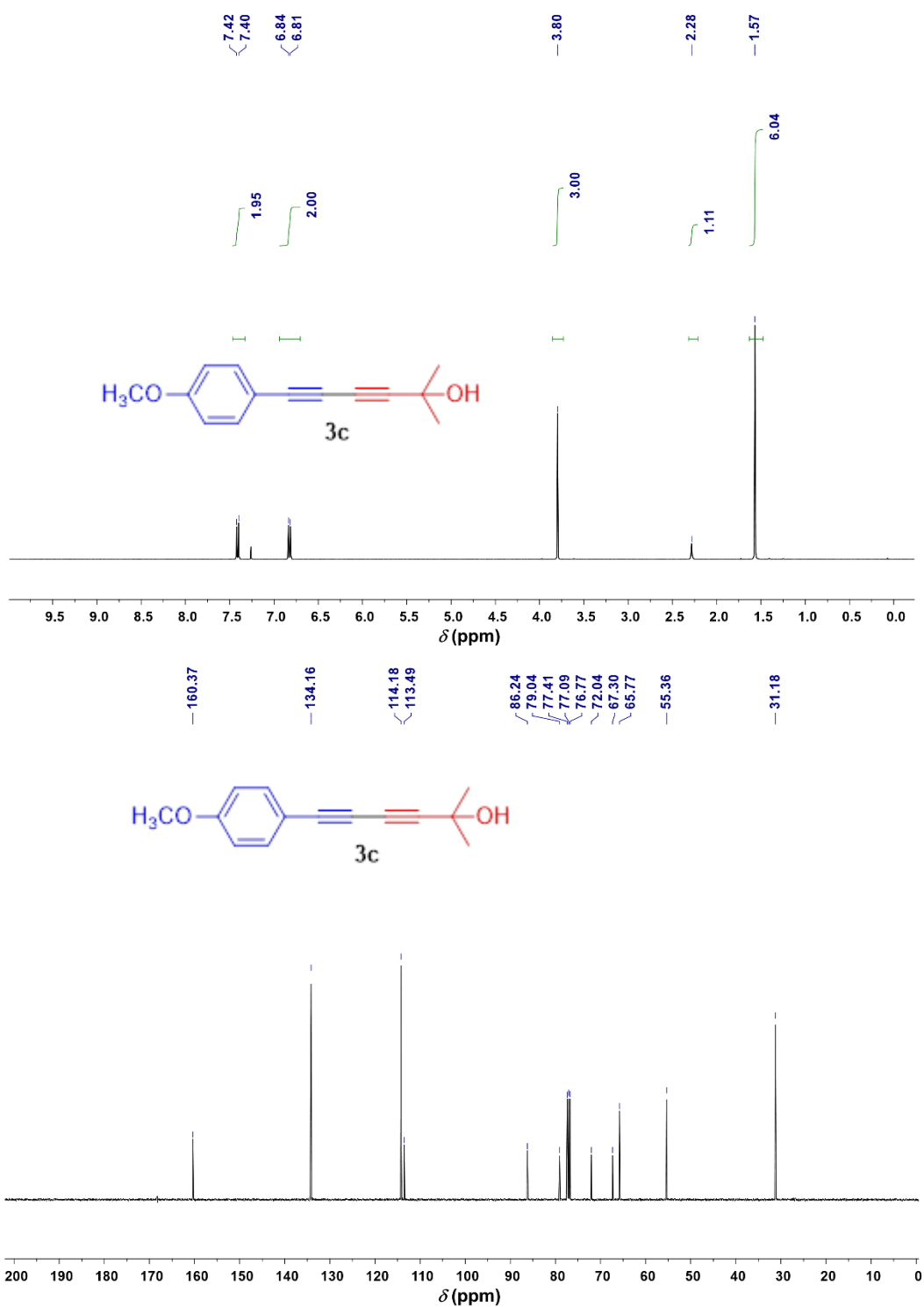
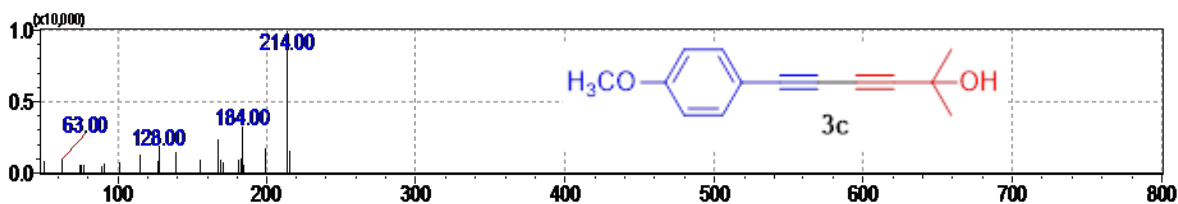
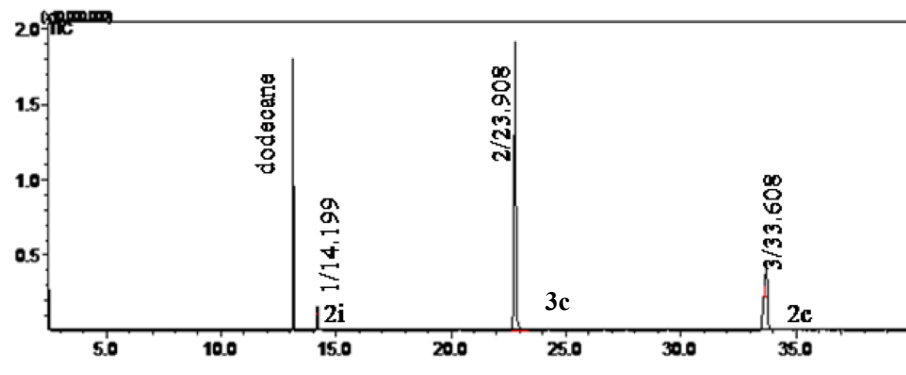


Fig. S36. ¹H- (400 MHz, CDCl₃, 298 K) and ¹³C-NMR (100 MHz, CDCl₃, 298 K) spectra of **3c**.



GC Chart of crude reaction mixture (3c)



entry	Retention time	Area	Area %	Height	Height %	Mass (m/z)
1	14.199	508188	7.77	506168	8.68	262
2	23.908	4754860	72.70	2873211	72.67	214
3	33.608	1277337	19.53	1622666	18.65	166

Fig. S37. GC-MS profile of crude reaction mixture of 3c showing the selectivity of 72:20:08 (%) for 3c/2c/2i, respectively. Dodecane was used as a standard.

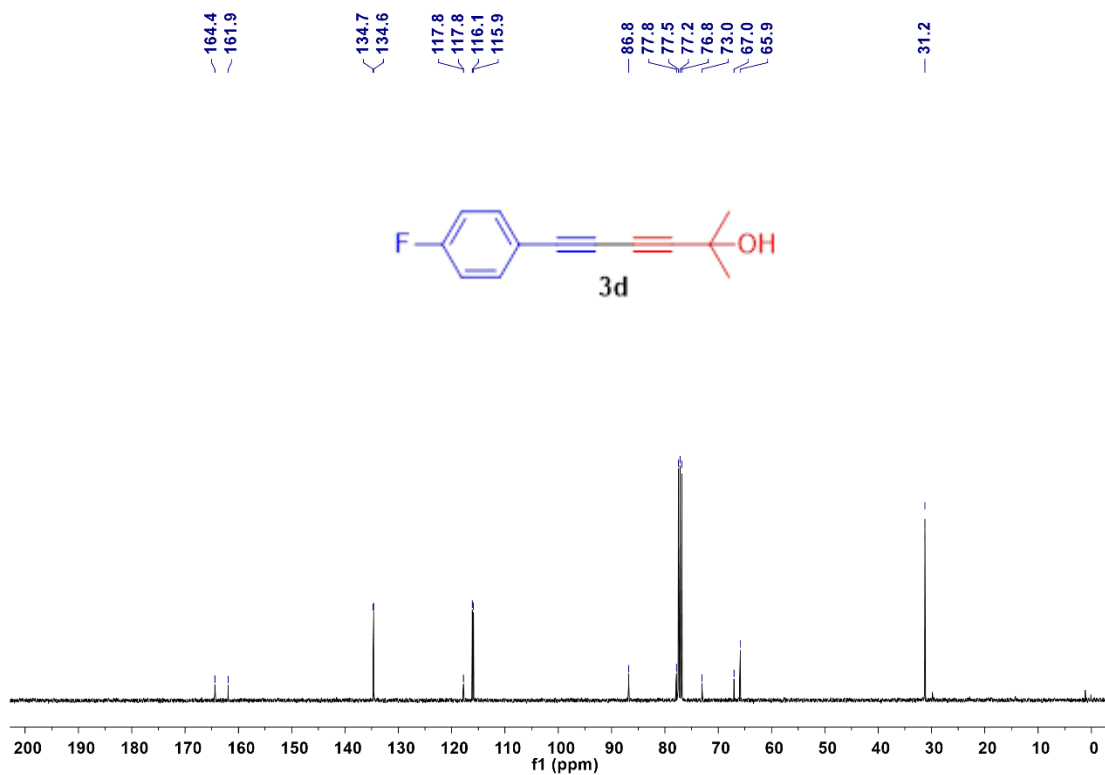
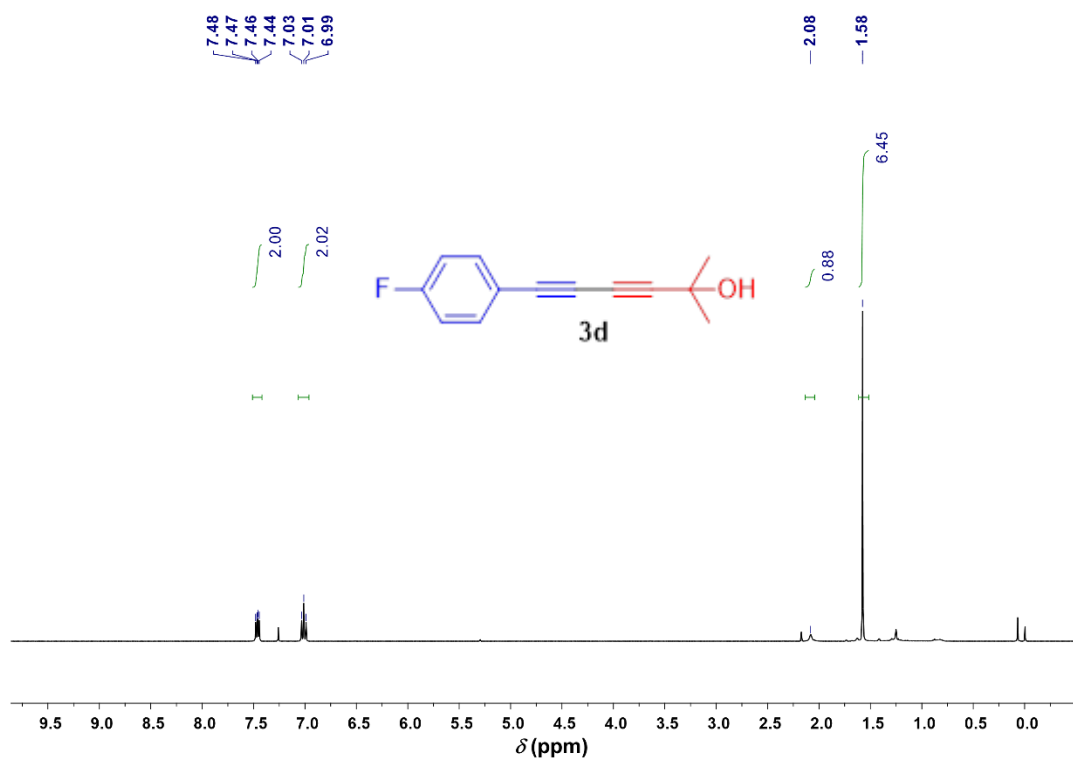
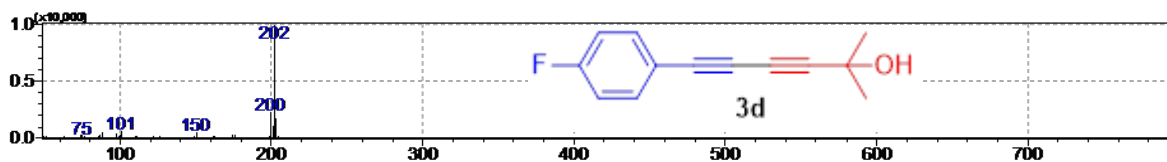
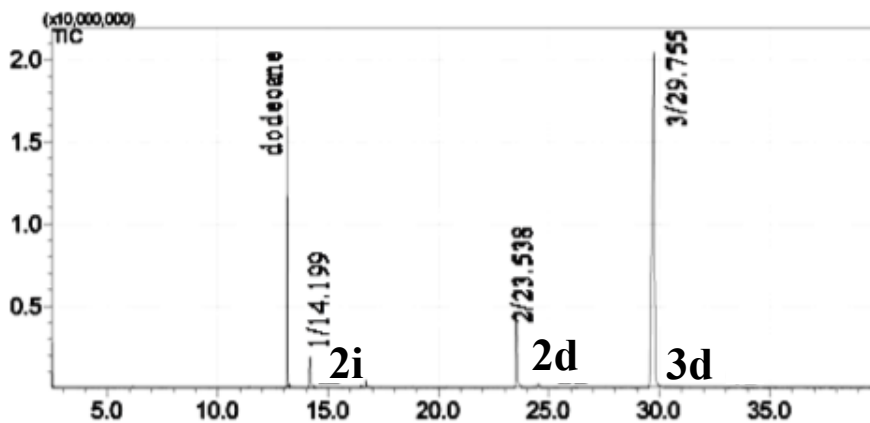


Fig. S38. ¹H- (400 MHz, CDCl₃, 298 K) and ¹³C-NMR (100 MHz, CDCl₃, 298 K) spectra of **3d**.



GC Chart of crude reaction mixture (3d)



entry	Retention time	Area	Area %	Height	Height %	Mass (m/z)
1	14.199	5732178	2.8	2487170	8.9	166
2	23.538	29500247	14.41	4789899	17.14	238
3	29.755	169488237	82.79	20459073	73.21	202

Fig. S39. GC-MS profile of crude reaction mixture of **3d** showing the selectivity of 83:14:05 (%) for **3d/2d/2i**, respectively. Dodecane was used as a standard.

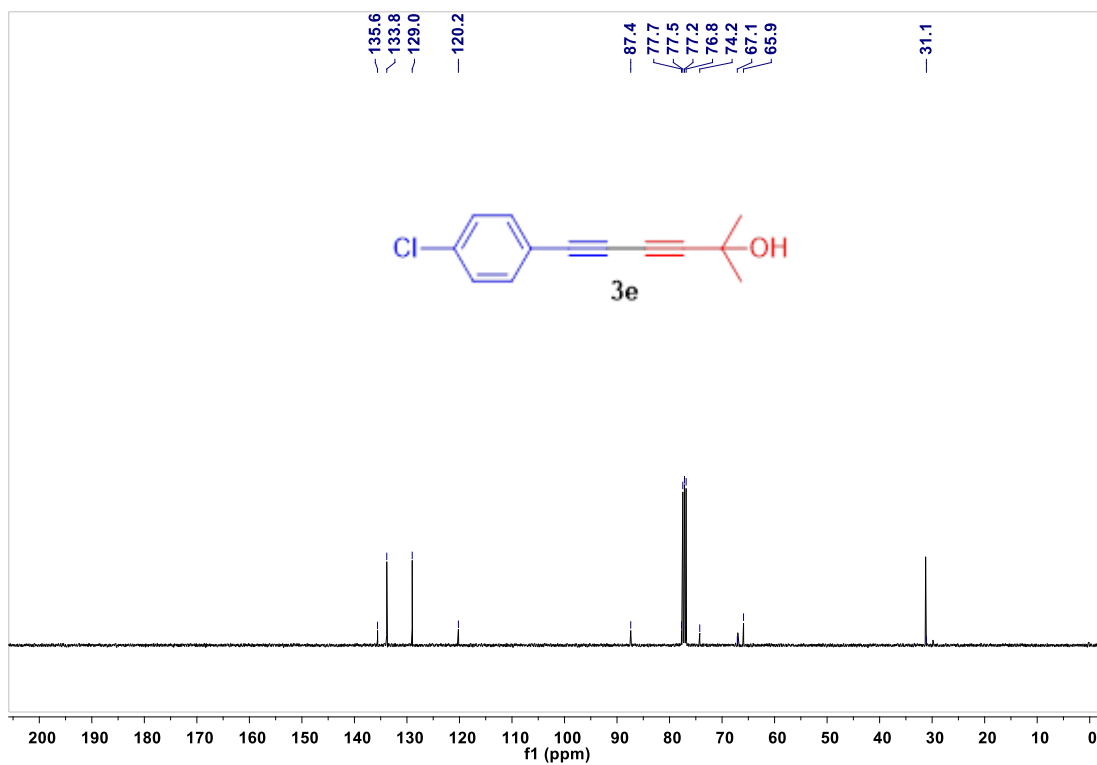
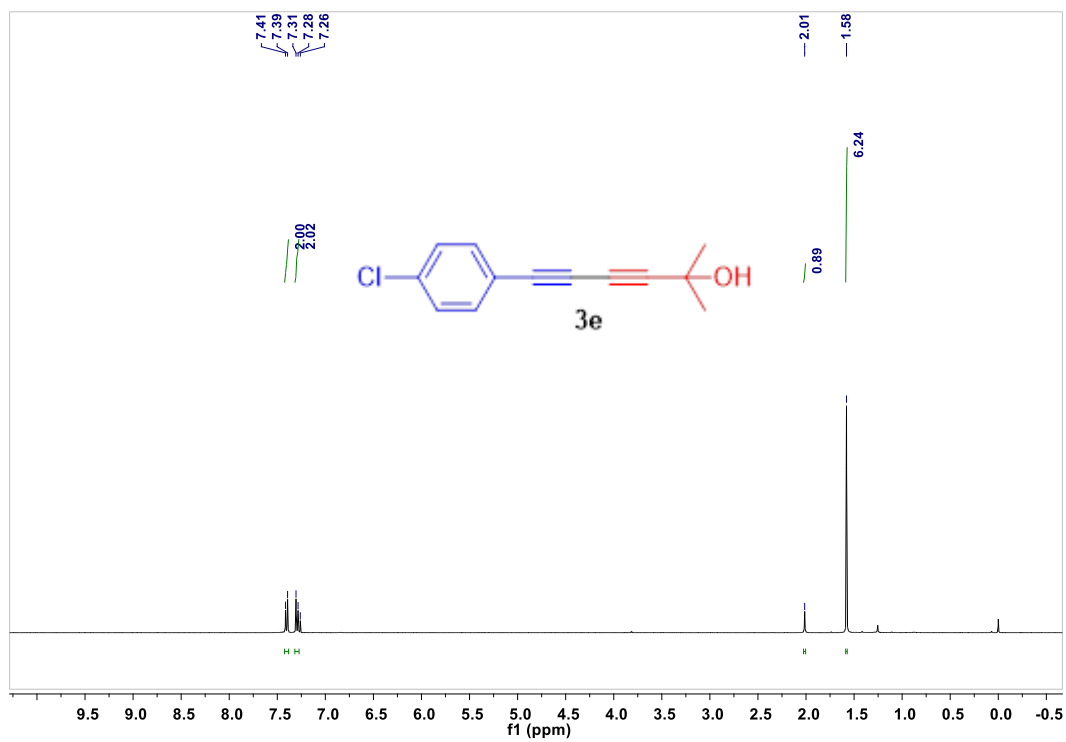
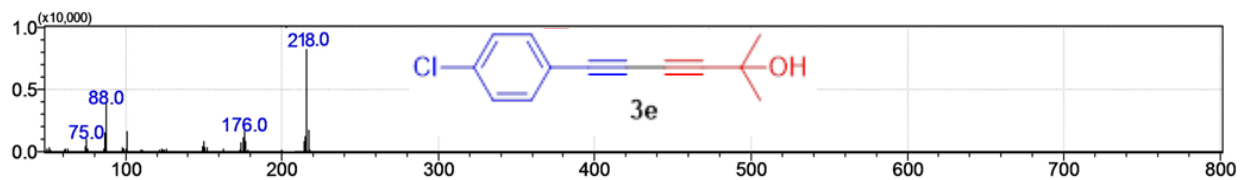
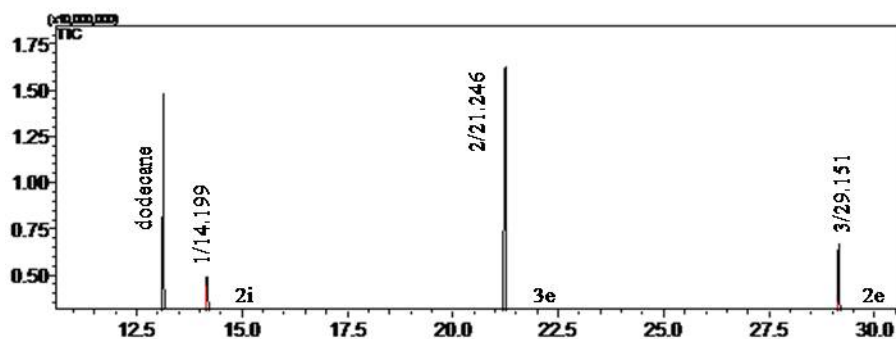


Fig. S40. ¹H- (400 MHz, CDCl₃, 298 K) and ¹³C-NMR (100 MHz, CDCl₃, 298 K) spectra of **3e**.



GC Chart of crude reaction mixture (3e)



entry	Retention time	Area	Area %	Height	Height %	Mass (m/z)
1	14.199	8651857	9.2	4692854	21.56	166
2	21.246	72177176	76.75	13312709	61.15	218
3	29.151	14294372	15.2	3763851	17.29	270

Fig. S41. GC-MS profile of crude reaction mixture of 3e showing the selectivity of 76:15:09 (%) for 3e/2e/2i, respectively. Dodecane was used as a standard.

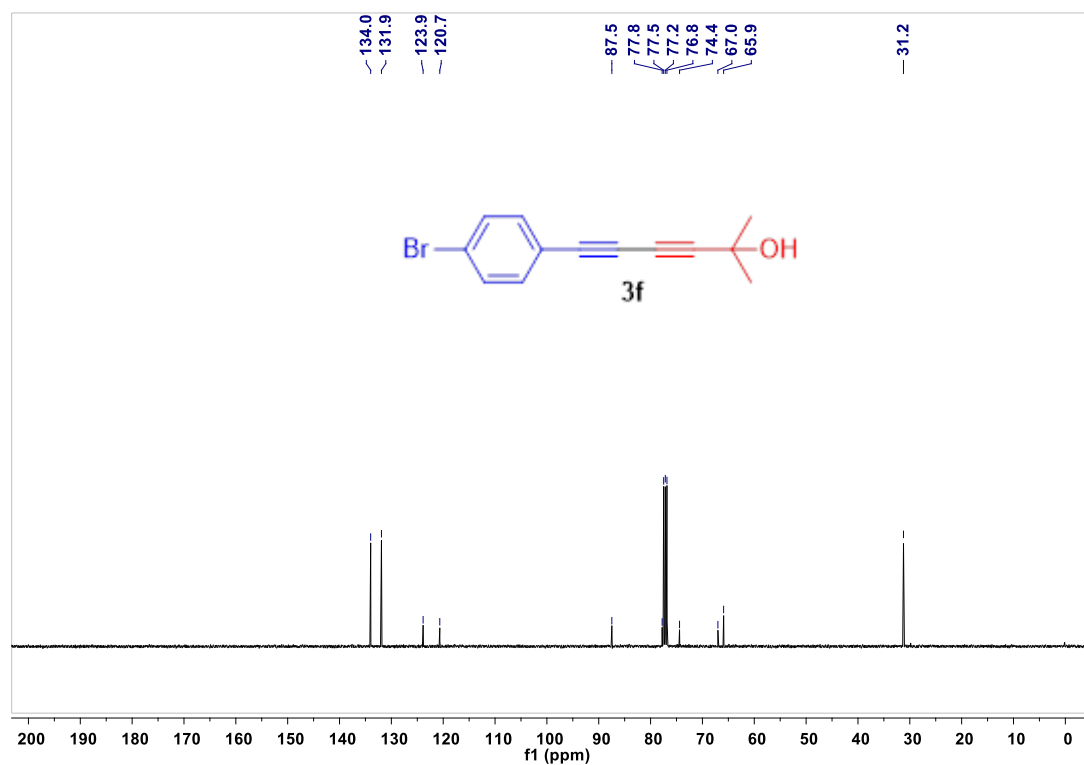
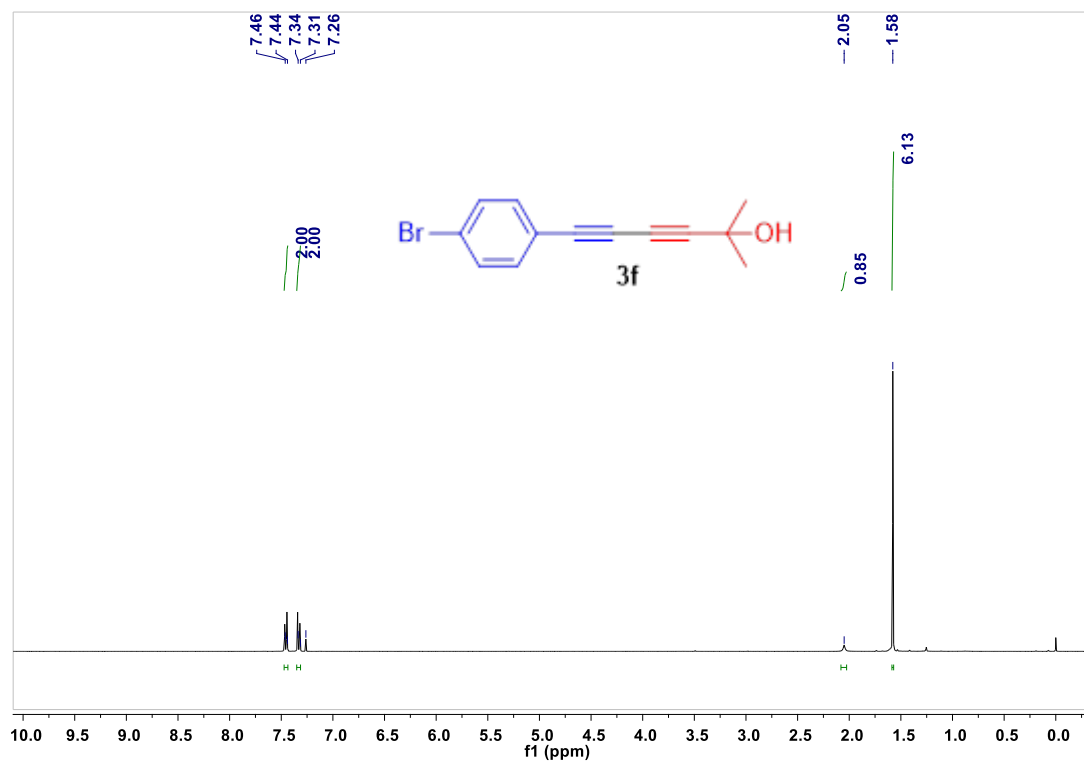
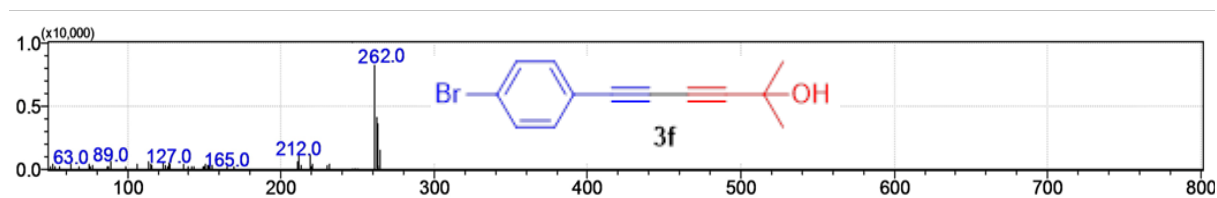
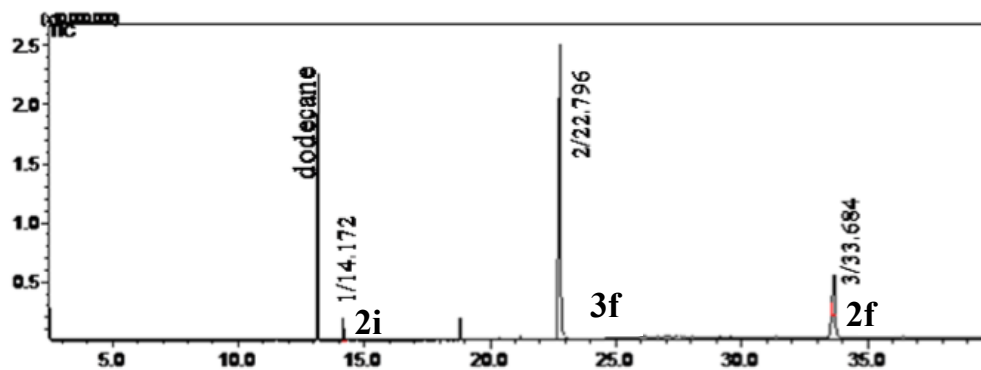


Fig. S42. ¹H- (400 MHz, CDCl₃, 298 K) and ¹³C-NMR (100 MHz, CDCl₃, 298 K) spectra of **3f**.



GC Chart of crude reaction mixture (**3f**)



entry	Retention time	Area	Area %	Height	Height %	Mass (m/z)
1	14.172	7057373	3.46	3030949	8.65	166
2	22.796	159753413	78.24	25020396	71.43	262
3	33.684	37371419	18.30	37371419	19.92	359

Fig. S43. GC-MS profile of crude reaction mixture of **3f** showing the selectivity of 78:18:04 (%) for **3f/2f/2i**, respectively. Dodecane was used as a standard.

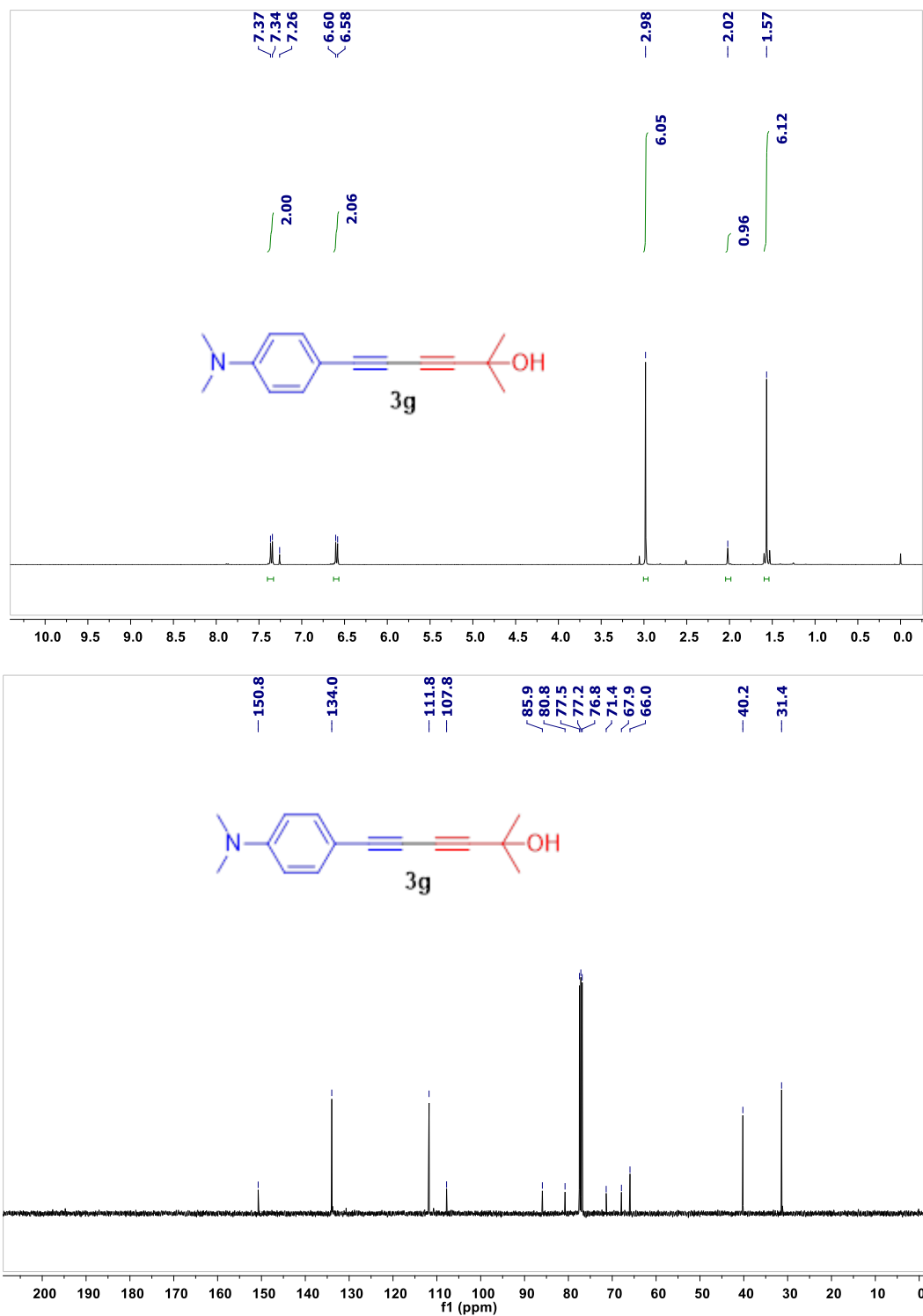
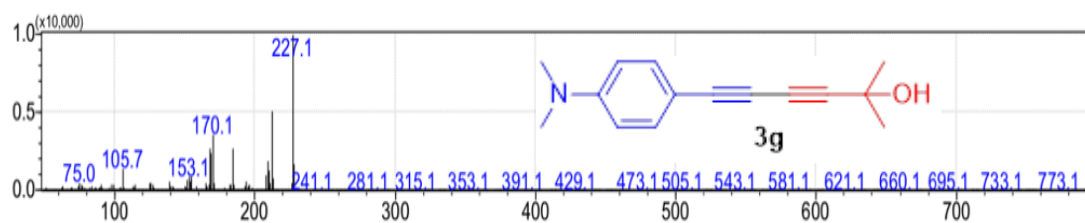
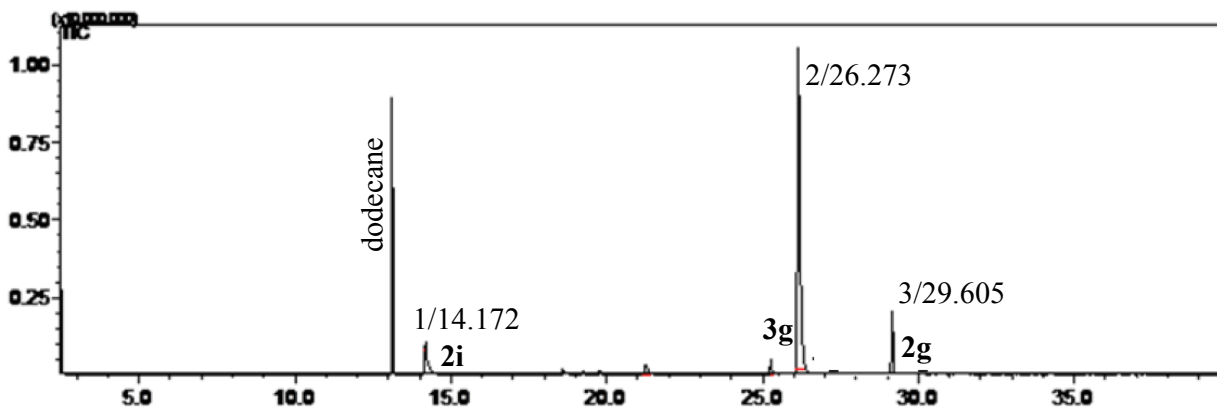


Fig. S44. ¹H NMR (400 MHz, CDCl₃, 298 K) and ¹³C NMR (100 MHz, CDCl₃, 298 K) spectra of **3g**.



GC Chart of crude reaction mixture (3g)



entry	Retention time	Area	Area %	Height	Height %	Mass (<i>m/z</i>)
1	14.172	9998542	3.47	586689	10.57	166
2	26.273	68869779	84.60	3706948	66.82	227
3	29.605	5075474	11.93	455078	22.4	288

Fig. S45. GC-MS profile of crude reaction mixture of **3g** showing the selectivity of 84:12:04 (%) for **3g/2g/2i**, respectively. Dodecane was used as a standard.

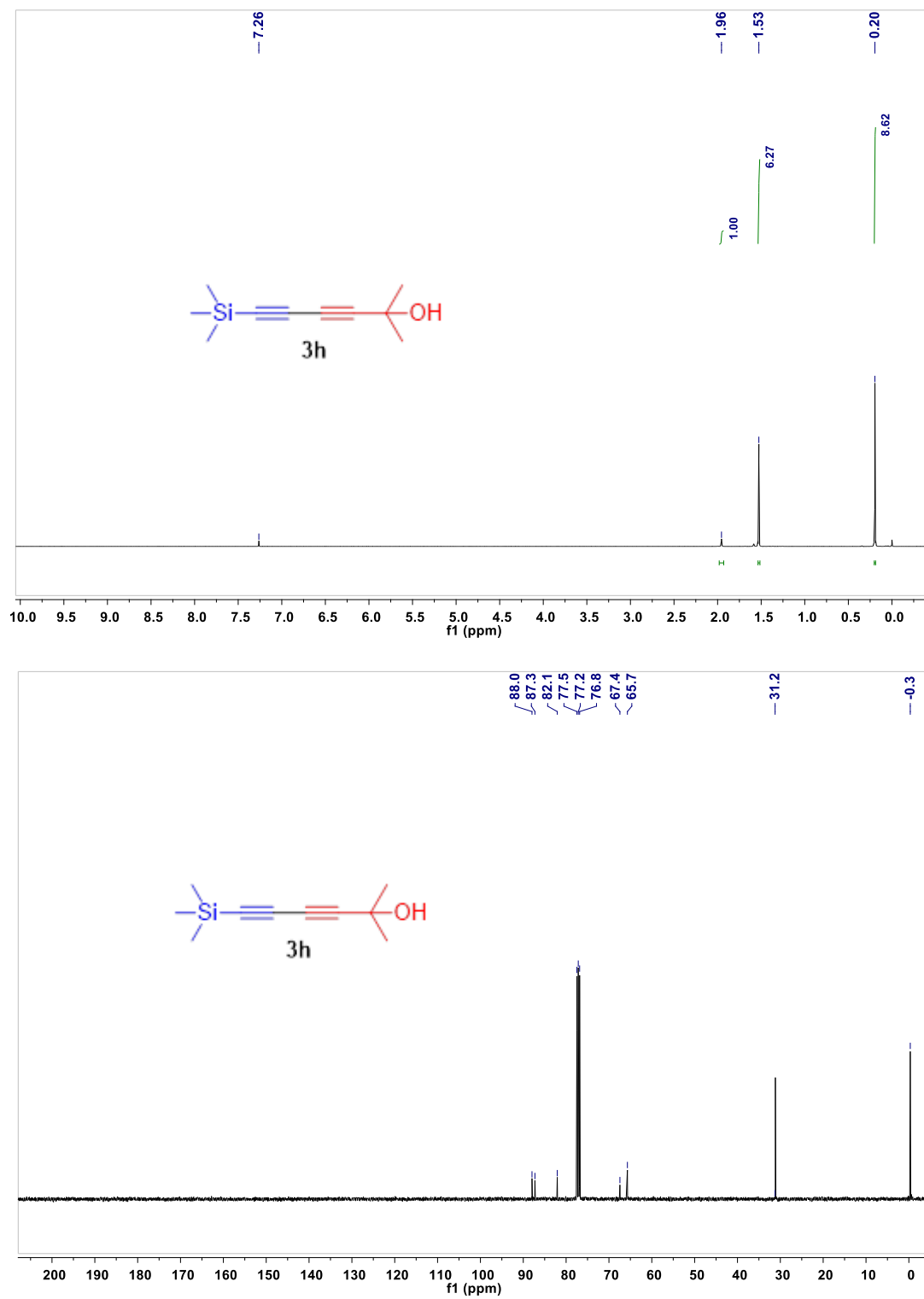
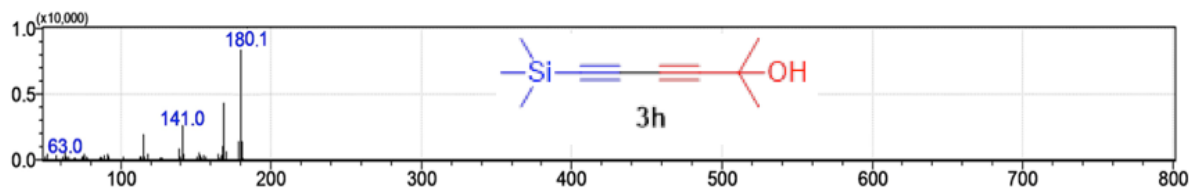
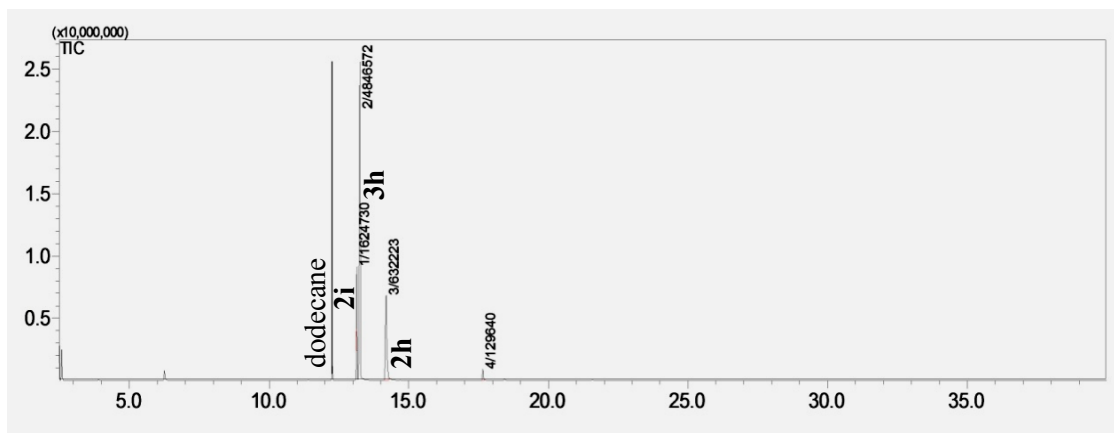


Fig. S46. ¹H- (400 MHz, CDCl₃, 298 K) and ¹³C-NMR (100 MHz, CDCl₃, 298 K) spectra of **3h**.



GC Chart of crude reaction mixture (3h)



entry	Retention time	Area	Area %	Height	Height %	Mass (m/z)
1	13.136	1624730	22.8	6728539	16.87	166
2	13.242	4846572	68.2	25443920	63.80	180
3	14.183	632223	0.09	6837905	17.15	194

Fig. S47. GC-MS profile of crude reaction mixture of 3h showing the selectivity of 68:23:09 (%) for 3h/2h/2i, respectively. Dodecane was used as a standard.

Section F: Computational method and modelling

F1. Polarity order of plausible intermediates

The Glaser reaction mechanism have been investigated extensively by both experimental & DFT calculations.¹⁶⁻²³ In homogeneous catalysis, it has been widely accepted that the formation of di-copper-dioxo $[\text{Cu}_2(\mu\text{-O}_2)]^{2+}$ core, in presence of TMEDA, are expected to form with terminal alkynes.^{16,17} In case of cross-coupling, three intermediates are expected to form corresponding to two homo-products and one cross-Glaser-product (Fig. S48b). They clearly exhibit different polarity order as shown below.

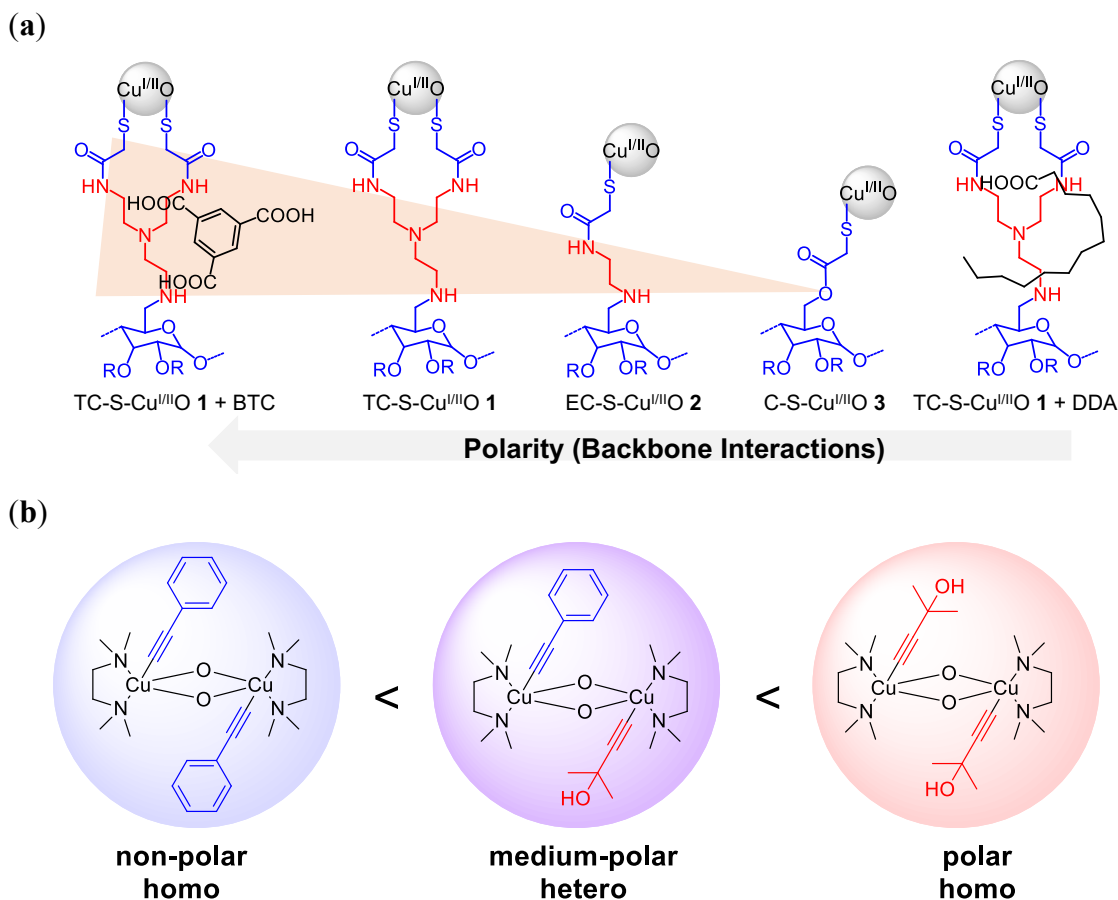


Fig. S48. (a) Structure of catalysts with varying amine part on the copper oxide ($\text{Cu}^{\text{II}}\text{O}$) nanoparticles backbone. The abbreviation BTC stands for benzene-1,3,5-tricarboxylic acid and DDA stands for dodecanoic acid. (b) Structures of plausible intermediates^{16,17} for the corresponding homo- and cross-Glaser-products showing the polarity order in homogenous catalysis.

F2. Computational details

The unit cell of CuO was optimised using density functional theory (DFT)^{24,25} with Perdew-Burke-Ernzerhof (PBE)²⁶ exchange correlation²⁷ functional implemented in VASP^{28,29}. The same functional was used for the ab initio Born-Oppenheimer molecular dynamics (BOMD) simulations as well. The unit-cell has the monoclinic symmetry (space group P2/c). The optimised unit cell parameters are as follows a=4.67 (4.65, 0.32%), b=3.398 (3.41, 0.73%), c=5.19425 (5.11, 1.27%), β =97.1724 (99.48;2.34%). The values in the parenthesis represents the experimental values²² of the cell parameters along with percentage deviation from experimental results. The plane wave cut-off was set to 400 eV for optimisation. The convergence tolerance for the self-consistent electronic minimisation was set to 10^{-5} eV/cycle.

F3. Modelling of the catalyst Cu(II)O nanoparticle assembly

The (111) surface of CuO was chosen as the catalyst-nanoparticle interface, as it has the lowest surface energy²³ among the different CuO surfaces. A supercell of size 17.32x 22.21x35.0 Å³ with 4x4x3 repetitions along x, y, z directions, respectively was chosen for modeling the CuO surface slab. The large value of c represent a vacuum added to that direction. The positions of the atoms inside the surface supercell was also optimised using the same computational methods described for optimisation of the unit cell. For the modelling of the catalyst tris-(2-aminoethyl) amine (TREN)-cellulose (TC) functionalised with thioglycolic acid (S) was used (Fig. S49). An optimised catalyst unit with its sulphur atoms anchored on two Cu atoms on the CuO surface super cell were used as the heterogeneous catalyst. The relaxation of the catalyst on the top of the surface along with the relaxation of the surface CuO layers were performed to get a relaxed CuO catalyst assembly. Among the three CuO layers the upper two layers were considered as the surface while the lowest layer were fixed to its bulk position. To understand the coupling reactions on the surface, we used the alkynyl anions, anchored on the CuO surface by means of sigma complex formation (Fig. 2a in the Main Text).

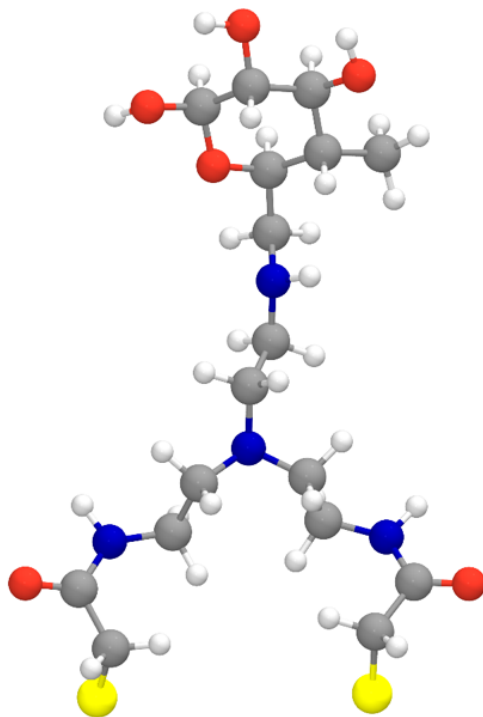


Fig. S49. The ball stick model of the optimised catalyst **1** in the gas phase.

F4. Ab initio molecular dynamics

The ab initio molecular dynamics (AIMD)^{30,31} simulations were performed using canonical ensemble and at 300 K. The Nose-Hover thermostat was used to control temperature of the simulated box. The van der Waals interactions were accounted through the DFT-D2 dispersion correction as devised by Grimme et al.³² The plane wave cut-off was set to 300 eV and the convergence tolerance for the self-consistent electronic energy minimisation was set to 10^{-4} eV/cycle for the molecular dynamics run. The 1 fs time steps was set for all simulations.

The dynamics were performed for all the three possibilities of the coupling reaction; i.e. two homo-coupling and the cross-coupling reaction between the two terminal alkyne reactant. The alkynes were anchored on the surface by means of sigma-complex formation as discussed in the previous mechanistic study. Total 2 ps trajectories was generated for each product formation to ensure the exploration of all kind of interactions might be present during the course of the reaction. The temperature fluctuation during the dynamics is shown in Fig. S50 indicating the thermal equilibrations of the system.

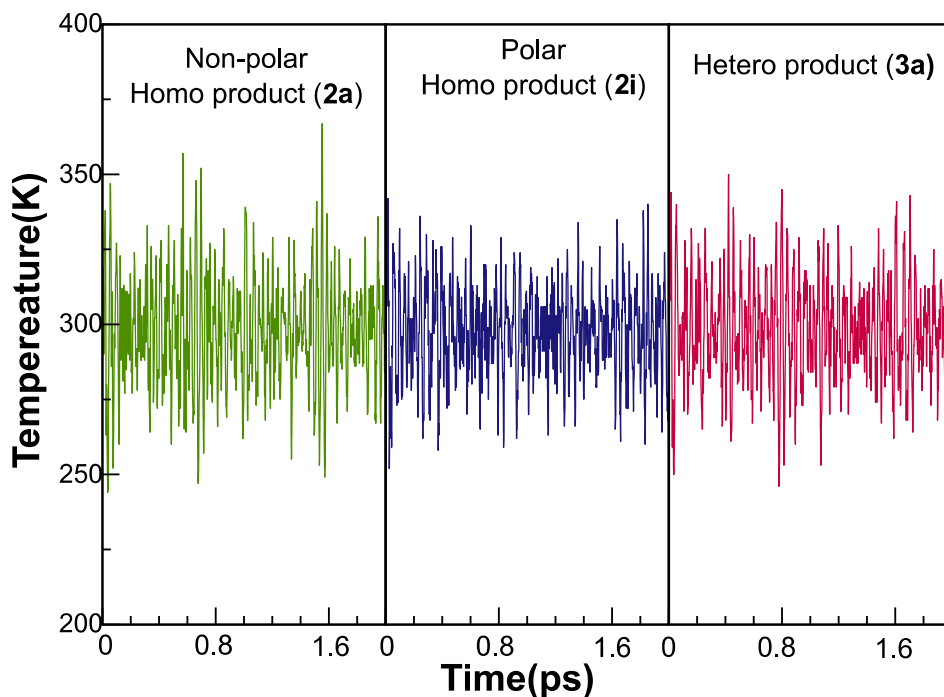


Fig. S50. Temperature fluctuation in the model reaction systems during the product formation obtained from the simulation of 2ps trajectory. The average temperature is 300 K .

Fig. S51 represents the distribution of C—C distance along different time windows throughout the trajectory. The wider distribution at the beginning of the trajectory implies that the formation of C—C bond occurs at this time window. At the later stages, the distributions are sharper and hence one can conclude a successful coupling reaction.

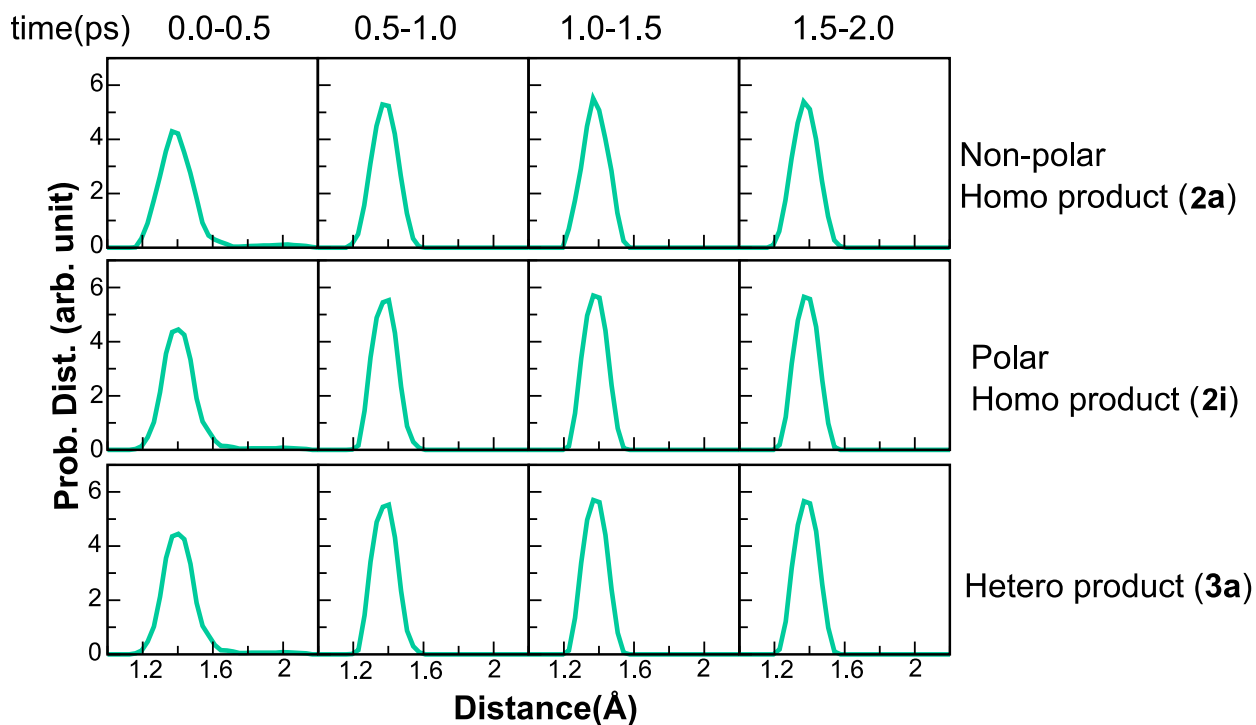


Fig. S51. Probability distribution of newly formed C—C bond distance at different time windows of total simulation.

On the other hand, Fig. S52 describes the variation of possible H-bonding distances during the formation of polar homo-product (**1i**) and cross-Glaser-product (**3a**) devied into time windows. This captures the H-bond formation and it's relative stability over the time windows. Although it seems that there is a H-bonding interaction for polar homo (**1i**) at 2nd time window but in reality this behaviour is attributed to residence of the polar groups in the vicinity of the catalyst. But as the time propagates it gets weaker and even doesn't show any sign of H-bond formation at the last window of the simulation. While, for the cross-Glaser-product the H-bonding distance gets lowes as the time progresses implying the formation of a strong H-bond.

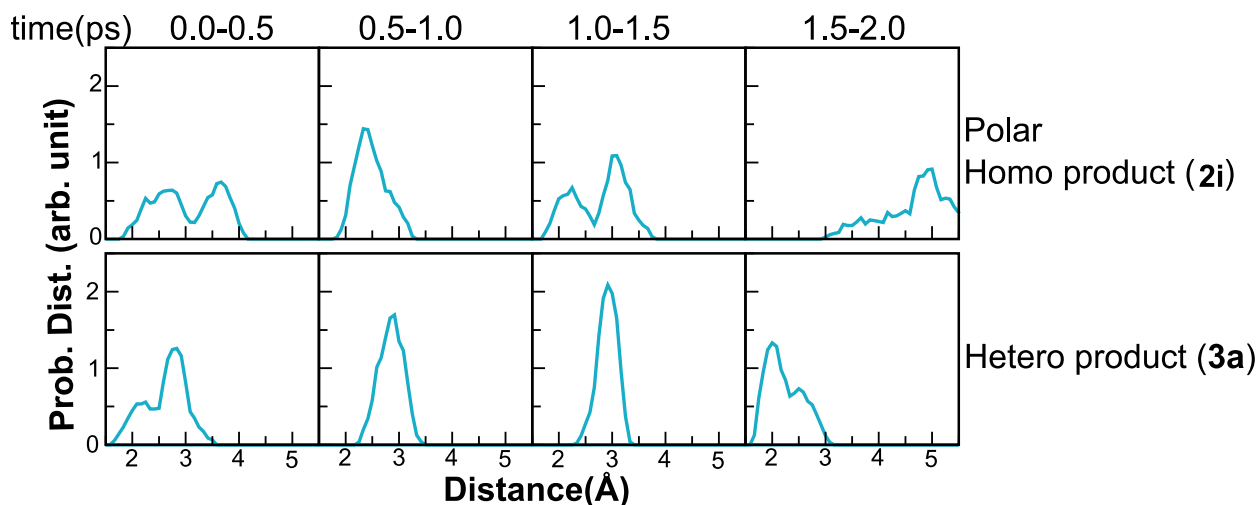


Fig. S52. Probability distribution of the H-bonding distances for two possible cases at different time windows.

The main aim of this part of the study was to evaluate the role of the catalyst towards controlling the hetero-selectivity. The complete energetics of these kind of heterogeneous reactions along with proper demonstration of reaction pathways are much more complex and still not explored properly. The experimental investigations performed by Bohlmann et al.³³ and later by Fedenok et al.^{34,35} postulated that the π -complex formation between the Cu and alkyne activates the alkyne for deprotonation. After deprotonation the copper (I)- σ -acetylide is formed which then undergoes coupling reaction. As we are only interested in exploring the role of interactions between catalyst and reactants, we took the initial geometry of copper (I)- σ -acetylide as a bent one, described to be an intermediate in previous computational investigations. This gives us the atomistic details of involved chemical processes during the product formation. In the following section we are going to discuss about the electronic structure changes during the progress of the reaction.

F5. Evolution of the Electronic Structures During the Coupling Reaction as Captured from Density of States (DOS) in DFT Calculations

To understand the evolution of the electronic structures during the course of the coupling reaction, the spin polarised ml-resolved DOS for Cu atom and the alkynyl C atom are compared (See Fig. S53). The spin polarised p-DOS of the terminal acetylide C-atoms to understand associated orbitals

in the sigma-bond formation as well as the evolution of the re-hybridization process for the chemical bond formation. The d_z^2 orbital of Cu-atom plays the crucial role in the formation of the initial copper (I/II)- σ -acetylide complex as it involved in the chemical bonding with the substrate in the activated (initial) state through the d_z^2 - p_z (C-atom) overlap.

It can be observed in the DOS plots (see Fig. S53) that at the initial stages the p_z orbitals of C atoms hybridizes with s orbital and overlaps with the d_z^2 orbital of the Cu-atom. As time propagates the C-atoms re-hybridize from sp_z to sp_y (i.e the sigma bonding axis changes from z axis to y axis) and overlap with each other via sigma bond formation. The intermediate formed at this process is a Cu(II) species. The formation of Cu(I) at the product stage indicates successful reductive elimination reaction. The product is formed via sigma bond formation between two sp_y orbitals of two C atoms.

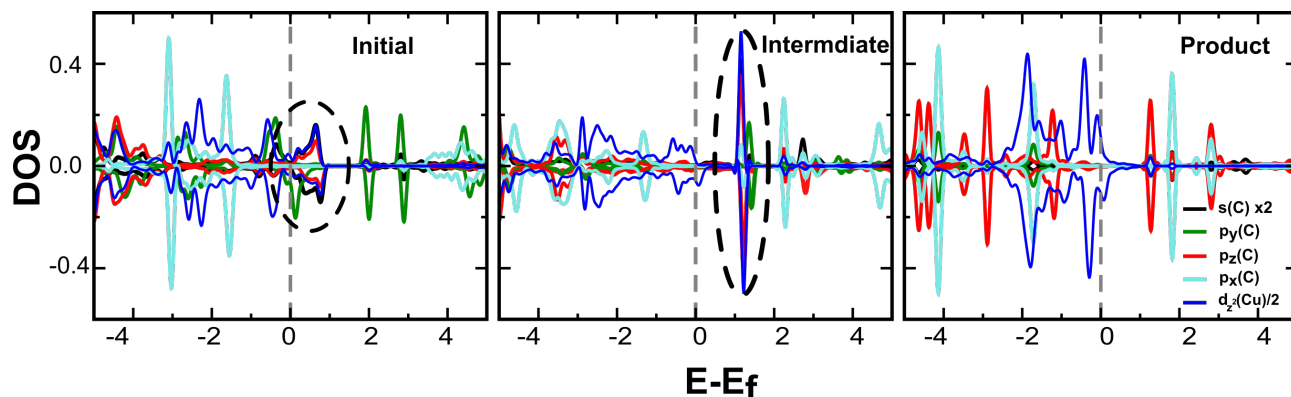


Fig. S53. The changes in the electronic structure at different stages. Initially, the s and p_z orbitals of the C atom is hybridised and exhibits bonding with the d_z^2 orbital of Cu atom (circled portion). The electronic states of intermediate exhibits a sharp peak at the unoccupied level which represents Cu(II). Absence of any state corresponding to Cu- d_z^2 orbital at unoccupied in the DOS-plot after product formation infers successful occurrence of reductive elimination reaction from Cu(II) to Cu(I). After the successful reductive elimination reaction, hybridization at the C atom changes to sp_y . σ -bond formation between C atom leads to coupling reaction.

Section G. Magnetically Recyclable catalyst

G1. Recyclability study using MNP-TC-S-Cu^{III}O 4

To make it a reusable catalyst, TC-S-Cu^{III}O **1** was grafted over the surface of super magnetic Fe₃O₄ nanoparticles² (MNP) to provide MNP-TC-S-Cu^{III}O **4** (Fig. S54a and Scheme S5B). The synthesis and characterisation of as-prepared MNP-TC-S-Cu^{III}O **4** is provided in the sections G2 and G3, respectively.

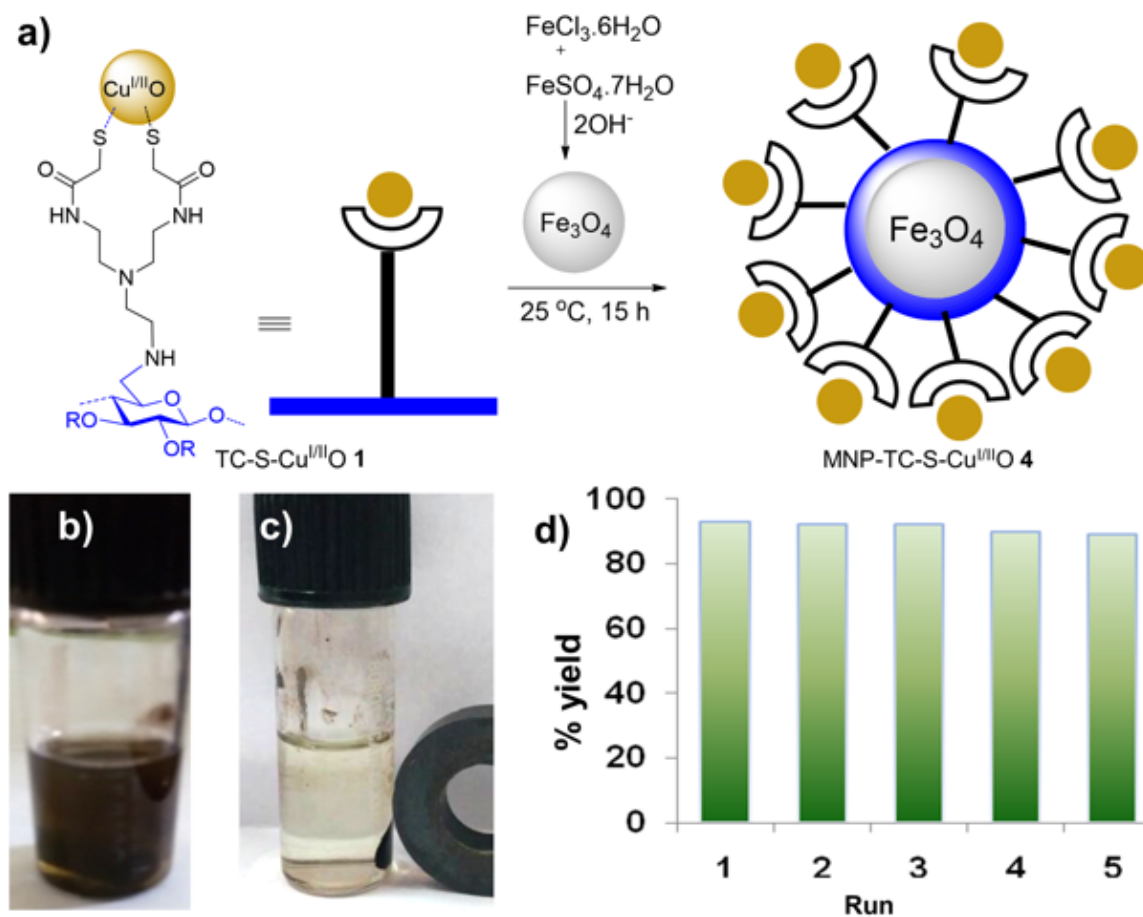


Fig. S54. (a) Schematic representation of grafting of TC-S-Cu^{III}O **1** over the surface of Fe₃O₄ NP to form MNP-TC-S-Cu^{III}O **4**. (b) Catalyst **4** dispersed in the reaction mixture of **1a**. (c) An external magnet attracted catalyst **4**. (d) Isolated yields of diyne **2a** obtained from **1a** by using heterogeneous catalyst **4**.

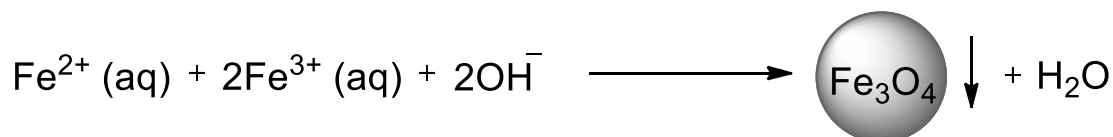
The homo-coupling of **1a** was investigated to demonstrate the magnetic recyclability of catalyst **4** under the conditions mentioned in entry 1, Table 2. Catalyst **4** could be easily separated out from the reaction mixture by external magnet after each cycle (Figs. S54b and S54c), and washed with

ethanol, dried, and weighed for the subsequent run. Interestingly, catalyst **4** could be recycled for 5 consecutive times without significant loss of its activity (Fig. S54d). The separation and reuse of the MNP-TC-S-Cu^{I/II}O **4** were very simple, effective and economical. Further, the TEM image of the catalyst **4** after 5 runs did not show any significant change in the morphology (Fig. S59). The EDX spectrum after 5 runs showed the presence of Cu and Fe, in the MNP-TC-S-Cu^{I/II}O **4** (Fig. S60). These results indicate that the catalyst **4** is stable during the catalytic process. Thus, the as-prepared backbone modified Cu-catalyst **4** serve as an efficient, fast, and reusable catalytic system for carrying out homo- and cross-coupling of terminal alkynes under environmentally benign conditions.

G2. Synthesis of MNP-TC-S-Cu^{I/II}O (catalyst **4**)

It involves two steps (Schemes S5A and S5B): (i) Synthesis of magnetite (Fe₃O₄) nanoparticles (MNP), (ii) Coating of TC-S-Cu^{I/II}O **1** over the MNP to afford MNP-TC-S-Cu^{I/II}O **4**.^{2a}

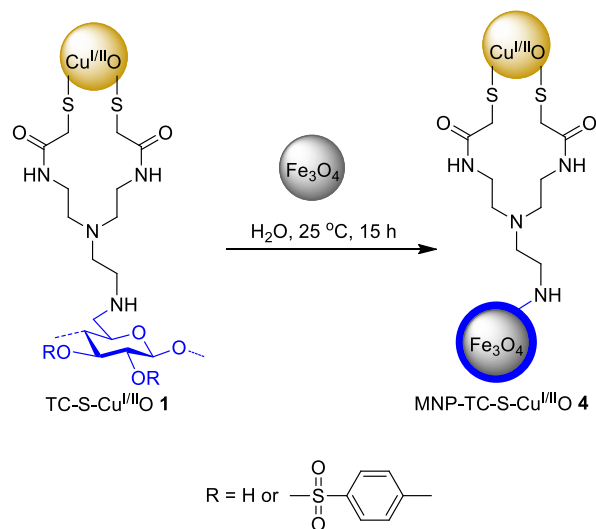
(i) Synthesis of magnetite (Fe₃O₄) nanoparticles (MNP).² Cellulose and TC grafted with magnetite nanoparticles (NP) were shown to be heterogeneous and magnetically separable.^{2,36,37} Magnetite nanoparticles (Fe₃O₄ NP) were prepared by co-precipitation (Scheme S5A) of ferric chloride (FeCl₃.6H₂O) and ferrous chloride (FeCl₂.4H₂O) salts under nitrogen (N₂) environment in a 2:1 molar ratio.² FeCl₃.6H₂O (1.35 g, 5 mmol) and FeCl₂.4H₂O (0.5 g, 2.5 mmol) were dissolved into 50 mL of degassed double distilled water and stirred for 30 min. Chemical precipitation was achieved at 25 °C under stirring (500 rpm) by adding 50 mL of 2M NaOH solution in the N₂ atmosphere. Then stirring was continued further for 3 h at 70 °C. The reaction was cooled to 25 °C and the particles were separated by using an external magnet, washed with double distilled water (3 × 100 mL) and vacuum dried at 50–60 °C for 15 h.



Scheme S5A. Synthesis of magnetite nanoparticles (MNP).

(ii) Grafting of TC-S-Cu^{I/II}O on magnetite nanoparticles (MNP) to give MNP-TC-S-Cu^{I/II}O (catalyst **4).**² MNP-TC-S-Cu^{I/II}O (catalyst **4**) was synthesized by adding 2 wt% aqueous solution of catalyst **1** (0.2 g, 10 mL) to 1 wt% aqueous solution of freshly synthesized Fe₃O₄ NP (0.1 g, 10 mL) as shown in Scheme S5B. The resulting mixture was stirred at 25 °C for 15

h. The heterogeneous reaction mixture was collected by using the external magnet after washing with double distilled water (3×100 mL) and vacuum dried at 50 °C for 15 h.



Scheme S5B. Synthesis of MNP-TC-S-Cu^{II}O **4**.

G3. Characterisation of MNP-TC-S-Cu^{II}O **4**

Characterisation of MNP-TC-S-Cu^{II}O **4** synthesized in Scheme S5B, Section G2 was investigated by FT-IR, PXRD, SEM-EDX, TEM, and ICP-MS analyses. The details are discussed below.

FT-IR (MNP-TC-S-Cu^{II}O, KBr): $\tilde{\nu} = 3454$ (O–H stretching, s), 2908 (C–H symmetrical stretching, m), 1725 (C=O, S), 1652 (m), 1620 (m), 1202 (s), 1165 (s), 1046 (w), 996 (m), 663 (m), 603, 586 (Fe–O, w), 520 cm^{-1} (w). The presence of bands at 663, 603, and 584 cm^{-1} are due to the presence of CuO/Cu₂O in the FT-IR spectrum (Fig. S55) of catalyst **4** indicate different modes of bending/stretching vibration of the Cu–O bond of copper oxide NP.^{11,12} In addition, the peak at 586 cm^{-1} also corresponding to the Fe–O band of magnetite (Fe₃O₄).

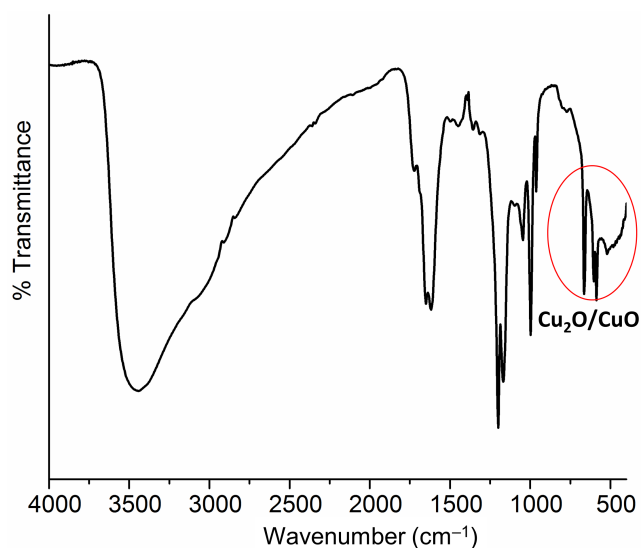


Fig. S55. FT-IR spectrum of as-prepared MNP-TC-S-Cu^{I/II}O 4.

PXRD data of MNP-TC-S-Cu^{I/II}O 4: Fig. S56 shows the PXRD spectrum of MNP-TC-S-Cu^{I/II}O 4. Diffraction peaks at 31.0°, 35.3°, 42.8°, 53.3°, 56.8° and 62.6° correspond to (220), (311), (400), (422), (511), and (440) planes of cubic inverse spinel Fe₃O₄ (JCPDS 03–0863), respectively.³⁸ However, other peaks indicate the existence of monoclinic CuO phase and cubic fcc structure of Cu₂O.³⁹ The result of XRD spectrum indicates that MNP-TC-S-Cu^{I/II}O 4 has been successfully synthesised.

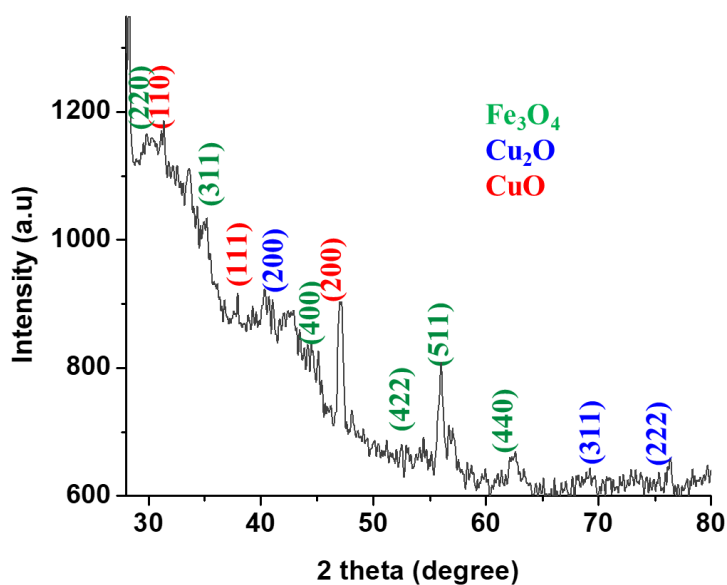


Fig. S56. Powder X-ray diffraction pattern of MNP-TC-S-Cu^{I/II}O 4.

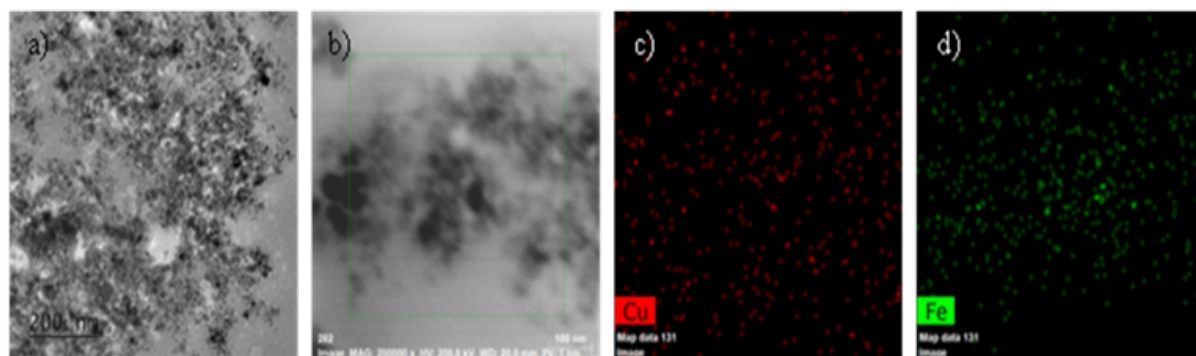


Fig. S57. TEM image of a) MNP-TC-S-Cu^{II}O **4**, b) TEM mapping of the portion selected for c) Cu and d) Fe.

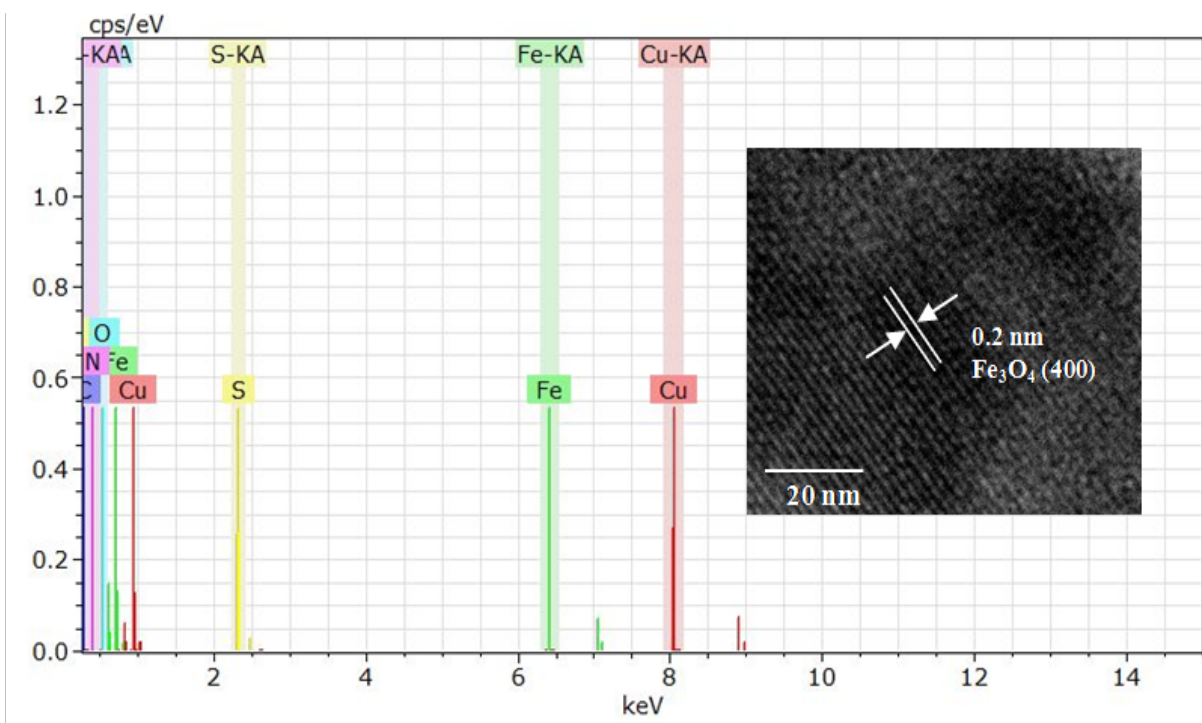


Fig. S58. EDX spectrum of as-prepared MNP-TC-S-Cu^{II}O **4**. HRTEM image of Fe₃O₄ nanoparticles (inset).

ICP-MS data of MNP-TC-S-Cu^{II}O **4:** The presence of copper and iron on catalyst **4** was estimated to be 26.149 and 27.877 wt%, respectively, as determined by ICP-MS.

G4. TEM studies of reused MNP-TC-S-Cu^{II}O 4

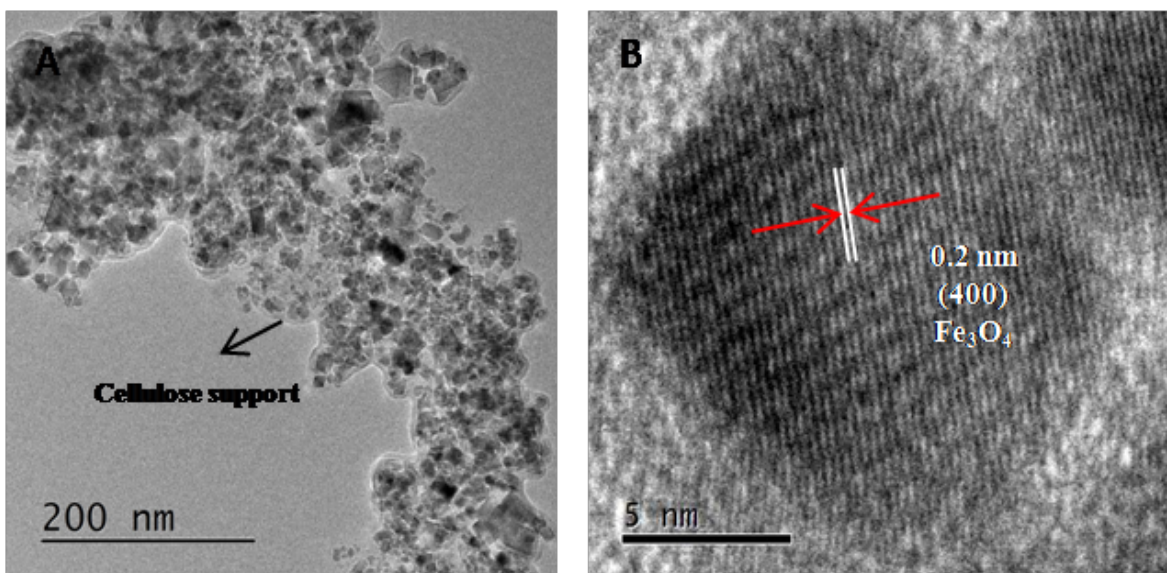


Fig. S59. A) TEM, B) HR-TEM images of catalyst 4 after 5th run.

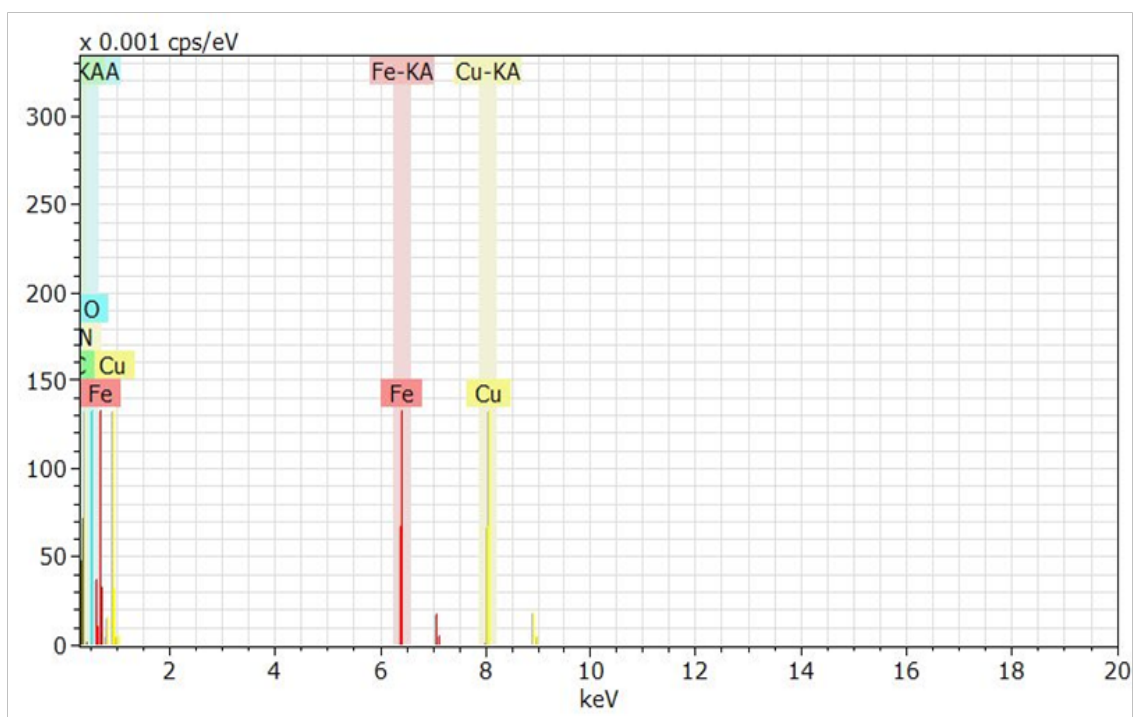


Fig. S60. EDX spectrum of catalyst 4 after 5th run showing the presence of both copper and iron in the catalyst.

H. References

1. D. Clarisse, P. Prakash, V. Geertsen, F. Miserque, E. Gravel and E. Doris, *Green Chem.*, 2017, **19**, 3112–3115.
2. L. C. Fidale, M. Nikolajski, T. Rudolph, S. Dutz, F. H. Schacher and T. Heinze, *J. Colloid Interface Sci.*, 2013, **390**, 25–33.
3. A. Gupta, A. Ahmad, H. Singh, S. Kaur, N. K M, Md. M. Ansari, G. Jayamurugan and R. Khan, *Biomacromolecules*, 2018, **19**, 803–815.
4. M. Nikolajski, J. Wotschadlo, J. H. Clement and T. Heinze, *Macromol. Biosci.*, 2012, **12**, 920–925.
5. K. Rahn, M. Diamantoglou, D. Klemm, H. Berghmans and T. Heinze, *Die Angew. Makromol. Chemie*, 1996, **238**, 143–163.
6. T. Heinze, M. Siebert, P. Berlin and A. Koschella, *Macromol. Biosci.*, 2016, **16**, 10–42.
7. P. Berlin, D. Klemm, J. Tiller and R. Rieseler, *Macromol. Chem. and Physics*, 2000, **201**, 2070–2082.
8. J. Rull-Barrull, M. d’Halluin, E. L. Grogneq and F.-X. Felpin, *Chem. Commun.*, 2016, **52**, 6569–6572.
9. J. Rull-Barrull, M. d’Halluin, E. Le Grogneq and F.-X. Felpin, *Angew. Chem. Int. Ed.*, 2016, **55**, 13549–13552.
10. C. E. Kast and A. Bernkop-Schnürch, *Biomaterials*, 2001, **22**, 2345–2352.
11. X. Wang, F. Zhang, B. Xia, X. Zhu, J. Chen, S. Qiu, P. Zhang and J. Li, *Solid State Sci.*, 2009, **11**, 655–659.
12. H. Azimi, S. Kuhri, A. Osvet, G. Matt, L. S. Khanzada, M. Lemmer, N. A. Luechinger, M. I. Larsson, E. Zeira, D. M. Guldi and C. J. Brabec, *J. Am. Chem. Soc.*, 2014, **136**, 7233–7236.
13. S. D. Pike, E. R. White, A. Regoutz, N. Sammy, D. J. Payne, C. K. Williams and M. S. P. Shaffer, *ACS Nano*, 2017, **11**, 2714–2723.
14. A. Ashok, A. Kumar, R. R. Bhosale, M. A. H. Saleh and L. J. P. van den Broeke, *RSC Adv.*, 2015, **5**, 28703–28712.
15. W. Gan, L. Gao, X. Zhan and J. Li, *RSC Adv.*, 2016, **6**, 37600–37609.
16. J. Jover, P. Spuhler, L. Zhao, C. McArdle and F. Maseras, *Catal. Sci. Technol.*, 2014, **4**, 4200–4209.

17. S. Díez-González, in *Advances in Organometallic Chemistry*, ed. P. J. Pérez, Academic Press, 2016, vol. 66, pp. 93–141.
18. L. Fomina, B. Vazquez, E. Tkatchouk and S. Fomine, *Tetrahedron*, 2002, **58**, 6741–6747.
19. X. Qi, R. Bai, L. Zhu, R. Jin, A. Lei and Y. Lan, *J. Org. Chem.*, 2016, **81**, 1654–1660.
20. A. P. Silvestri, P. A. Cistrone and P. E. Dawson, *Angew. Chem. Int. Ed.*, 2017, **56**, 10438–10442.
21. Y.-Q. Zhang, N. Kepčija, M. Kleinschrodt, K. Diller, S. Fischer, A. C. Papageorgiou, F. Allegretti, J. Björk, S. Klyatskaya, F. Klappenberger, M. Ruben and J. V. Barth, *Nat Commun*, 2012, **3**, 1–8.
22. J. Zemann, *Acta Cryst*, 1965, **18**, 139–139.
23. C. Gattinoni and A. Michaelides, *Surf. Sci. Reports*, 2015, **70**, 424–447.
24. P. Hohenberg and W. Kohn, *Phys. Rev. B*, 1964, **136**, 864–871.
25. W. Kohn and L. J. Sham, *Phys. Rev.*, 1965, **140**, A1133–A1138.
26. J. P. Perdew, K. Burke and M. Ernzerhof, *Phys. Rev. Lett.*, 1996, **77**, 3865–3868.
27. D. M. Ceperley and B. J. Alder, *Phys. Rev. Lett.*, 1980, **45**, 566–569.
28. G. Kresse and J. Furthmüller, *Phys. Rev. B*, 1996, **54**, 1169–1186.
29. G. Kresse and D. Joubert, *Phys. Rev. B*, 1999, **59**, 1758–1775.
30. A. Warshel and R. M. Weiss, *J. Am. Chem. Soc.*, 1980, **102**, 6218–6226.
31. D. Marx and J. Hutter, *Modern Methods and Algorithms of Quantum Chemistry (NIC Series (vol 1))*, ed J Grotendorst (Forschungszentrum Juelich), 2000
32. S. Grimme, J. Antony, S. Ehrlich and H. Krieg, *J. Chem. Phys.*, 2010, **132**, 154104.
33. F. Bohlmann, H. Schönowsky, E. Inhoffen and G. Grau, *Chem. Ber*, 1964, **97**, 794–800
34. L. G. Fedenok, V. M. Berdikov and M. S. Shvartsberg, *Zh. Org. Khim.*, 1978, **14**, 1423–1429
35. L. G. Fedenok, V. M. Berdikov and M. S. Shvartsberg, *Zh. Org. Khim.*, 1978, **14**, 1429–1432.
36. X. Yu, S. Tong, M. Ge, J. Zuo, C. Cao, W. Song, *J. Mater. Chem. A.*, 2013, **1**, 959–965.
37. R. Xiong, Y. Wang, X. Zhang, C. Lu, *RSC Adv.*, 2014, **4**, 22632–22641.
38. W. Chen, J. Chen, Y.-B. Feng, L. Hong, Q.-Y. Chen, L.-F. Wu, X.-H. Lina, X.-H. Xia, *Analyst* 2012, **137**, 1706–1712.

39. A. Lak, J. Dieckhoff, F. Ludwig, J. M. Scholtyssek, O. Goldmann, H. Lunsdorf, D. Eberbeck, A. Kornowski, M. Kraken, F. J. Litterst, K. Fiege, P. Mischnick, M. Schillinga, *Nanoscale* 2013, **5**, 11447–11455.